

A finite volume framework for damage and fracture prediction in wire drawing

Andrew Whelan^{1,2,3,4}, Tian Tang⁵, Vikram Pakrashi^{1,2,3,4},
Philip Cardiff^{1,2,3,4,6*}

¹*School of Mechanical and Materials Engineering, University College Dublin, Ireland.

²SFI MaREI Centre, University College Dublin, Ireland.

³UCD Centre for Mechanics, University College Dublin, Ireland.

⁴Bekaert University Technology Centre, University College Dublin, Ireland.

⁵NV Bekaert SA, Kortrijk, Belgium.

⁶SFI I-Form Centre, University College Dublin, Ireland.

*Corresponding author. E-mail: philip.cardiff@ucd.ie

Abstract

This article presents the implementation of the canonical Lemaitre and Gurson-Tvergaard-Needleman (GTN) damage models and a more recent phase-field type model within a Lagrangian, geometrically nonlinear, cell-centred finite volume framework. The proposed segregated solution procedure uses Picard-type defect (deferred) outer corrections, where the primary unknowns are cell-centre displacements and pressures. Spurious zero-energy modes (numerical oscillations in displacement and pressure) are avoided by introducing stabilisation (smoothing) diffusion terms to the pressure and momentum equations. Appropriate scaling of the momentum “Rheie-Chow” stabilisation term is shown to be important in regions of plasticity and damage. To accurately predict damage and fracture in wire drawing where hydrostatic pressure is high, novel variants of the Lemaitre model with crack-closure and triaxiality effects are proposed. The developed methods are validated against the *notched round bar* and *flat notched bar* experimental cases and subsequently applied to the analysis of axisymmetric wire drawing. It is shown that the proposed finite volume approach provides a robust basis for predicting damage in wire drawing, where the proposed novel Lemaitre model with crack-closure effects was shown to be the most suitable for predicting experimentally observed fracture.

Keywords: finite volume method, damage, fracture, Lemaitre, Gurson-Tvergaard-Needleman, phase field model, OpenFOAM

1 Introduction

Numerical simulations of ductile fracture are of great interest in industries such as aerospace [1, 2], automotive [3–6], nuclear [7], and metal forming [8–13] to predict where and when damage or fracture will occur. The availability of computational predictive tools allows for substantial savings in the cost of experiments and design optimisation. In this work, the drawing of high-carbon steel wire products is the primary interest [11, 12]. The drawing process can often lead to defects and even fractures during production. By improving understanding of how and why fracture occurs, products and processes can be optimised.

A computational model for ductile fracture should predict several features, such as the stress and strain distribution, damage origination and propagation, and the resulting loss of load-carrying capacity. In the review of Besson [14], fracture models were classified into global and local approaches. The Rice J -integral model is the canonical global approach; however, this approach suffers from limitations, such that it cannot predict crack initiation and propagation, and the J -integral is also not a material property as it strongly depends on the specimen geometry [15]. These problems were rectified by the J - Q integral approach; however, this approach, in turn, has the limitation that it does not apply to complex geometries [16]. Further developments in this family of models, such as the critical crack tip opening displacement or crack tip opening angle, share the same limitations [17, 18]. These models have been implemented in finite element solvers with remeshing techniques needed to model the crack propagation.

The limitations of the global approach have led to the development of local approaches. These methods characterise the fracture zone in more physical detail. These models can, in turn, be split into surface models (cohesive zone models), where fracture occurs on a surface, and volume models, where damage or degradation occurs in a volume. A limitation of cohesive zone models is that they often require a pre-defined crack path and typically exhibit strong mesh dependency. With these limitations in mind, this work focuses on the volume or *continuum* damage mechanics approaches, stemming from the work of Lemaître [19, 20], and micro-mechanical approaches, as originally proposed by Gurson-Tvergaard-Needleman (GTN) [21, 22]. A review of these approaches is left to Section 3. Within the past 15 years, an alternative volume ductile damage model has emerged, known as the phase field model approach [23–27]. This approach involves diffusing the sharp crack over a continuum. Models of this form are also implemented in this work and are described in Section 3.

In recent years, there has been an increasing interest in exploring the finite volume method for structural application and the interested reader is directed to a recent review by Cardiff and Demirdžić [28]. While the volume damage models have been implemented within finite element frameworks, they have seen little attention within the finite volume community. As shown in this work, the segregated Picard iteration solution methodology, commonly employed in the finite volume method, demonstrates favourable convergence properties for the highly nonlinear material behaviour experienced in wire drawing.

Although both Eulerian and Lagrangian approaches have been adopted for metal forming, the Lagrangian approach is now commonly favoured due to its ability to easily capture elastic effects,

e.g. residual stresses and *spring back*, notwithstanding its limitation of mesh deterioration for severe deformations. Nonetheless, for continuous processes such as wire drawing, Lagrangian approaches require the user to select a sufficiently long initial domain (e.g., initial wire length) so that steady-state phenomena of interest can be examined. Eulerian approaches do not have such a limitation as the workpiece *inlet* and *outlet* (i.e., wire upstream and downstream boundaries) are static in space. To combine the advantages of both, the current work proposes a Lagrangian approach with novel Eulerian-style boundary conditions, which allow the wire upstream and downstream boundaries to stay fixed in space.

Three main contributions are proposed in this work: (i) Nascent damage model implementations within a cell-centred finite volume framework, including a novel Lemaitre damage formulation for wire drawing; (ii) Eulerian-style boundary conditions for continuous forming processes, where mesh layers are added and removed at the workpiece upstream and downstream boundaries. (iii) A segregated large strain pressure-displacement finite volume formulation, where scaled Rhie-Chow stabilisation terms are proposed for quelling pressure oscillations while minimising over-smoothing of the damage fields. All implementations are performed in the solids4foam toolbox [29, 30] for the open-source C++ software OpenFOAM, building on previous work related to metal forming [11, 13]. Code and cases are publicly shared on GitHub at <http://github.com/awhelanUCD/solids4foam>.

The remainder of the paper is organised as follows: Section 2 describes the mathematical model and presents the finite volume numerical method, where details of the elastoplastic damage laws are left to Section 3. The implemented damage procedures are verified in Section 4, and applied to wire drawing in Section 5. The article ends with a summary of the main conclusions.

2 Mathematical Model and Numerical Methods

This section outlines the Lagrangian large strain, finite volume methodology, where details of the constitutive laws are left to Section 3.

2.1 Linear Momentum Conservation

The dynamic, Lagrangian, strong integral form of linear momentum conservation for a body Ω , bounded by a surface Γ with outwards pointing normal \mathbf{n} , can be expressed in *total* Lagrangian form as

$$\int_{\Omega_o} \rho_o \frac{\partial^2 \mathbf{u}}{\partial t^2} d\Omega_o = \oint_{\Gamma_o} (J \mathbf{F}^{-T} \cdot \mathbf{n}_o) \cdot \boldsymbol{\sigma} d\Gamma_o \quad (1)$$

or equivalently in *updated* Lagrangian form as

$$\int_{\Omega_u} \frac{\partial}{\partial t} \left(\rho_u \frac{\partial \mathbf{u}}{\partial t} \right) d\Omega_u = \oint_{\Gamma_u} (j \mathbf{f}^{-T} \cdot \mathbf{n}_u) \cdot \boldsymbol{\sigma} d\Gamma_u \quad (2)$$

where ρ is the density, \mathbf{u} is the displacement vector, $\boldsymbol{\sigma}$ is the true (Cauchy) stress, and body forces are neglected. Subscript o indicates quantities in the initial reference configuration, and subscript u indicates quantities in the updated configuration. The two forms are connected through Nanson's

formula [31], which relate the deformed area vector $\boldsymbol{\Gamma}$ with the initial area vector $\boldsymbol{\Gamma}_o$:

$$\boldsymbol{\Gamma} = J \mathbf{F}^{-T} \cdot \boldsymbol{\Gamma}_o \quad (3)$$

The deformation gradient is defined as $\mathbf{F} = \mathbf{I} + (\nabla \mathbf{u})^T$ and its determinant (Jacobian) as $J = \det(\mathbf{F})$. The *relative* deformation gradient is given in terms of the displacement increment as $\mathbf{f} = \mathbf{I} + [\nabla(\Delta \mathbf{u})]^T$ and the relative Jacobian as $j = \det(\mathbf{f})$.

The conservation of linear momentum in integral form (Equations 1 and 2) can equally be applied to entire domain or a sub-region of it such as a computational cell, as is the basis of the cell-centred finite formulation presented below. Although the total Lagrangian approach is a viable option for wire drawing, the current work adopts the updated Lagrangian approach as developing Eulerian-type upstream and downstream conditions (Section 2.5) is conceptually easier in an updated Lagrangian formulation.

The definition of the true stress in Equations 1 and 2 comes from the constitutive law, as is described in Section 3.

2.2 Solution Domain Discretisation

The solution domain is discretised in space and time. The total specified simulation time is divided into a finite number of time increments Δt , and the discretised governing momentum equation is solved in a time-marching manner.

The space domain is divided into a finite number of contiguous convex polyhedral cells. The proposed solution discretisation follows closely the approach of Cardiff et al. [13]; consequently, only an overview of the final discretised form of equations and adopted solution algorithm are given below.

The employed finite volume discretisation begins by applying the governing conservation equation (Equation 2) to each cell in the mesh. To facilitate the use of a segregated solution algorithm, and the surface forces term (term on the right-hand side of Equation 2) is split into explicit and implicit components:

$$\int_{\Omega_u} \frac{\partial}{\partial t} \left(\rho_u \frac{\partial \mathbf{u}}{\partial t} \right) d\Omega_u = \underbrace{\oint_{\Gamma_u} K_{imp} \mathbf{n}_u \cdot \nabla(\Delta \mathbf{u}) d\Gamma_u}_{\text{implicit}} + \underbrace{\oint_{\Gamma_u} (j \mathbf{f}^{-T} \cdot \mathbf{n}_u) \cdot \boldsymbol{\sigma} d\Gamma_u - \oint_{\Gamma_u} K_{imp} \mathbf{n}_u \cdot \nabla(\Delta \mathbf{u}) d\Gamma_u}_{\text{explicit}} \quad (4)$$

where the first term on the right-hand side (Laplacian term) is treated implicitly, and the second and third terms on the right-hand side are treated in a explicit manner. Here, by implicit, we mean that the term contributes coefficients to the resulting linear(-ised) system of equations. In contrast, here, by explicit we mean that the terms are treated in a deferred correction manner; that is, they are evaluated using the latest available values; consequently, the explicit terms

contribute only to the source of the system of linear equations. The overall procedure is implicit in time in that the time step size is not constrained by the Courant–Friedrichs–Lewy condition. From a deferred (or defect) correction perspective, this Laplacian term can be considered an approximate compact-stencil linearisation of the surface stress term. This allows the coupled vector system to be temporarily decoupled into three scalar component equations. These three scalar component equations can then be solved independently, where outer Picard iterations provide the inter-component coupling. Unlike Newton-Raphson approaches, where quadratic convergence may be expected, linear convergence of the residuals can be expected when using a segregated approach; however, this disadvantage is offset in several ways: (i) an exact Jacobian stiffness matrix need not be assembled, which is often costly; (ii) a material tangent is not required for the material laws, as instead the scalar coefficient K_{imp} is only required; (iii) outer Picard iterations are less expensive than Newton iterations as the discretised systems are smaller to assemble and quicker to solve; (iv) Picard iterations may provide superior convergence when the solution is far from the asymptotic region, potentially resulting in a more robust approach for highly nonlinear large strain fracture and damage cases. Nonetheless, as noted previously [32], segregated solution procedures can require significantly more outer iterations and exhibit slow convergence relative to coupled approaches, particularly in high aspect ratio linear cases. In the current work, K_{imp} is chosen following the work of Jasak and Weller [33] as

$$K_{imp} = \frac{4}{3}\mu + \kappa \quad (5)$$

where μ is the material shear modulus and κ is the bulk modulus. It should be reinforced that the value of K_{imp} affects convergence but does not affect the final converged solution – assuming convergence is achieved.

The primary unknown to be solved for is the displacement increment $\Delta\mathbf{u} = \mathbf{u}^{[m+1]} - \mathbf{u}^{[m]}$ where the superscript $[m]$ indicates a quantity from the previous time step and $[m+1]$ a quantity from the current (to be calculated) time step.

The resulting conservation equation (Equation 4) is applied to each cell (control volume) in the computational mesh and discretised in terms of the displacement increment at the cell centre/centroid ($\Delta\mathbf{u})_P$ and at the centres of the neighbouring cells N_i .

The temporal volume integral term is discretised in space using the second-order mid-point rule and discretised in time using a first-order accurate implicit backward Euler scheme [33]:

$$\begin{aligned} \int_{\Omega_u} \frac{\partial}{\partial t} \left(\rho_u \frac{\partial(\Delta\mathbf{u})}{\partial t} \right) d\Omega_u &\approx \frac{\partial}{\partial t} \left(\rho_u \frac{\partial(\Delta\mathbf{u})}{\partial t} \right)_P \Omega_P \\ &\approx \left(\frac{\rho_u^{[m+1]} \frac{\partial(\Delta\mathbf{u})^{[m+1]}}{\partial t} - \rho_u^{[m]} \frac{\partial(\Delta\mathbf{u})^{[m]}}{\partial t}}{\Delta t} \right)_P \Omega_P \\ &\approx \left[\frac{\rho_u^{[m+1]} \left(\frac{\Delta\mathbf{u}^{[m+1]} - \Delta\mathbf{u}^{[m]}}{\Delta t} \right) - \rho_u^{[m]} \left(\frac{\Delta\mathbf{u}^{[m]} - \Delta\mathbf{u}^{[m-1]}}{\Delta t} \right)}{\Delta t} \right]_P \Omega_P \\ &\approx \frac{1}{\Delta t^2} \left[\rho_{u_P}^{[m+1]} \Delta\mathbf{u}_P^{[m+1]} - \left(\rho_{u_P}^{[m+1]} + \rho_{u_P}^{[m]} \right) \Delta\mathbf{u}_P^{[m]} + \rho_{u_P}^{[m]} \Delta\mathbf{u}_P^{[m-1]} \right] \Omega_P \end{aligned} \quad (6)$$

The $\mathbf{u}^{[m-1]}$ term is discretised in a similar fashion, noting that $\mathbf{u}^{[m]} = \mathbf{u}^{[m-1]} + \Delta\mathbf{u}$ in Equation 4. In the cases examined in this work, inertial effects are relatively small, so temporal accuracy is not a concern. All dependent variables must be specified at the initial time.

The surface forces Laplacian term (first term on the right-hand side of Equation 4) is discretised using central differencing with over-relaxed non-orthogonal correction [13, 33–36]:

$$\underbrace{\oint_{\Gamma_u} K_{imp} \mathbf{n}_u \cdot \nabla (\Delta\mathbf{u}) d\Gamma_u}_{\text{implicit}} \approx \sum_{f \in N_f} K_{imp}^f |\Delta_{u_f}| \left(\frac{\Delta\mathbf{u}_{N_f} - \Delta\mathbf{u}_P}{|\mathbf{d}_f|} \right) |\Gamma_{u_f}| + \sum_{f \in N_f} K_{imp}^f \mathbf{k}_{u_f} \cdot [\nabla (\Delta\mathbf{u})]_f |\Gamma_{u_f}| \quad (7)$$

where N_f represents the set of faces f in cell P , and neighbouring cell centre N_f shares face f with the cell P . The over-relaxed orthogonal vector $\Delta_{u_f} = \frac{\mathbf{d}_{u_f}}{\mathbf{d}_{u_f} \cdot \mathbf{n}_{u_f}}$ and non-orthogonal correction vector $\mathbf{k}_{u_f} = \mathbf{n}_{u_f} - \Delta_{u_f}$, where \mathbf{n}_{u_f} is the outward-facing unit normal to the face f . Vector \mathbf{d}_{u_f} connects the centre of cell P with the centre of cell N_f in the updated configuration. The first term on the right-hand side is treated implicitly, while the second term - representing non-orthogonal corrections at the face - is treated in a deferred correction manner.

The remaining surface force terms (second and third terms on the right-hand side of Equation 4) are discretised by assuming that they vary linearly across the face as follows [37]:

$$\underbrace{\oint_{\Gamma_u} (j\mathbf{f}^{-T} \cdot \mathbf{n}_u) \cdot \boldsymbol{\sigma} d\Gamma_u}_{\text{explicit}} \approx \sum_{f \in N_f} \boldsymbol{\Gamma}_{u_f} \cdot (j\boldsymbol{\sigma}\mathbf{f}^{-T})_f \quad (8)$$

$$\underbrace{\oint_{\Gamma_u} K_{imp} \mathbf{n}_u \cdot \nabla (\Delta\mathbf{u}) d\Gamma_u}_{\text{explicit}} \approx \sum_{f \in N_f} K_{imp}^f \boldsymbol{\Gamma}_{u_f} \cdot [\nabla (\Delta\mathbf{u})]_f \quad (9)$$

The terms at a face, indicated by the subscript f , are calculated by linearly interpolating from the adjacent cell-centres. The cell-centre gradients $\nabla (\Delta\mathbf{u})$ are determined using a least squares method [37].

2.3 Boundary conditions

Boundary conditions are enforced through modification of the discretised expressions on boundary faces. Five classes of boundary conditions are employed in the current work (prescribed displacement, prescribed traction, symmetry plane, axisymmetric/wedge, frictional contact) as described below. An additional boundary condition where the normal component of the displacement is prescribed and the shear traction is zero is also used; the discretisation of this condition employs the prescribed displacement condition in the boundary normal direction and the traction condition in the tangential direction.

Prescribed displacement

The displacement boundary condition, a Dirichlet condition, may be constant in time or time-varying and fixes the value of \mathbf{u} at the centre of a boundary face. The corresponding displacement increment at the boundary face $\Delta\mathbf{u}_b = \mathbf{u}^{[m+1]} - \mathbf{u}^m$ is substituted into the calculation of the surface normal gradient term in Equation 7. The resulting contribution of a boundary face b to the discretised diffusion term becomes:

$$\underbrace{\int_{\Gamma_{u_b}} K_{imp} \mathbf{n}_{u_b} \cdot \nabla(\Delta\mathbf{u}) d\Gamma_{u_b}}_{\text{implicit}} \approx K_{imp}^b |\Delta_{u_b}| \left(\frac{\Delta\mathbf{u}_b - \Delta\mathbf{u}_P}{|\mathbf{d}_b|} \right) |\boldsymbol{\Gamma}_{u_b}| + K_{imp}^b \mathbf{k}_{u_b} \cdot [\nabla(\Delta\mathbf{u})]_P |\boldsymbol{\Gamma}_{u_b}| \quad (10)$$

where \mathbf{d}_b connects the centre of cell P with the boundary face centre in the updated configuration, and the non-orthogonal correction vector $\mathbf{k}_{u_b} = (\mathbf{I} - \mathbf{n}\mathbf{n}) \cdot \mathbf{d}_b$.

Prescribed traction

The traction boundary condition, constant in time or time-varying, is implemented as a Neumann condition where the normal gradient, $\mathbf{g}_b \equiv \mathbf{n} \cdot \nabla(\Delta\mathbf{u})$, of the displacement increment is specified on the boundary face. The specified normal boundary gradient, may be directly substituted into the discretised diffusion term, Equation 7:

$$\underbrace{\int_{\Gamma_{u_b}} K_{imp} \mathbf{n}_{u_b} \cdot \nabla(\Delta\mathbf{u}) d\Gamma_{u_b}}_{\text{implicit}} \approx K_{imp}^b \mathbf{g}_b |\boldsymbol{\Gamma}_{u_f}| \quad (11)$$

The normal gradient, \mathbf{g}_b , which corresponds to the specified boundary traction, \mathbf{T}_b , is determined from the expression for the discretised boundary traction as

$$\begin{aligned} \mathbf{T}_b &= \mathbf{n}_b \cdot \boldsymbol{\sigma}_b \\ &= K_{imp}^b \mathbf{g}_b + \mathbf{n}_b \cdot \boldsymbol{\sigma}_b - K_{imp}^b \mathbf{n}_b \cdot [\nabla(\Delta\mathbf{u})]_b \end{aligned} \quad (12)$$

which is rearranged to give \mathbf{g}_b :

$$\mathbf{g}_b = \frac{\mathbf{T}_b - \mathbf{n}_b \cdot \boldsymbol{\sigma}_b - K_{imp}^b \mathbf{n}_b \cdot [\nabla(\Delta\mathbf{u})]_b}{K_{imp}^b} \quad (13)$$

At each outer (Picard) iteration, \mathbf{g}_b is explicitly updated according to Equation 13, where all terms on the right-hand side are evaluated using the latest available values. At convergence within each time step, the $K_{imp}^b \mathbf{g}_b$ and $K_{imp}^b \mathbf{n}_b \cdot (\nabla\phi)_b$ terms in Equation 12 cancel out and the traction condition is enforced. It is also worth noting that substitution of Equation 13 into discretised diffusion term results in the contribution to the source of the entire linear system being the force on the face. If the value of $\Delta\mathbf{u}_b$ is needed at the face b , it is obtained by extrapolating from the

adjacent cell centre ($\Delta\mathbf{u}_P$) as

$$(\Delta\mathbf{u})_b = (\Delta\mathbf{u})_P + (\mathbf{n}_b \cdot \mathbf{d}_b)g_b + [(\mathbf{I} - \mathbf{n}_b\mathbf{n}_b) \cdot \mathbf{d}_b] \cdot [\nabla(\Delta\mathbf{u})]_P \quad (14)$$

Symmetry plane

The symmetry plane is a mixed condition, where the normal component is a Dirichlet condition and the tangential component is a Neumann condition. The component of the dependent variable normal to the boundary is zero and the shear/tangential traction is zero. For boundary faces on a symmetry plane, the mirror reflection $(\Delta\mathbf{u})_N$ of the $(\Delta\mathbf{u})_P$ can be obtained as

$$\begin{aligned} (\Delta\mathbf{u})_N &= \mathbf{R}_m \cdot (\Delta\mathbf{u})_P \\ &= (\mathbf{I} - 2\mathbf{n}_b\mathbf{n}_b) \cdot (\Delta\mathbf{u})_P \end{aligned} \quad (15)$$

where \mathbf{R}_m is termed the reflection tensor. The discretisation in Equation 7 takes the same form with the mirror reflected values used at boundary faces on the symmetry plane. The \mathbf{d}_b vector at a symmetry plane boundary face is calculated as

$$\mathbf{d}_b = \mathbf{R}_m \cdot \mathbf{C}_P - \mathbf{C}_P \quad (16)$$

where \mathbf{C}_P is the positional vector of the centre of cell P . This means that symmetry planes are orthogonal by definition and the non-orthogonal correction (second term on the right-hand side of Equation 7) drops out. Further details on the implementation of symmetry planes in segregated cell-centred finite volume formulations can be found in Demirdžić and Cardiff [38].

In the approach adopted here, displacement increment values on the symmetry planes are calculated as

$$(\Delta\mathbf{u})_b = \frac{(\Delta\mathbf{u})_P^* + (\Delta\mathbf{u})_N^*}{2} \quad (17)$$

where cell-centred values corrected for mesh skewness errors are

$$(\Delta\mathbf{u})_P^* = (\Delta\mathbf{u})_P + [(\mathbf{I} - \mathbf{n}\mathbf{n}) \cdot \mathbf{d}_b] \cdot [\nabla(\Delta\mathbf{u})]_P \quad (18)$$

$$(\Delta\mathbf{u})_N^* = \mathbf{R}_m \cdot (\Delta\mathbf{u})_P^* \quad (19)$$

Axisymmetric (wedge)

Axisymmetry problems are approached by constructing a wedge-shaped slice of the domain [39], where a small wedge angle (e.g., 1°) is adopted to minimise geometry errors. Axisymmetric conditions are applied to the two sloping sides of the wedge. Similar to the symmetry condition, the axisymmetric condition replaces the neighbouring displacement increment value $(\Delta\mathbf{u})_N$ at a axisymmetric boundary face in Equation 7 with the equivalent reflected value. Unlike the symmetry

condition, the reflection on an axisymmetric boundary comes from a rotation about the axis:

$$(\Delta \mathbf{u})_N = \mathbf{R}_c \cdot (\Delta \mathbf{u})_P \quad (20)$$

where $\mathbf{R}_c = \mathbf{R}_f \mathbf{R}_f$ is the rotation tensor that rotates values on the centre plane (centre plane of the wedge-shaped slice) to the equivalent location on a neighbouring adjacent wedge centre plane. The \mathbf{R}_f tensor, which rotates values on the centre plane to the sloping side of the domain boundary, is calculated according to the Euler-Rodrigues rotation formula [39, 40]

$$\mathbf{R}_f = (\mathbf{n}_c \cdot \mathbf{n}_f) \mathbf{I} + [1 - (\mathbf{n}_c \cdot \mathbf{n}_f)] \mathbf{n}_a \mathbf{n}_a + \mathbf{n}_f \mathbf{n}_c - \mathbf{n}_c \mathbf{n}_f \quad (21)$$

where $\mathbf{n}_a = (\mathbf{n}_c \times \mathbf{n}_f)/|\mathbf{n}_c \times \mathbf{n}_f|$ is the unit axis direction, \mathbf{n}_c is the unit normal of the centre plane, and \mathbf{n}_f is the unit normal of the sloping side of the domain boundary.

Similar to the symmetry plane, the displacement increment values on the sloping wedge boundary planes are calculated as

$$(\Delta \mathbf{u})_b = \mathbf{R}_f \cdot \{(\Delta \mathbf{u})_P + \mathbf{k}_b \cdot [\nabla (\Delta \mathbf{u})]_P\} \quad (22)$$

where, once again, the second term within the brackets on the right-hand side corrects for mesh skewness. The \mathbf{k}_b correction vector is calculated as

$$\mathbf{k}_b = \mathbf{C}_b - \mathbf{R}_f \cdot \mathbf{C}_P \quad (23)$$

and represents the vector from the cell centre \mathbf{C}_P rotated to the sloping wedge patch and the face centre \mathbf{C}_b at the patch.

Frictional contact

Coulomb friction contact boundaries are handled using an iterative penalty method, as described previously by the authors [13, 41]. From an implementation perspective, the contact boundaries are a special type of prescribed traction condition where the traction distribution is re-calculated every solution outer (Picard) iteration according to a penalty law formulation. More recent extensions of this approach have been proposed by Batistić et al. [42, 43], including segment-to-segment and implicit approaches, but these are not used in the current work.

2.3.1 Rhie-Chow Stabilisation

The difference in the computational stencil for the first and third terms on the right-hand side in Equation 4 introduces third-order numerical diffusion to the discretisation, which quells spurious zero-energy checkerboarding solution oscillations. First introduced by Rhie and Chow [44] for cell-centred finite volume methods, Demirdžić and Muzaferija [45] extended this approach for solid mechanics. In the current approach, the Rhie-Chow stabilisation term $\mathcal{D}_{\text{Rhie-Chow}}$ takes the

following form:

$$\mathcal{D}_{\text{Rhie-Chow}} = \sum_{f \in N_f} K_{imp}^f \left[|\Delta_f| \frac{\Delta \mathbf{u}_{N_f} - \Delta \mathbf{u}_P}{|\mathbf{d}_f|} - \Delta_f \cdot [\nabla(\Delta \mathbf{u})]_f \right] |\Gamma_{u_f}| \quad (24)$$

which comes from the difference between Equations 7 and 9. The first term on the right-hand side represents a compact stencil (two-node) approximation of the face normal gradient, while the second term represents a larger stencil approximation. These two terms cancel out in the limit of mesh refinement (or if the solution varies linearly); otherwise, they produce a stabilisation effect that tends to smooth the solution fields. As the term reduces at a third-order rate, it does not affect the overall scheme's second-order accuracy.

As shown in Section 4, the magnitude of the Rhie-Chow stabilisation affects the localisation behaviour for damage and fracture mechanics models, with a tendency to artificially *smear* damage fields. Two mitigation strategies are proposed here to produce a modified Rhie-Chow stabilisation $\hat{\mathcal{D}}_{\text{Rhie-Chow}}$:

- (a) The Rhie-Chow stabilisation is scaled by a global scalar constant $0 \leq \mathcal{R}$:

$$\hat{\mathcal{D}}_{\text{Rhie-Chow}} = \mathcal{R} \mathcal{D}_{\text{Rhie-Chow}} \quad (25)$$

- (b) The Rhie-Chow stabilisation is scaled by a global scalar constant in addition to a damage-dependent field:

$$\hat{\mathcal{D}}_{\text{Rhie-Chow}} = \mathcal{R}(1 - D)^2 \mathcal{D}_{\text{Rhie-Chow}} \quad (26)$$

In the first approach, the smoothing effect is reduced globally, lessening the smearing of damage fields; however, this approach's disadvantage is that solution convergence is slowed as the stabilisation term is reduced in magnitude everywhere. In addition, numerical oscillations are more likely to appear, particularly in regions undergoing purely elastic deformation where no dissipation mechanisms exist. In the second approach, a damage variable $0 < D \leq 1$ (to be introduced in Section 3) reduces the smoothing effect only in regions of damage. The effect of these proposed modifications is examined in Section 4.4.5. Although the purpose of the proposed modifications is to reduce the amount of stabilisation, \mathcal{R} is not limited to be less than unity and hence can be used to increase the amount of stabilisation if desired.

2.3.2 Hydrostatic Pressure Calculation

Displacement-only formulations are known to be susceptible to numerical hydrostatic pressure oscillations in regions of large isochoric plastic strains. In Cardiff et al. [13], it was proposed to smooth the relative deformation gradient Jacobian field j . In contrast, the current approach proposes to decompose the stress tensor into deviatoric and volumetric terms, $\boldsymbol{\sigma} = \text{dev}(\boldsymbol{\sigma}) - p\mathbf{I}$, and solve a smoothed pressure Poisson equation:

$$p = \hat{p} + \mathcal{D}_{\text{Rhie-Chow}}^p \quad (27)$$

where \hat{p} is the hydrostatic pressure calculated directly from the displacement field, e.g. $\hat{p} = -1/J[\kappa \text{tr}(\boldsymbol{\epsilon})]$. The Rhie-Chow pressure stabilisation term $\mathcal{D}_{\text{Rhie-Chow}}^p$ is discretised according to Equation 24 with the displacement increment $\Delta\mathbf{u}$ replaced by the pressure p . Similar to the discretised momentum equation, the magnitude of the Rhie-Chow stabilisation term can be controlled with a global scale constant $0 \leq \mathcal{R}_p$. The effect of the Rhie-Chow stabilisation term here is to smooth any pressure oscillations. The final stabilised form of the pressure Poisson equation is

$$p - \mathbb{D}\nabla^2 p = \hat{p} - \nabla \cdot (\mathbb{D}\nabla p) \quad (28)$$

where the terms on the left-hand side are discretised implicitly, and the terms on the right-hand side are discretised using deferred corrections, following similar methods to Equations 6 and 7. The second terms on the left and right-hand sides come from the Rhie-Chow stabilisation. The described approach is similar to the formulation proposed by Bijelonja et al. [46–49] for incompressibility, quasi-incompressibility and elastoplasticity. The scalar coefficient \mathbb{D} ensures the stabilisation is scaled appropriately. Following a similar approach to SIMPLE-type computational fluid dynamic procedures, this term is calculated for a cell P in terms of the momentum equation diagonal coefficient (first term on the right-hand side of Equation 7):

$$\mathbb{D} = \mathcal{R}_p K_{imp} \Omega_P \sum_{f \in N_f} \frac{|\mathbf{d}_f|}{|\boldsymbol{\Delta}_f| |\boldsymbol{\Gamma}_{u_f}|} \quad (29)$$

As the pressure fields are typically relatively smooth, the predictions have been found to be relatively insensitive to the value of \mathcal{R}_p , where order of magnitude changes produce minimal effects on the results. Values in the range $1 \leq \mathcal{R}_p \leq 10^3$ are suitable for the types of cases examined in this work.

2.4 Solution Algorithm

The linear momentum equation is discretised for each control volume P in component form, and three linear algebraic equations of the following form is assembled [33]:

$$a_P \Delta u_P^i + \sum_{f \in N_f} a_{n_f} \Delta u_{N_f}^i = b_P^i \quad (30)$$

where Δu_P^i is the i^{th} component of the displacement increment at cell P , $\Delta u_{N_f}^i$ is the i^{th} component of the displacement increment at neighbouring cell N_f , and b_P^i is i^{th} component of the source vector contribution. The scalar central coefficient a_p , the scalar coefficients associated with the centre of neighbouring cell a_{n_f} (which shares a face f with cell P), and the source vector \mathbf{b}_P are

$$a_p = \frac{\rho_{u_P} \Omega_P^{[m+1]}}{\Delta t^2} + \sum_{f \in N_f} K_{imp}^f |\boldsymbol{\Gamma}_{u_f}| \frac{|\boldsymbol{\Delta}_{u_f}|}{|\mathbf{d}_f|} \quad (31)$$

$$a_{n_f} = -K_{imp}^f |\boldsymbol{\Gamma}_{u_f}| \frac{|\boldsymbol{\Delta}_{u_f}|}{|\mathbf{d}_f|} \quad (32)$$

$$\begin{aligned}
\mathbf{b}_P = & \frac{\Omega_P}{\Delta t^2} \left[\left(\rho_{u_P}^{[m+1]} + \rho_{u_P}^{[m]} \right) \Delta \mathbf{u}_P^{[m]} - \rho_{u_P}^{[m]} \Delta \mathbf{u}_P^{[m-1]} \right] \\
& + \sum_{f \in N_f} \boldsymbol{\Gamma}_{u_f} \cdot (j \boldsymbol{\sigma} \mathbf{f}^{-T})_f \\
& - \sum_{f \in N_f} K_{imp}^f \boldsymbol{\Gamma}_{u_f} \cdot [\nabla(\Delta \mathbf{u})]_f \\
& + \sum_{f \in N_f} K_{imp}^f \mathbf{k}_{u_f} \cdot [\nabla(\Delta \mathbf{u})]_f |\boldsymbol{\Gamma}_{u_f}|
\end{aligned} \tag{33}$$

These linear algebraic equations are then assembled for all control volumes, creating a system of linear algebraic equations for each direction i :

$$[\mathbf{K}] [\mathbf{u}] = [\mathbf{f}] \tag{34}$$

where $[\mathbf{K}]$ is an $M \times M$ sparse, symmetric coefficient matrix containing the coefficients from the implicit operators, with M being the total number of cells. The matrix $[\mathbf{K}]$ is the same for each direction before boundary condition contributions are included, meaning the matrix need only be formed once and stored once per time step. The solution vector $[\mathbf{u}]$ contains a component (e.g., x , y , or z) of the unknown cell-centre displacement increments $\Delta \mathbf{u}$, and $[\mathbf{f}]$ is the source term containing a component of the deferred correction terms. During the stress calculation, a similar scalar system is formed and solved for the hydrostatic pressure (Equation 28).

As noted in Section 2.2, a segregated solution algorithm is employed where the governing vector momentum equation is temporarily decoupled and three scalar equations are solved; outer Picard iterations at each time step provide the inter-equation coupling.

The *inner* linear sparse system is iteratively solved using an incomplete Cholesky preconditioned conjugate gradient method [50]. As noted in previous articles on segregated methods, the inner system need not be solved to a tight tolerance as coefficients and source terms are approximated from the previous increment; a reduction in the residuals of one order of magnitude is typically sufficient. The outer iterations are performed until the predefined tolerance, typically 1×10^{-6} , has been achieved [13].

In the current updated Lagrangian approach, the mesh is moved to the deformed configuration at the end of each time step rather than after each outer iteration. Since the displacements are calculated at the cell centres, a linear least-squared method is employed here [13] to interpolate the displacement increments to the mesh vertices, allowing the mesh to be moved.

The procedures have been implemented and publicly shared within the solids4foam toolbox [29, 30] of the open-source OpenFOAM software.

Algorithm 1 shows an overview of the solution algorithm.

Algorithm 1: Solution Procedure

```
for all time steps do
    while convergence not reached do
        - Discrete governing system (Equation 4) for each cell, using Equations 5-10, in terms of  $\Delta\mathbf{u}$ 
        - Assemble the discretised equations for all cells into three scalar linear systems (Equation 17)
        - Solve the three scalar linear systems in terms of cell-centred displacement increments  $\Delta\mathbf{u}$ 
        - Update the kinematics:  $\nabla(\Delta\mathbf{u})$ ,  $\mathbf{F}$ ,  $J$ ,  $\mathbf{f}$ ,  $j$ 
        - Update the stress ( $\sigma$ ) at the cell-centres using the chosen material law; optionally, solve the
          pressure equation.
        - Update the Rhie-Chow stabilisation:  $\hat{\mathcal{D}}_{\text{Rhie-Chow}}$ 
    end while
    - Interpolate cell-centre displacement increments to the vertices
    - Move the mesh to the deformed configuration using the vertex displacement increments,
      incorporating layer addition/removal (Section 2.4)
end for
```

2.5 Eulerian-Type Layer Addition and Removal Boundaries

Steady-state behaviour is typically the primary interest in wire drawing and other continuous forming approaches. Eulerian approaches are a natural choice but are not commonly employed when elastic phenomena (e.g. spring back, residual stresses) are important. When simulating wire drawing using a Lagrangian approach, a naïve approach is to simulate a workpiece segment that is *long enough* to allow steady-state to be reached. The disadvantage of this approach is that computational cost is inflated by the portion of the workpiece domain primarily undergoing rigid-body translation, which may be large relative to the region actively undergoing plastic deformations.

To overcome this disadvantage, the current work proposes Eulerian-type layer addition and removal conditions for the workpiece upstream and downstream boundaries. The approach involves fixing the workpiece (e.g., wire) upstream and downstream mesh boundaries in space during the mesh motion at the end of each time step. As cells at the upstream boundary become elongated, layers of new cells are added. Similarly, cells are removed as they become compressed near the downstream patch. In this way, the length of the workpiece domain remains fixed (like an Eulerian approach), but a traditional Lagrangian method is still used to calculate the deformation. Nonetheless, the proposed approach's limitation is that the workpiece domain mesh must consist of layers of cells in the streamwise direction.

Figure 1 schematically outlines the step involved in the layer addition and removal mesh motion scheme:

- (a) The workpiece (e.g., wire) mesh is constructed such that it is layered in the streamwise direction.
- (b) Solution of the discretised governing equations provides the cell centres displacement increments $\Delta\mathbf{u}$.
- (c) The cell-centred displacement increment $\Delta\mathbf{u}$ are interpolated to the vertices $\Delta\mathbf{u}_v$.
- (d) If the average width (in the streamwise direction) at the upstream boundary of the cell layer d_{av} is greater than a user-prescribed maximum width d_{max} , a zero-thickness layer of cells is added.
- (e) The displacement increments of the newly added layer of vertices are set to zero.

- (f) The mesh is moved by the vertex displacement increment field $\Delta\mathbf{u}_v$, where it is noted that the *original* vertices on the upstream and downstream points are allowed to move; this causes the newly added cell layer to *grow* by the displacement increment field.
- (g) If the average width (in the streamwise direction) of the cell layer d_{av} at the downstream boundary is less than a user-prescribed minimum width d_{min} , remove the layer of cells at the downstream boundary. Multiple cell layers may need to be iteratively removed depending on the displacement increment magnitude.

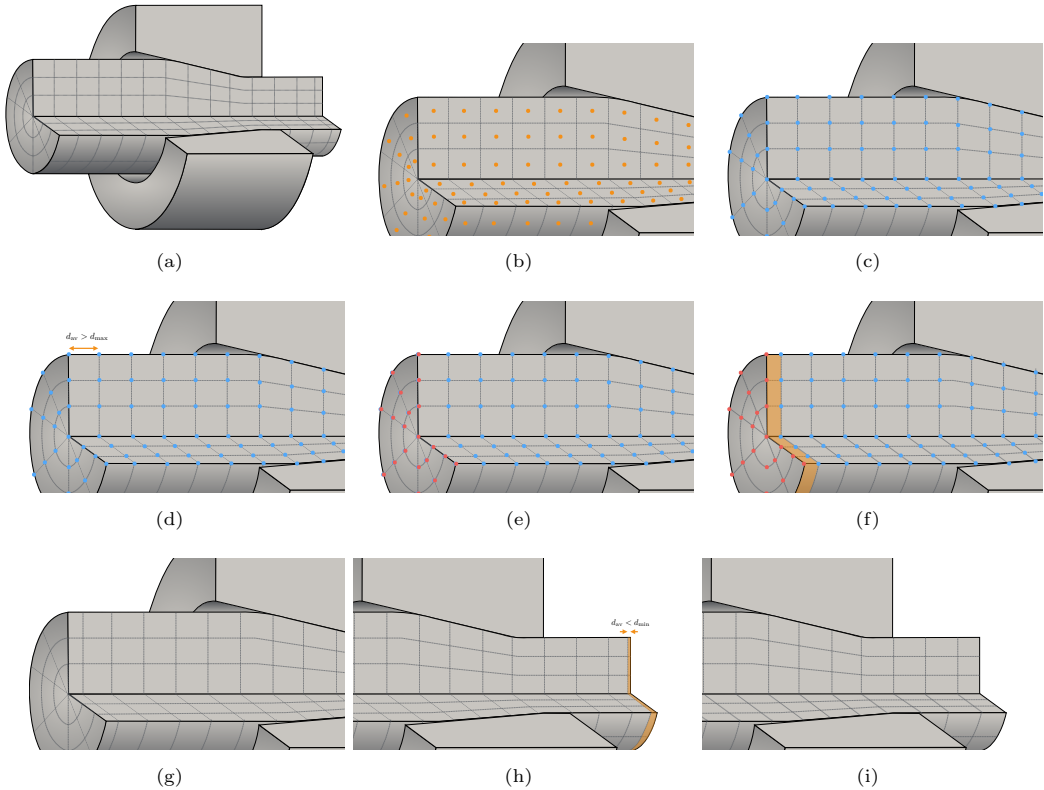


Fig. 1 Layer addition and removal mesh motion algorithm for continuous wire drawing (a). The displacement increments are calculated at the cell centre (b) and are interpolated to the vertices (c). A new layer of cells is added at the upstream boundary if the layer width is greater than d_{max} (d-g). Layers of cells are removed from the downstream boundary if the later width is less than d_{max} (h-i).

Following the layer addition and removal mesh motion algorithm, solution and derived field data at the newly added cell centres are mapped from the field data stored at the upstream boundary. This mapping approach assumes field data to have a zero gradient in the upstream direction; this assumption is valid if the upstream and downstream are chosen sufficiently far from the *active* deformation zone.

The presented layer addition-removal procedure is agnostic to the mathematical boundary conditions used at the upstream and downstream boundaries. As is demonstrated in drawing simulations, a velocity (or equivalent displacement increment) is prescribed at the downstream boundary, where the tangential traction is zero, while traction (back tension) is applied to the upstream boundary. However, other conditions can be used; for example, in rolling simulations, tractions may be applied to both upstream (back tension) and downstream (front tension) boundaries.

Note on parallelisation: The proposed solution algorithm has been implemented in the open-source toolbox OpenFOAM, where multi-CPU-core parallelisation on distributed memory systems is achieved through the domain decomposition approach. To simplify the implementation of the non-trivial topological mesh changes (addition or removal of cells) in parallel, domain decomposition approaches are limited to decomposing the workpiece into streamwise columns of cells (Figure 2). In the current approach, modified forms of the METIS [51] and scotch [52] approaches have been used to perform this decomposition. Nonetheless, there is no limitation on the decomposition of the cells in the die, as demonstrated in Figure 2.

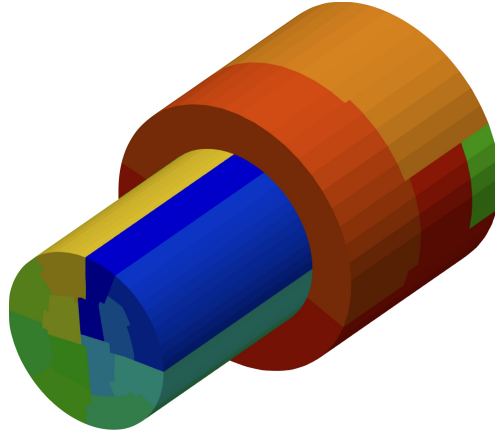


Fig. 2 Example parallel decomposition of a wire and drawing die, where the wire is decomposed into streamwise columns, indicated by the different colours. There is no limitation on the die decomposition.

3 Constitutive Damage Laws

3.1 Overview

As noted by Garrison and Moody [53], ductile fracture in metals occurs in three stages: (i) voids are nucleated at material defects, adding to pre-existing voids, if any; (ii) plastic deformations cause these voids to grow; and (iii) when large enough, these voids coalesce to form micro-cracks and macro-cracks. As noted in the introduction, local approaches for modelling ductile fracture in metal forming can classified into two approaches [9, 10]: continuum damage mechanics models and micro-mechanical models.

In *continuum* damage mechanics, an internal damage variable is used to describe the accumulation of microstructural degradation within a material due to various types of loading. This degradation is typically reflected in the increased density of internal defects, such as microcracks, dislocations, or voids. The internal damage variable is continuous, meaning it can take on any value within a given range. The *micro-mechanical* approach is also continuous in nature and posits the existence of material micro-voids. The void density is described by a *porosity* variable. Material degradation is characterised by increased porosity due to void nucleation, growth, and coalescence.

As noted by Besson [14], Cao [9] and Tekkaya et al. [10], the canonical frameworks in the continuum damage mechanics and micro-mechanical approaches are the Lemaitre [19, 20] and the Gurson-Tvergaard-Needleman (GTN) [21, 22] models, respectively.

This section provides an overview of the Lemaitre and GTN models and proposes modifications to the Lemaitre model to extend its applicability to the high hydrostatic pressure regimes characteristic of wire drawing. For comparison, a recent phase field model damage approach is also considered.

The constitutive damage laws described in this section close the system of governing equations (Equation 4) described in Section 2.2 by providing the true stress definition.

3.2 Preliminaries

Before describing these models in more detail, it is necessary to define the stress triaxiality η , the Lode angle θ and related Lode parameters [54, 55]. Extensive literature has noted the importance of stress triaxiality and Lode angle in predicting ductile fracture [9, 10, 14]. The triaxiality parameter η is given by:

$$\eta = -\frac{p}{\sigma_v} \quad (35)$$

where, as noted previously, p is the hydrostatic pressure, and $\sigma_v = \sqrt{3J_2} = \sqrt{\frac{3}{2}\text{dev}(\boldsymbol{\sigma}) : \text{dev}(\boldsymbol{\sigma})}$ is the equivalent (von Mises) stress. J_2 is the second invariant of the deviatoric stress tensor. The deviatoric operator is indicated by $\text{dev}(\bullet)$, and $:$ indicates the double-dot product.

The Lode angle, $0 \leq \theta \leq \frac{\pi}{3}$, can be physically interpreted as the degree of shear dominance in the stress state. The Lode angle can be rewritten as a function of the normalised third invariant of the deviatoric stress tensor:

$$\theta = \frac{1}{3} \arccos(\xi) \quad (36)$$

The parameter $0 \leq \xi \leq 1$ is determined as a ratio between the third invariant and the equivalent stress:

$$\xi = \left(\frac{r}{\sigma_v} \right)^3 \quad (37)$$

where r is given by:

$$r = 3 \left(\frac{3}{2} J_3 \right)^{1/3} \quad (38)$$

The third invariant of the deviatoric stress tensor is $J_3 = \det[\text{dev}(\boldsymbol{s})]$. An alternative normalised Lode angle has been proposed by Bai and Wierzbicki [54] to be

$$\bar{\theta} = 1 - \frac{6\theta}{\pi} \quad (39)$$

which ranges between -1 and 1.

The three Lode parameters (θ , ξ , and $\bar{\theta}$) are essentially equivalent but are defined to vary between different limits.

3.3 Isotropic Elastoplasticity

3.3.1 Model Formulation

In the current work, the damage models are formulated in terms of isotropic J_2 (von Mises) elastoplasticity. Extension to other forms of elastoplasticity (e.g., kinematic hardening, anisotropic/Hill yielding, distortional hardening) is possible but is outside the scope of this article. The adopted large strain elastoplasticity formulation is based on the logarithmic (Hencky) strain, as proposed by Eterovic and Bathe [56] and described in detail by Koji and Bathe [57] and de Souza Neto et al. [58]. This approach allows an additive split of the elastic and plastic strain tensors, conveniently leading to a return mapping scheme that is similar in form to those used in small-strain deformation models. In contrast, previous large-strain elastoplastic models [11, 13] implemented in the OpenFOAM software have adopted the approaches of Caminero et al. [59] and Simo and Hughes [60].

The employed isotropic J_2 elastoplastic constitutive law is defined in terms of the yield criterion

$$\Phi = \sigma_v - \sigma_y(\bar{\varepsilon}_p) \quad (40)$$

and flow rule

$$\dot{\mathbf{F}}_p \mathbf{F}_p^{-1} = \dot{\bar{\varepsilon}}_p \mathbf{R}_e^T \left[\frac{3}{2} \frac{\text{dev}(\boldsymbol{\sigma})}{\sigma_v} \right] \mathbf{R}_e \quad (41)$$

where the yield stress σ_y is a function of the hardening variable $\bar{\varepsilon}_p$, which coincides with the equivalent plastic strain $\bar{\varepsilon}_p$. The deformation gradient is decomposed into elastic and plastic components $\mathbf{F} = \mathbf{F}_e \mathbf{F}_p$ and polar decomposition of the elastic deformation gradient gives the elastic rotation \mathbf{R}_e and elastic stretch \mathbf{U}_e tensors: $\mathbf{F}_e = \mathbf{R}_e \mathbf{U}_p$.

The model is closed with the Kuhn-Tucker conditions

$$\Phi \geq 0, \quad \dot{\bar{\varepsilon}}_p \geq 0, \quad \dot{\bar{\varepsilon}}_p \Phi = 0 \quad (42)$$

and the consistency condition

$$\dot{\bar{\varepsilon}}_p \dot{\Phi} = 0 \quad (43)$$

3.3.2 Computational procedure

For each cell at every outer (Picard) iteration, the stress $\boldsymbol{\sigma}^{[m+1]}$ and history variables $(\alpha^{[m+1]}, \mathbf{F}_p^{[m+1]})$ at time step $t^{[m+1]}$ must be calculated in terms of the current displacement increment gradient $[\nabla(\Delta \mathbf{u})]^{[m+1]}$ and old-time history variables $(\alpha^{[m]}, \mathbf{F}_p^{[m]})$.

The adopted stress calculation algorithm [58] is summarised in Algorithm 2.

Algorithm 2: Large strain J_2 (von Mises) isotropic elastoplastic stress calculation algorithm [58]

(i) Update deformation gradients for a given incremental displacement

$$\mathbf{f}^{[m+1]} = \mathbf{I} + [\nabla(\Delta\mathbf{u})]^T$$

$$\mathbf{F}^{[m+1]} = \mathbf{f}^{[m+1]} \mathbf{F}^{[m]}$$

$$J^{[m+1]} = \det(\mathbf{F}^{[m+1]})$$

(ii) Compute trial elastic state

$$\mathbf{B}_e^{[m]} = \exp(2\boldsymbol{\epsilon}_e^{[m]})$$

$$\mathbf{B}_e^{\text{trial}} = \mathbf{f}^{[m+1]} \mathbf{B}_e^{[m]} (\mathbf{f}^{[m+1]})^T$$

$$\boldsymbol{\epsilon}_e^{\text{trial}} = \frac{1}{2} \ln(\mathbf{B}_e^{\text{trial}})$$

$$\bar{\boldsymbol{\epsilon}}_p^{\text{trial}} = \bar{\boldsymbol{\epsilon}}_p^{[m]}$$

$$\sigma_v^{\text{trial}} = \sqrt{3/2} ||2\mu \text{dev}(\boldsymbol{\epsilon}_e^{\text{trial}})||$$

$$\Phi^{\text{trial}} = \sigma_v^{\text{trial}} - \sigma_y(\bar{\boldsymbol{\epsilon}}_p^{\text{trial}})$$

if $\Phi^{\text{trial}} > 0$ **then**

| Go to step (iii) to solve for $\Delta\bar{\boldsymbol{\epsilon}}_p$

else

| $\Delta\bar{\boldsymbol{\epsilon}}_p = 0$ and go to step (iv)

end

(iii) Use the Newton-Raphson method to solve the yield function for $\Delta\bar{\boldsymbol{\epsilon}}_p$:

$$\sigma_v^{\text{trial}} - 3\mu\Delta\bar{\boldsymbol{\epsilon}}_p - \sigma_y(\bar{\boldsymbol{\epsilon}}_p^{[m]} + \Delta\bar{\boldsymbol{\epsilon}}_p) = 0$$

(iv) Update the constitutive variables and deviatoric stress

$$\boldsymbol{\epsilon}_e^{[m+1]} = \boldsymbol{\epsilon}_e^{\text{trial}} - \sqrt{3/2} \Delta\bar{\boldsymbol{\epsilon}}_p \frac{\text{dev}(\boldsymbol{\epsilon}_e^{\text{trial}})}{||\boldsymbol{\epsilon}_e^{\text{trial}}||}$$

$$\bar{\boldsymbol{\epsilon}}_p^{[m+1]} = \bar{\boldsymbol{\epsilon}}_p^{[m]} + \Delta\bar{\boldsymbol{\epsilon}}_p$$

$$\hat{p} = -\frac{\kappa}{J^{[m+1]}} \text{tr}(\boldsymbol{\epsilon}_e^{[m+1]})$$

$$\mathbf{s}^{[m+1]} = (1/J^{[m+1]}) 2\mu \text{dev}(\boldsymbol{\epsilon}_e^{[m+1]})$$

(v) **if** *Solve pressure equation* **then**

| Implicitly solve the pressure Poisson's equation:

$$p^{[m+1]} - \mathbb{D}\nabla^2 p^{[m+1]} = \hat{p} - \nabla \cdot (\mathbb{D}\nabla p_{[i]}^{[m+1]})$$

else

$$p^{[m+1]} = \hat{p}$$

end

(vi) Update the true (Cauchy) stress

$$\boldsymbol{\sigma}^{[m+1]} = \mathbf{s}^{[m+1]} - p^{[m+1]} \mathbf{I}$$

3.4 Lemaitre Damage Model

3.4.1 Model Formulation

The Lemaitre model describes damage using a scalar field variable D . When no damage has occurred, the damage variable D equals 0 (virgin material), whereas when the material is fully damaged, the damage variable equals 1. From a physical point of view, D can be interpreted as the area of cracks and cavities per unit surface cut by an arbitrary plane.

The Lemaitre model augments the elastoplasticity constitutive law (Equations 40 and 41) with the inclusion of an evolution law for D . In addition, the reciprocal of $(1 - D)$ is introduced to the

yield function and flow rules:

$$\Phi = \frac{\sigma_v}{1-D} - \sigma_y(\bar{\varepsilon}_p) \quad (44)$$

$$\dot{\mathbf{F}}_p \mathbf{F}_p^{-1} = \frac{\dot{\varepsilon}_p}{1-D} \mathbf{R}_e^T \left[\frac{3 \operatorname{dev}(\boldsymbol{\sigma})}{\sigma_v} \right] \mathbf{R}_e \quad (45)$$

$$\dot{D} = \frac{\dot{\varepsilon}_p}{1-D} \left(\frac{-Y}{S_0} \right)^b \quad (46)$$

where S_0 (dimensions of stress) and b (dimensionless) are material parameters. The energy release rate Y , which gives the energy dissipated due to the phenomenon of damage, is given by [20]

$$Y = -\frac{\sigma_v^2}{2E} \left[\frac{2}{3}(1+\nu) + 3(1-2\nu)\eta^2 \right] \quad (47)$$

where E is Young's modulus and ν is Poisson's ratio, and the dependence on Y on triaxiality η is explicitly clear.

Triaxiality and Lode Angle Dependence

The classic Lemaitre model does not distinguish between positive and negative triaxiality (η is squared in Equation 47); consequently, it can overpredict damage in wire drawing processes where triaxiality can be highly negative (high negative pressures). One remedy is to employ a triaxiality *cut-off* [61], which disallows damage evolution for highly negative triaxiality values:

$$\dot{D} = \begin{cases} 0 & \text{if } \eta \leq -\frac{1}{3} \\ \frac{\dot{\varepsilon}_p}{1-D} \left(\frac{-Y}{S_0} \right)^b & \text{if } \eta > -\frac{1}{3} \end{cases} \quad (48)$$

Rather than use a triaxiality cut-off, Malcher and co-workers [62–64] proposed that the parameter S_0 be a function of triaxiality η as well as Lode angle ξ . This approach has shown an ability to accurately predict fracture for a range of loading conditions at both low and high triaxiality values and for various shear stress states. The Malcher et al. form of damage evolution is achieved by making S_0 in Equation 46 a function of η and ξ :

$$S(\eta, \xi) = \frac{S_{0.33}}{3|\eta| + \frac{S_{0.33}}{S_{0.0}}(1-\xi^2)} \quad (49)$$

where $S_{0.33}$ and $S_{0.0}$ are material parameters determined based on pure tensile loading ($S_{0.33}$) and pure shear loading ($S_{0.0}$).

Despite its success, this formulation's weakness is that it does not distinguish between positive and negative triaxiality values, which is critical for wire drawing. To overcome this limitation, a function for $S(\eta, \xi)$ is proposed here, inspired by the Ko et al. [65] uncoupled damage law. The Ko et al. [65] criterion has shown an ability to predict fracture in both wire drawing processes [66] and in the hub-hole expanding process [65]. For wire drawing, $\xi \approx 1.0$ at the wire axis, where fracture typically originates [66]. For this reason, the proposed function does not incorporate a dependency

on ξ , and the final expression for S proposed here takes the form

$$S(\eta) = \frac{2S_0}{1.0 + 3\eta} \quad (50)$$

Crack Closure Effects

An additional limitation of the classic Lemaitre damage model is that it does not distinguish between tensile and compressive stress states, whereas it is known from experiments that tensile stresses are considerably more conducive to crack growth than compressive stresses [67]. To overcome this shortcoming, some authors assume no crack growth in compressive stress states [68]; however, this does not account for the partial closure of micro-defects under compressive stress states. This effect causes a greater material area to bear the compressive load. As a result, the material may exhibit a partial or complete recovery of its stiffness, depending on the specific conditions [69]. This approach also does not account for the fact that some crack growth can occur in compressive states [70].

Consequently, an *enhanced* Lemaitre model with crack closure effects has been proposed [69, 71]. In this approach, the energy release rate Y (Equation 47) is rewritten to account for the differing contributions of tensile and compressive stresses:

$$Y = \frac{-1}{2E(1-D)} [(1+\nu)\boldsymbol{\sigma}^+ : \boldsymbol{\sigma}^+ - \nu \langle \text{tr}(\boldsymbol{\sigma}) \rangle^2] - \frac{h}{2E(1-hD)} [(1+\nu)\boldsymbol{\sigma}^- : \boldsymbol{\sigma}^- - \nu \langle -\text{tr}(\boldsymbol{\sigma}) \rangle^2] \quad (51)$$

where Macaulay brackets are indicated by $\langle \bullet \rangle$. The parameter $0 \leq h \leq 1$ accounts for the crack closure phenomenon; here, we take $h = 0.2$ as is common for steels [61, 72, 73]). The positive and negative stress components are defined as

$$\boldsymbol{\sigma}^+ = \sum_{i=1}^3 \langle \sigma_i \rangle \mathbf{e}_i \otimes \mathbf{e}_i \quad (52)$$

$$\boldsymbol{\sigma}^- = \sum_{i=1}^3 \langle -\sigma_i \rangle \mathbf{e}_i \otimes \mathbf{e}_i \quad (53)$$

where σ_i are the principal stresses, $\{\mathbf{e}_1, \mathbf{e}_2, \mathbf{e}_3\}$ are the orthonormal basis vectors, and $\boldsymbol{\sigma} = \boldsymbol{\sigma}^+ + \boldsymbol{\sigma}^-$.

A simplified form of the crack-closure model [69] is employed in this work, whereby this definition of decomposed stress is only used in the damage evolution calculation.

Non-Local Damage

One general limitation of damage models is that due to the strain softening behaviour, predictions may suffer from mesh size and orientation dependency in localised strain zones [74–76]. To rectify this, an implicit *non-local* damage variable \bar{D} is introduced as in Peerlings et al. [74, 75] and Geers

et al. [76]. This is related to the local damage variable D through the implicit diffusion equation:

$$\bar{D} - l_c^2 \nabla^2 \bar{D} = D \quad (54)$$

where l_c is a characteristic length scale which controls the area over which the local damage is diffused. This equation can be viewed as a smoothing equation (\bar{D} is a spatially smoothed version of D), which has the effect of mitigating the mesh dependency. To discretise this equation using the cell-centred finite volume method, we express it in integral form:

$$\underbrace{\int_{\Omega_u} \bar{D} d\Omega_u}_{\text{implicit}} - \underbrace{\oint_{\Gamma_u} \mathbf{n}_u \cdot (l_c^2 \nabla \bar{D}) d\Gamma_u}_{\text{implicit}} = \underbrace{\int_{\Omega_u} D d\Omega_u}_{\text{explicit}} \quad (55)$$

where the divergence theorem has been used to express the diffusion term (second on the left-hand side) in terms of a surface integral. As indicated by underbraces, the terms on the left-hand side are treated implicitly (coefficients in the linear system matrix), while the term of the right-hand side is treated explicitly in a deferred correction manner using values from the previous outer (Picard) iteration.

Assuming a linear variation of \bar{D} within cell P , the mid-point rule is used to approximate the first term on the left-hand side of Equation 55:

$$\underbrace{\int_{\Omega_u} \bar{D} d\Omega_u}_{\text{implicit}} \approx \bar{D}_P \Omega_{u_P} \quad (56)$$

This term is treated implicitly with the resulting linear system matrix coefficient contribution being Ω_{u_P} on the diagonal.

Similarly, the right-hand side term is approximated using the mid-point rule:

$$\underbrace{\int_{\Omega_u} D d\Omega_u}_{\text{explicit}} \approx D_P \Omega_{u_P} \quad (57)$$

where this term is treated in a deferred correction manner, where $D_P \Omega_{u_P}$ is added to the linear system source.

The surface integral term (second on the left-hand side) is discretised by assuming a linear various of the integrand over the face and applying the mid-point rule about the face centre f :

$$\begin{aligned} \underbrace{\oint_{\Gamma_u} \mathbf{n}_u \cdot (l_c^2 \nabla \bar{D}) d\Gamma_u}_{\text{implicit}} &= \sum_{f \in N_f} \int_{\Gamma_u} \mathbf{n}_u \cdot (l_c^2 \nabla \bar{D}) d\Gamma_u \\ &\approx \sum_{f \in N_f} l_c^2 |\Delta_{u_f}| \left(\frac{\bar{D}_{N_f} - \bar{D}_P}{|\mathbf{d}_f|} \right) |\Gamma_{u_f}| \\ &\quad + \sum_{f \in N_f} l_c^2 \mathbf{k}_{u_f} \cdot (\nabla \bar{D})_f |\Gamma_{u_f}| \end{aligned} \quad (58)$$

This equation is solved with zero-flux Neumann boundary conditions on all boundaries, that is, $\mathbf{n} \cdot \nabla \bar{D} = 0$. Consequently, the contributions coming from boundary faces are dropped.

For each computational cell, the resulting algebraic equation becomes:

$$\left(\Omega_{u_P} + \sum_{f \in N_f} \frac{l_c^2 |\Delta_{u_f}| |\Gamma_{u_f}|}{|\mathbf{d}_f|} \right) \bar{D}_P - \sum_{f \in N_f} \frac{l_c^2 |\Delta_{u_f}| |\Gamma_{u_f}|}{|\mathbf{d}_f|} \bar{D}_{N_f} = D_P \Omega_{u_P} + \sum_{f \in N_f} l_c^2 \mathbf{k}_{u_f} \cdot (\nabla \bar{D})_f |\Gamma_{u_f}| \quad (59)$$

in terms of the unknown non-local damage at the centres of cell P and the neighbouring cells N_f . A similar algebraic equation is formed for each cell in the mesh and assembled into a system of linear equations. This equation is iteratively solved once per outer (Picard) iteration resulting in an implicit discretisation that is balanced at convergence of the outer loop. The resulting sparse matrix is strongly diagonally dominant due to the inclusion of the Ω_{u_P} , ensuring rapid convergence of the iterative linear solver. In the limit of l_c going to zero, the system of equations become decoupled and $\bar{D}_P = D_P$ as expected.

Effective Non-Local Damage

An additional issue with the classic non-local Lemaitre damage model is that it can lead to a non-physical response when the material reaches ultimate failure. The non-local equation diffuses the damage, reducing the rate at which it evolves after a certain point. In reality, it would be expected for a piece of material to quickly become fully damaged as it enters the void coalescence stage of failure. Furthermore, fully degraded cells continue to contribute to the damage growth in the surrounding cells through the non-local damage field, which is nonphysical.

To mitigate these issues, this work introduces an *effective* non-local damage field \bar{D}_{eff} . This field is set such that it is equivalent to the non-local damage field unless, for a given cell, the non-local damage field exceeds the critical damage value D_c (the damage at which failure occurs). At this critical value, the effective non-local damage is set *close* to 1 to represent fully degraded material. A value of 0.99 is proposed here instead of 1 to allow small residual stresses that aid convergence. An additional change to the classic approach is the growth of the local damage D , for a given cell, is disallowed if the effective non-local damage of this cell exceeds the critical damage value D_c .

The implication of this proposed effective non-local damage approach is examined in Section 4.4.6.

3.4.2 Computational Procedure

A deferred (defect) algorithm is developed in this work to solve Equations 44-46. At every outer iteration, the plastic increment is solved implicitly, with the value for the damage variable fixed from the previous outer iteration. The damage rate equation (Equation 46) is then solved in a deferred-correction manner using the damage from the previous iteration $D_{[i]}$, where $[i]$ indicates the previous outer iteration and $[i + 1]$ indicates the current outer iteration. This approach avoids

using a 2×2 matrix (or an even higher dimension matrix if one were to solve for anisotropic plasticity or plasticity incorporating kinematic hardening) that would be needed if both the damage and the plastic increment were solved for simultaneously. By not requiring the solution of plasticity and damage simultaneously, the mathematics are simplified when solving for more complex formulations of the Lemaître damage and non-local damage evolution. In addition, the proposed approach aligns with the philosophy of the overall segregated solution procedure. Within each time step, $D_{[i]}^{[m+1]}$ converges to $D_{[i+1]}^{[m+1]}$. Note that the overall solution algorithm is still implicit in time.

This stress calculation procedure for the Lemaître damage model using the proposed effective non-local damage model is summarised in Algorithm 3. This approach reverts to the *classic* non-local damage Lemaître procedure with three changes:

- (a) The effective non-local damage \bar{D}_{eff} is set always equal to the non-local damage \bar{D} – modification to step (viii);
- (b) The local damage D is not limited in its growth by the effective non-local damage \bar{D}_{eff} – modification to step (vii).
- (c) The local damage D is set to be 0.99 when it becomes greater than D_c – modification to step (vii)

The impact of the proposed effective non-local damage approach is examined in Section 4.4.6.

3.5 Gurson-Tvergaard-Needleman Model

3.5.1 Model Formulation

Gurson [21] proposed the canonical micro-mechanical framework for ductile damage prediction and provided the basis for various derived models [9, 10, 14, 77, 78]. As noted above, this model posits the existence of micro-voids in the material, the density of which is described by a variable denoted as porosity f . Material degradation is characterised by increasing porosity due to the growth of these voids. Gurson's framework was further developed by Tvergaard and Needleman [22] to account for the void nucleation and coalescence, leading to the Gurson-Tvergaard-Needleman (GTN) model.

The GTN model is described by a yield equation, flow rule (with deviatoric and volumetric components), consistency condition, and porosity evolution equations:

$$\Phi = \left(\frac{\sigma_v}{\sigma_y} \right)^2 + 2q_1 f_* \cosh \left(\frac{3q_2 p}{2\sigma_y} \right) - (1 + q_3 f_*^2) \quad (60)$$

$$\dot{\varepsilon}_p = \frac{1}{(1-f)\sigma_y} (\sigma_v \dot{\varepsilon}_{\text{dev}} - p \dot{\varepsilon}_{\text{vol}}) \quad (61)$$

$$\dot{\varepsilon}_{\text{vol}} \frac{\partial \Phi}{\partial \sigma_v} + \dot{\varepsilon}_{\text{dev}} \frac{\partial \Phi}{\partial p} = 0 \quad (62)$$

$$\dot{f} = (1 - f) \text{tr}(\dot{\varepsilon}_p) + A \dot{\varepsilon}_p \quad (63)$$

Algorithm 3: Effective non-local damage Lemaitre model stress calculation algorithm

(i) Update deformation gradients for a given incremental displacement

$$\begin{aligned}\mathbf{f}^{[m+1]} &= \mathbf{I} + [\nabla(\Delta\mathbf{u})]^T \\ \mathbf{F}^{[m+1]} &= \mathbf{f}^{[m+1]}\mathbf{F}^{[m]} \\ J^{[m+1]} &= \det(\mathbf{F}^{[m+1]})\end{aligned}$$

(ii) Compute trial elastic state

$$\begin{aligned}\mathbf{B}_e^{[m]} &= \exp(2\boldsymbol{\varepsilon}_e^{[m]}) \\ \mathbf{B}_e^{\text{trial}} &= \mathbf{f}^{[m+1]}\mathbf{B}_e^{[m]} (\mathbf{f}^{[m+1]})^T \\ \boldsymbol{\varepsilon}_e^{\text{trial}} &= \frac{1}{2} \ln(\mathbf{B}_e^{\text{trial}}) \\ \bar{\boldsymbol{\varepsilon}}_p^{\text{trial}} &= \bar{\boldsymbol{\varepsilon}}_p^{[m]} \\ \sigma_v^{\text{trial}} &= \sqrt{3/2} ||2\mu \operatorname{dev}(\boldsymbol{\varepsilon}_e^{\text{trial}})|| \\ \Phi^{\text{trial}} &= \sigma_v^{\text{trial}} - \sigma_y(\bar{\boldsymbol{\varepsilon}}_p^{\text{trial}})\end{aligned}$$

```

if  $\Phi^{\text{trial}} > 0$  then
| Go to step (iii) to solve for  $\Delta\bar{\boldsymbol{\varepsilon}}_p$ 
else
|  $\Delta\bar{\boldsymbol{\varepsilon}}_p = 0$  and go to step (iv)
end

```

(iii) Use the Newton-Raphson method to solve the yield function for $\Delta\bar{\boldsymbol{\varepsilon}}_p$:

$$\sigma_v^{\text{trial}} - \frac{3\mu\Delta\bar{\boldsymbol{\varepsilon}}_p}{1 - \bar{D}_{\text{eff}[i]}^{[m+1]}} - \sigma_y(\bar{\boldsymbol{\varepsilon}}_p^{[m]} + \Delta\bar{\boldsymbol{\varepsilon}}_p) = 0$$

(iv) Update constitutive variables and deviatoric stress

$$\begin{aligned}\boldsymbol{\varepsilon}_e^{[m+1]} &= \boldsymbol{\varepsilon}_e^{\text{trial}} - \sqrt{\frac{3}{2}} \frac{\Delta\bar{\boldsymbol{\varepsilon}}_p}{1 - \bar{D}_{\text{eff}[i]}^{[m+1]}} \frac{\operatorname{dev}(\boldsymbol{\varepsilon}_e^{\text{trial}})}{||\boldsymbol{\varepsilon}_e^{\text{trial}}||} \\ \bar{\boldsymbol{\varepsilon}}_p^{[m+1]} &= \bar{\boldsymbol{\varepsilon}}_p^{[m]} + \Delta\bar{\boldsymbol{\varepsilon}}_p\end{aligned}$$

$$\hat{p} = -\left(1 - \bar{D}_{\text{eff}[i]}^{[m+1]}\right) \frac{\kappa}{J^{[m+1]}} \operatorname{tr}(\boldsymbol{\varepsilon}_e^{[m+1]})$$

$$\mathbf{s}^{[m+1]} = \left(1 - \bar{D}_{\text{eff}[i]}^{[m+1]}\right) \frac{1}{J^{[m+1]}} 2\mu \operatorname{dev}(\boldsymbol{\varepsilon}_e^{[m+1]})$$

(v) if Solve pressure equation then

$$\left| \begin{array}{l} \text{Implicitly solve the pressure Poisson's equation:} \\ p^{[m+1]} - \mathbb{D}\nabla^2 p^{[m+1]} = \hat{p} - \nabla \cdot (\mathbb{D}\nabla p_{[i]}^{[m+1]}) \end{array} \right.$$

else

$$p^{[m+1]} = \hat{p}$$

end

(vi) Update the true (Cauchy) stress

$$\boldsymbol{\sigma}^{[m+1]} = \mathbf{s}^{[m+1]} - p^{[m+1]}\mathbf{I}$$

(vii) Update the local damage (use the modified form for Y if $h > 0$)

$$D_{[i+1]}^{[m+1]} = \begin{cases} D^{[m]} & \text{if } \eta \leq -\frac{1}{3} \text{ or } \bar{D}_{\text{eff}[i]}^{[m+1]} \geq D_c \\ D^{[m]} + \frac{\bar{\boldsymbol{\varepsilon}}_p}{1 - D_{[i]}^{[m+1]}} \left(\frac{-Y}{S(\eta, \xi)}\right)^b & \text{if } \eta > -\frac{1}{3} \text{ and } \bar{D}_{\text{eff}[i]}^{[m+1]} < D_c \end{cases}$$

(viii) Implicitly solve diffusion equation for non-local damage

$$\bar{D}^{[m+1]} - l_c^2 \nabla^2 \bar{D}^{[m+1]} = D_{[i+1]}^{[m+1]}$$

(ix) Update the effective damage

$$\bar{D}_{\text{eff}[i+1]}^{[m+1]} = \begin{cases} \bar{D}^{[m+1]} & \text{if } \bar{D}^{[m+1]} \leq D_c \\ 0.99 & \text{if } \bar{D}^{[m+1]} > D_c \end{cases}$$

where q_1 , q_2 and q_3 are dimensionless material parameters. The effective void fraction f_* , which accounts for void coalescence, is

$$f_* = \begin{cases} f & \text{if } f \leq f_c \\ f_c + (f - f_c) \frac{f_u - f_c}{f_f - f_c} & \text{if } f > f_c \end{cases} \quad (64)$$

where f_c is the void volume fraction at which void coalescence begins, f_u is the ultimate volume fraction, and f_f is the void volume fraction at fracture.

The rate of volumetric plastic strain and equivalent deviatoric plastic strain are given, respectively, by

$$\dot{\varepsilon}_{\text{vol}} = -\dot{\bar{\varepsilon}}_p \frac{\partial \Phi}{\partial p} \quad (65)$$

$$\dot{\varepsilon}_{\text{dev}} = \dot{\bar{\varepsilon}}_p \frac{\partial \Phi}{\partial \sigma_v} \quad (66)$$

The dimensionless coefficient A is chosen to ensure void nucleation follows a normal distribution [68]:

$$A = \begin{cases} \frac{f_n}{S_n \sqrt{2\pi}} \exp\left[-\frac{1}{2}\left(\frac{\bar{\varepsilon}_p - \varepsilon_n}{S_n}\right)\right] & \text{if } p < 0 \\ 0 & \text{if } p \geq 0 \end{cases} \quad (67)$$

where f_n determines the total void fraction possible, ε_n is the mean nucleation strain, and S_n is the nucleation strain standard deviation.

Non-Local Porosity

Like the Lemaitre model, mesh dependency in the GTN model can be mitigated by introducing non-local damage variables [79, 80]. In the case of the GTN model, a non-local (smoothed) porosity variable \bar{f} is determined using a non-local gradient (smoothing) equation:

$$\bar{f} - l_c^2 \nabla^2 \bar{f} = f \quad (68)$$

As before, this equation can be discretised using the described cell-centred finite volume method and zero-flux Neumann boundary conditions.

3.5.2 Computational Procedure

For the GTN model, the elastoplasticity stress calculation is extended to determine porosity f in addition to stress and plastic strain. The adopted computational algorithm is shown in Algorithm 4. As in the Lemaitre computational procedure, we propose a deferred correction algorithm to solve the system of equations: Equations 60, 61 and 62 are solved implicitly for the variables ε_{vol} , ε_{dev} and $\bar{\varepsilon}_p$ using a Newon-Raphson method, while the porosity f (Equation 63) is calculated in a deferred-correction manner. Once again, the overall procedure is implicit in time.

Algorithm 4: GTN damage model stress calculation algorithm

(i) Update deformation gradients for a given incremental displacement

$$\begin{aligned}\mathbf{f}^{[m+1]} &= \mathbf{I} + [\nabla(\Delta\mathbf{u})]^T \\ \mathbf{F}^{[m+1]} &= \mathbf{f}^{[m+1]}\mathbf{F}^{[m]} \\ J^{[m+1]} &= \det(\mathbf{F}^{[m+1]})\end{aligned}$$

(ii) Compute trial elastic state

$$\begin{aligned}\mathbf{B}_e^{[m]} &= \exp(2\boldsymbol{\varepsilon}_e^{[m]}) \\ \mathbf{B}_e^{\text{trial}} &= \mathbf{f}^{[m+1]}\mathbf{B}_e^{[m]}(\mathbf{f}^{[m+1]})^T \\ \boldsymbol{\varepsilon}_e^{\text{trial}} &= \frac{1}{2}\ln[\mathbf{B}_e^{\text{trial}}] \\ p^{\text{trial}} &= -\kappa \operatorname{tr}(\boldsymbol{\varepsilon}_e^{\text{trial}}) \\ \mathbf{s}^{\text{trial}} &= 2\mu \operatorname{dev}(\boldsymbol{\varepsilon}_e^{\text{trial}}) \\ \sigma_v^{\text{trial}} &= \sqrt{3/2} ||2\mu \operatorname{dev}(\boldsymbol{\varepsilon}_e^{\text{trial}})|| \\ \mathbf{n} &= \frac{3}{2} \frac{\mathbf{s}^{\text{trial}}}{\sigma_v^{\text{trial}}} \\ \Phi^{\text{trial}} &= \left(\frac{\sigma_v^{\text{trial}}}{\sigma_y}\right)^2 + q_1 f_{*[i]}^{[m+1]} \cosh\left(\frac{3q_2 p^{\text{trial}}}{2\sigma_y}\right) - (1 + q_3 f_{*[i]}^{[m+1]2})\end{aligned}$$

if $\Phi^{\text{trial}} > 0$ **then**
| Go to step (iii)

else
| set $\Delta\varepsilon_{\text{vol}} = \Delta\varepsilon_{\text{dev}} = \Delta\bar{\varepsilon}_p = 0$ and $\Delta\boldsymbol{\varepsilon}_p = \mathbf{0}$. Go to step (iv)

end

(iii) Enter small strain return map and solve the system of equations (Equations 49-51) for $\Delta\varepsilon_h^{[m+1]}$, $\Delta\varepsilon_q^{[m+1]}$ and $\Delta\bar{\varepsilon}_{[m+1]}^p$

(iv) Update the constitutive variables

$$\begin{aligned}\bar{\varepsilon}_p^{[m+1]} &= \bar{\varepsilon}_p^{[m]} + \Delta\bar{\varepsilon}_p \\ \boldsymbol{\varepsilon}_p^{[m+1]} &= \boldsymbol{\varepsilon}_p^{[m]} + \Delta\boldsymbol{\varepsilon}_p \\ \boldsymbol{\varepsilon}_e^{[m+1]} &= \boldsymbol{\varepsilon}^{\text{trial}} - (1/3)\Delta\varepsilon_{\text{vol}}^{[m+1]}\mathbf{I} - \Delta\varepsilon_{\text{dev}}^{[m+1]}\mathbf{n} \\ \hat{p} &= (1/J^{[m+1]}) (p_{\text{trial}} + \kappa\Delta\varepsilon_{\text{vol}}^{[m+1]}) \\ \mathbf{s}^{[m+1]} &= (1/J^{[m+1]}) [2/3 (\sigma_v^{\text{trial}} - 3\mu\Delta\varepsilon_{\text{dev}}^{[m+1]}) \mathbf{n}]\end{aligned}\tag{69}$$

(v) **if** *Solve pressure equation* **then**

| Implicitly solve the pressure Poisson's equation:

$$p^{[m+1]} - \mathbb{D}\nabla^2 p^{[m+1]} = \hat{p} - \nabla \cdot (\mathbb{D}\nabla p_{*[i]}^{[m+1]})\tag{70}$$

else

$$p^{[m+1]} = \hat{p}\tag{71}$$

end

(vi) Update the true (Cauchy) stress

$$\boldsymbol{\sigma}^{[m+1]} = \mathbf{s}^{[m+1]} - p^{[m+1]}\mathbf{I}$$

(vii) Calculate the porosity $f_{[i+1]}^{[m+1]}$ and the effective porosity $f_{*[i+1]}^{[m+1]}$:

$$f^{[m+1]} = f^{[m]} + (1 - f_{[i]}^{[m+1]}) \operatorname{tr}(\dot{\boldsymbol{\varepsilon}}_p^{[m+1]}) + A\dot{\bar{\varepsilon}}_p^{[m+1]}\tag{72}$$

$$f^{*[m+1]} = \begin{cases} f^{[m+1]} & \text{if } f^{[m+1]} \leq f_c \\ f_c + (f^{[m+1]} - f_c) \frac{f_u - f_c}{f_f - f_c} & \text{if } f^{[m+1]} > f_c \end{cases}\tag{73}$$

(viii) Implicitly solve non-local porosity equation:

$$\tilde{f}^{[m+1]} - l_c^2 \nabla^2 \tilde{f}^{[m+1]} = f^{[m+1]}\tag{74}$$

3.6 Phase Field Fracture Model

3.6.1 Model Formulation

In recent years, phase field approaches have received much attention for the prediction of fracture and failure [23–27, 81, 82], showing an ability to predict complex crack patterns, including

branching and merging in both two and three dimensions [81, 82]. In this method, sharp cracks are *regularised* over a continuum, leading to a system of partial differential equations that are relatively simple to implement in finite element, finite volume and related solvers.

The phase field method for damage, initially proposed by Francfort and Marigo [83] to describe brittle fracture, is based on a variational approach to minimise a Griffiths theory potential energy functional. This approach leads to a Mumford-Shah [84] type energy potential that can be approximated by a phase-field formulation following the work of Ambrosio and Tortorelli [85]. This approximation was adopted by Bourdin et al. [86] to facilitate numerical solutions of the variational formulation and further extended by Miehe et al. [82], who derived the phase field approach from continuum mechanics and thermodynamic arguments. Miehe et al. [82] also added an important mechanism for distinguishing between tensile and compressive effects on crack growth, as well as including a history variable \mathcal{H} , ensuring the irreversibility of crack growth. Several studies have shown the ability of these models to produce results consistent with benchmark fracture cases [81, 82].

The phase field approach has since been extended to ductile fracture by Ambati et al. [23], Borden et al. [24] and Miehe et al. [25]. The approach from Ambati et al. [23] involves incorporating a plastic strain dependency in the elastic degradation function while the approach from Miehe et al. [25] incorporates the plastic strain energy into the crack driving variable \mathcal{H} . Borden et al. [24] uses a similar approach to Miehe et al. [25] by incorporating the plastic strain into the crack driving variable \mathcal{H} while also introducing a plastic degradation function to ensure that fracture is preceded by large plastic strains, as is seen experimentally.

In this work, the approach from Borden et al. [24] is chosen to be most suitable, given the large plastic strains expected in wire drawing. The strong differential form of the phase field equation is given by:

$$\frac{G_c}{2l} (d - 4l^2 \nabla^2 d) = \mathcal{H} \quad (75)$$

where $0 < d \leq 1$ is the damage variable, with $d = 0$ characterising the unbroken state and $d = 1$ characterising the fully broken state. The variable d is conceptually similar to the damage variable D used in the Lemaître model and the porosity f in the GTN model, with d being a macroscopic variable that characterises the growth of micro-voids and micro-cracks. The critical fracture energy per unit area is given by G_c . The parameter l is a length-scale variable that regularises the crack surface. It is typically chosen as a function of the local element/cell size. The crack driving variable \mathcal{H} is

$$\mathcal{H} = -2d \max [\psi_e(\boldsymbol{\varepsilon}^e), \bar{\psi}_e(\boldsymbol{\varepsilon}^e)] - 2d\langle\psi_p(\bar{\boldsymbol{\varepsilon}}^p) - w_0\rangle \quad (76)$$

where $\psi_e(\boldsymbol{\varepsilon}^e)$ is the current elastic energy contribution, and $\bar{\psi}_e(\boldsymbol{\varepsilon}^e)$ is a history variable which gives the largest value reached by the elastic energy contribution in time. The elastic energy contribution $\psi_e(\boldsymbol{\varepsilon}^e)$ is decomposed into positive and negative components, such that only positive elastic strain energy contributes towards the crack driving energy [87]:

$$\psi_e = (1 - d^2) \psi_e^+(\boldsymbol{\varepsilon}_e) + \psi_e^-(\boldsymbol{\varepsilon}_e) \quad (77)$$

$$\psi_e^+(\boldsymbol{\varepsilon}_e) = \frac{\kappa}{2} \langle \text{tr}(\boldsymbol{\varepsilon}_e) \rangle^2 + \mu \text{dev}(\boldsymbol{\varepsilon}_e) : \text{dev}(\boldsymbol{\varepsilon}_e) \quad (78)$$

$$\psi_e^-(\boldsymbol{\varepsilon}_e) = \frac{\kappa}{2} \langle -\text{tr}(\boldsymbol{\varepsilon}_e) \rangle^2 \quad (79)$$

The plastic energy contribution to the crack growth $\psi_p(\bar{\varepsilon}^p)$ is given by [88]:

$$\psi_p(\bar{\varepsilon}^p) = \int_0^{\bar{\varepsilon}^p} \sigma_y d\bar{\varepsilon}^p \quad (80)$$

and w_0 is the plastic work threshold, below which the plastic strain will not contribute to crack growth.

Finally, the isotropic J_2 yield function (Equation 40) is modified as [24]

$$\Phi = \sigma'_v - (1 - d^2) \sigma_y (\bar{\varepsilon}_p) \quad (81)$$

where

$$\sigma'_v = \sqrt{3/2 \mathbf{s}' : \mathbf{s}'} \quad (82)$$

$$\mathbf{s}' = (1 - d^2) 2\mu \operatorname{dev}(\boldsymbol{\varepsilon}_e) \quad (83)$$

Similar to the non-local equations in the Lemaitre and GTN models, in this work, the phase field equation (Equation 75) is discretised using the described cell-centred finite volume method, and zero-flux Neumann boundary conditions. To facilitate the cell-centred finite volume method, we express the phase field equation in integral form:

$$\underbrace{\int_{\Omega_u} d d\Omega_u}_{\text{implicit}} - \underbrace{\oint_{\Gamma_u} \mathbf{n}_u \cdot (4l^2 \nabla d) d\Gamma_u}_{\text{implicit}} = \underbrace{\int_{\Omega_u} \frac{2l}{G_c} \mathcal{H} d\Omega_u}_{\text{explicit}} \quad (84)$$

where both sides have been multiplied by $\frac{2l}{G_c}$ and the divergence theorem has been used to express the diffusion term (second on the left-hand side) in terms of a surface integral.

This equation is applied to each cell and discretised in the same fashion as described for the the non-local damage equation (Equation 55), where the terms on the left-hand side are discretised implicitly and the term on the right is treated in a deferred correction manner. The resulting algebraic equation for each computational cell becomes:

$$\left(\Omega_{u_P} + \sum_{f \in N_f} \frac{4l^2 |\Delta_{u_f}| |\Gamma_{u_f}|}{|\mathbf{d}_f|} \right) d_P - \sum_{f \in N_f} \frac{4l^2 |\Delta_{u_f}| |\Gamma_{u_f}|}{|\mathbf{d}_f|} d_{N_f} = \frac{2l}{G_c} \mathcal{H} \Omega_{u_P} + \sum_{f \in N_f} l_c^2 \mathbf{k}_{u_f} \cdot (\nabla d)_f |\Gamma_{u_f}| \quad (85)$$

in terms of the unknown phase field variable at the centres of cell P and the neighbouring cells N_f . Like in the case of the non-local damage equation, this algebraic equation is formed for each cell in the mesh and assembled into a system of linear equations, which is iteratively solved once per outer (Picard) iteration.

3.6.2 Computational Procedure

Like the Lemaitre and GTN procedures, a deferred-correction procedure is adopted here to incorporate the phase (damage) evolution equation. Within each outer iteration, the elastoplastic quantities are calculated using the latest available phase field variable $d_{[i]}^{[m+1]}$ from the previous outer iteration i . Subsequently, the phase field equation (Equation 75) is solved using the latest available stress and strain fields. The algorithm for the phase field stress calculation procedure is given in Algorithm 5.

Algorithm 5: Phase field damage model stress calculation algorithm

(i) Update deformation gradients for a given incremental displacement

$$\begin{aligned}\mathbf{f}^{[m+1]} &= \mathbf{I} + [\nabla(\Delta\mathbf{u})]^T \\ \mathbf{F}^{[m+1]} &= \mathbf{f}^{[m+1]}\mathbf{F}^{[m]} \\ J^{[m+1]} &= \det(\mathbf{F}^{[m+1]})\end{aligned}$$

(ii) Compute trial elastic state

$$\begin{aligned}\mathbf{B}_e^{[m]} &= \exp(2\boldsymbol{\varepsilon}_e^{[m]}) \\ \mathbf{B}_e^{\text{trial}} &= \mathbf{f}^{[m+1]}\mathbf{B}_e^{[m]}(\mathbf{f}^{[m+1]})^T \\ \boldsymbol{\varepsilon}_e^{\text{trial}} &= \frac{1}{2} \ln(\mathbf{B}_e^{\text{trial}}) \\ \sigma_v^{\text{trial}} &= (1 - d_{[i]}^{[m+1]2}) \sqrt{3/2} ||2\mu \text{dev}(\boldsymbol{\varepsilon}_e)|| \\ \Phi^{\text{trial}} &= \sigma_v^{\text{trial}} - (1 - d_{[i]}^{[m+1]2}) \sigma_y(\bar{\varepsilon}_p^{[m]})\end{aligned}$$

```

if  $\Phi_{\text{trial}} > 0$  then
| Go to step (iii) to solve for  $\Delta\bar{\varepsilon}_p$ 
else
|  $\Delta\bar{\varepsilon}_p = 0$  and go to step (iv)
end

```

(iii) Use the Newton-Raphson to solve the yield equation for the equivalent plastic strain increment $\Delta\bar{\varepsilon}_p$:

$$\sigma_v^{\text{trial}} - (1 - d_{[i]}^{[m+1]2}) 3\mu \Delta\bar{\varepsilon}_p - (1 - d_{[i]}^{[m+1]2}) \sigma_y(\bar{\varepsilon}_p^{[m]} + \Delta\bar{\varepsilon}_p) = 0$$

(iv) Update the constitutive variables

$$\begin{aligned}\boldsymbol{\varepsilon}_e^{[m+1]} &= \boldsymbol{\varepsilon}_e^{\text{trial}} - \sqrt{3/2} \Delta\bar{\varepsilon}_p \frac{\text{dev}(\boldsymbol{\varepsilon}_e^{\text{trial}})}{||\boldsymbol{\varepsilon}_e^{\text{trial}}||} \\ \hat{p} &= -(\kappa/J^{[m+1]}) \text{ tr}(\boldsymbol{\varepsilon}_e^{[m+1]}) \\ \mathbf{s}^{[m+1]} &= \left[1 - (d_{[i]}^{[m+1]})^2 \right] (1/J^{[m+1]}) 2\mu \text{ dev}(\boldsymbol{\varepsilon}_e^{[m+1]}) \\ \bar{\varepsilon}_p^{[m+1]} &= \bar{\varepsilon}_p^{[m]} + \Delta\bar{\varepsilon}_p\end{aligned}$$

(v) if Solve pressure equation then

Implicitly solve the pressure Poisson's equation:

$$p^{[m+1]} - \mathbb{D}\nabla^2 p^{[m+1]} = \hat{p} - \nabla \cdot (\mathbb{D}\nabla p_{[i]}^{[m+1]})$$

else

$$p^{[m+1]} = \hat{p}$$

end

(vi) Update the true (Cauchy) stress

$$\boldsymbol{\sigma}^{[m+1]} = \mathbf{s}^{[m+1]} - p^{[m+1]}\mathbf{I}$$

(vi) Solve the phase field equation for d :

$$\frac{G_c}{2l} (d^{[m+1]} - 4l^2 \nabla^2 d^{[m+1]}) = \mathcal{H}_{[i]}^{[m+1]}$$

4 Benchmark Cases

This section assesses the performance of the developed finite volume procedures on two benchmark test cases: (i) a 2-D axisymmetric notched round bar and (ii) a 3-D flat notched bar. In both cases, a region of localised plastic strain develops at the centre of the specimen, but the levels of triaxiality experienced differ. The cases are presented simultaneously rather than sequentially to allow easier comparison of the material models.

Comparisons are made with predictions from previously developed procedures, finite element software Abaqus and results from the literature. In the Abaqus models, linear interpolation functions are used (Abaqus element code C3D8T for 3-D and CAX4RT for axisymmetry). For reference, single-cell verifications of the proposed material models are provided in Appendix A.

4.1 Geometries and Meshes

The notched round bar (Figure 3(a)) has been widely used for benchmarking plasticity and damage procedures [89–91]. The geometry consists of a 40 mm long round bar of diameter 18 mm with a 4 mm rounded notch. A 2-D axisymmetric model is created, including a horizontal symmetry plane, where a graded structured quadrilateral mesh is employed (Figure 3(b)).

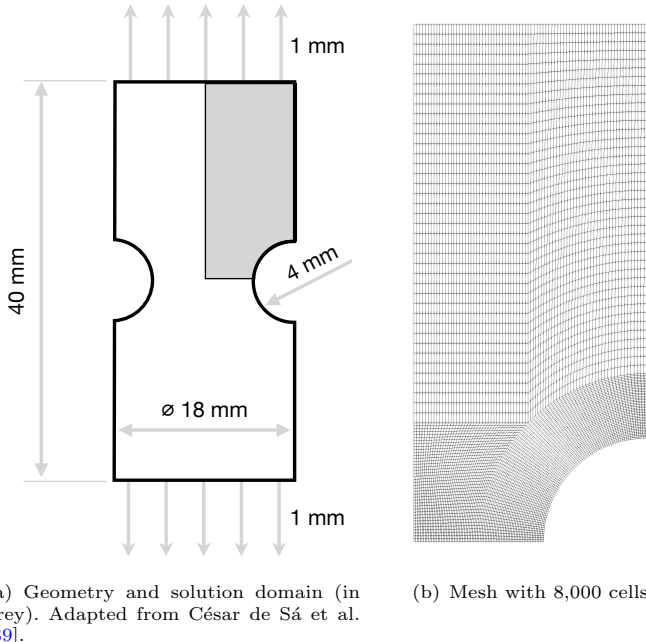


Fig. 3 Notched round bar geometry and mesh

The 3-D flat notched tensile specimen (Figure 4(a)) is another common test case for assessing damage models [24, 92]. The 3-D geometry comprises a $152.4 \times 25.4 \times 2.37$ mm plate with 4.06 mm diameter side notches. The solution domain comprises one-eighth of the specimen by exploiting three symmetry planes. A graded structured hexahedral mesh is employed with 10,000 hexahedral cells (Figure 4(b)).

The mesh spacing and time-step size have been chosen so that spatial and temporal discretisation are small for all cases.

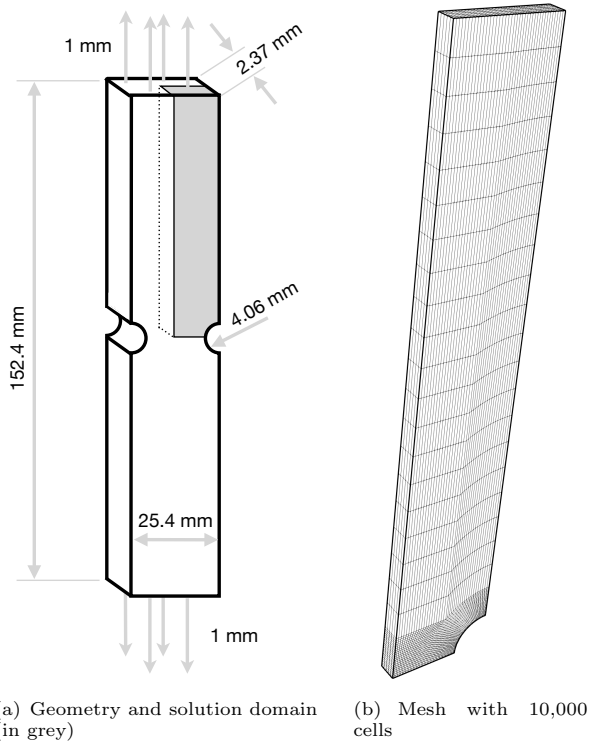


Fig. 4 Flat notched bar geometry and mesh

4.2 Loading Conditions

For both cases, an axial displacement of 1.0 mm is quasi-statically applied to the upper boundary over 1 s, resulting in a total elongation of 2 mm applied to the entire sample when accounting for the symmetry planes (Figures 3 and 4). The loading is applied over 1000 equal loading steps, resulting in a time step size of 1 ms. A global Rhie-Chow stabilisation factor of $\mathcal{R} = 0.01$ is used for all cases unless stated otherwise; the effect of this term is examined in Section 4.4.5. It was found that the pressure equation approach described in Section 2.3.2 was not required for the benchmark cases presented in this section, as pressure oscillations were not present.

For the Abaqus finite element cases, an adaptive time-stepping procedure was employed, with a maximum time increment size of 1 ms and a minimum of 0.001 ms.

4.3 Plasticity Model Verification

Before verifying the damage and fracture models, the implementation of the described plasticity model is verified by comparison with three other procedures:

- (a) The approach of Clancy [11] implemented in OpenFOAM that uses the logarithmic strain and the Mandel stress [59];

- (b) The approach of Cardiff et al. [13] implemented in OpenFOAM, which uses the Green strain tensor (left Cauchy–Green deformation tensor) and the return mapping algorithm described by Simo and Hughes [60];
- (c) The default approach in the finite element software Abaqus, which is based on the Jaumann stress rate.

Verification consists of examining the reaction forces at the loading boundary and the equivalent plastic strain $\bar{\varepsilon}_p$ at the centre of the notched round bar and the coordinate (7.02 0 0) mm for the flat notched bar, where the origin is the geometric centre and the first coordinate is in the direction of the notch. These locations have been chosen as the damage is greatest here in the later test cases.

4.3.1 Material Parameters

The elastoplastic material parameters for the notched round bar are given in Table 1, while the parameters for the flat notched bar are given in Table 2.

| Property | Symbol | Value | Units |
|-----------------|------------|--|-------|
| Young's modulus | E | 69 | GPa |
| Poisson's ratio | v | 0.3 | - |
| Hardening law | σ_y | $589(10^{-4} + \bar{\varepsilon}_p)^{0.216}$ | MPa |

Table 1 Material properties for the notched round bar case

| Property | Symbol | Value | Units |
|-----------------|------------|--------------------------------|-------|
| Young's modulus | E | 68.8 | GPa |
| Poisson's ratio | v | 0.33 | - |
| Hardening law | σ_y | $320 + 688\bar{\varepsilon}_p$ | MPa |

Table 2 Material properties for the flat notched bar case

4.3.2 Reaction Forces

The predicted reaction forces at the loading boundaries (Figures 5) align closely between all approaches, showing the forces and displacements for half the domain. It is worth noting that the reaction forces for both the Clancy [11] implementation and the implementation in this work (which both use the logarithmic strain) are slightly less than the Cardiff et al. [13] and Abaqus predictions in the latter stages of the deformation. These differences have been found to remain as the mesh spacing and time step are reduced, ruling out discretisation error as the cause. Although the reason for these subtle differences is unclear, the lack of mathematical equivalence between the logarithmic and Green/Jaumann strain approaches may be the cause. Similarly, the use of the Jaumann objective rate in Abaqus [93] may also contribute to the subtle differences, as it is known to exhibit unphysical stress oscillations at large shear deformations. Although it is outside the scope of the current study, implementing a similar Jaumann rate formulation in OpenFOAM is one approach for checking this hypothesis. For the purposes of benchmarking in the current work, these subtle differences are considered acceptable.

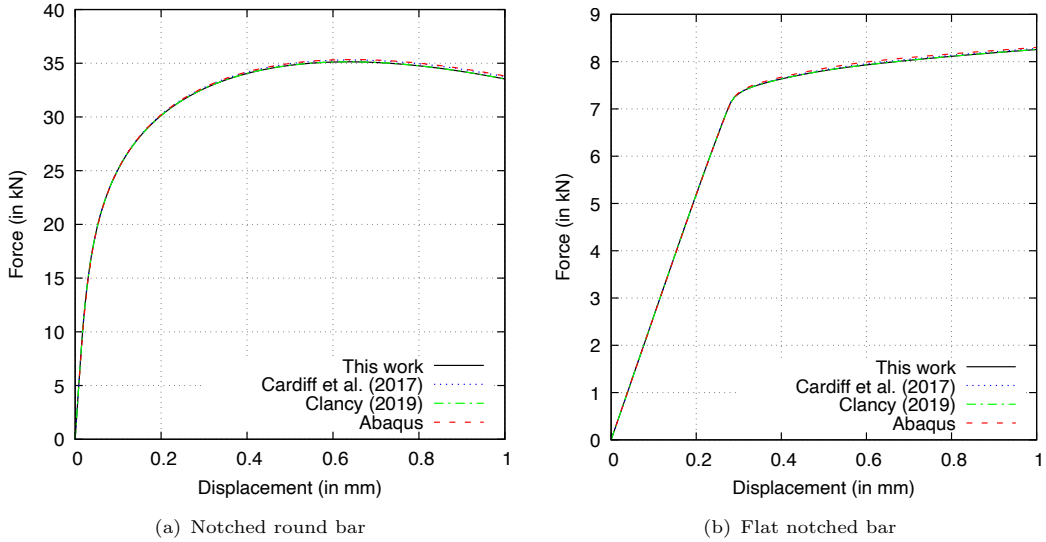


Fig. 5 Reaction forces at the upper loading boundary for the notched round bar and flat notched bar cases compared with predictions from the methods of Cardiff et al. [13], Clancy [11] and finite element software Abaqus

4.3.3 Plastic Strains

The equivalent plastic strain predictions at the points of interest agree for all approaches (Figure 6), with the values being marginally greater in the later stages for the finite volume (OpenFOAM) simulations compared with the Abaqus predictions. The equivalent plastic strain value is seen to increase smoothly in the notched round bar case (Figure 6(a)), whereas there is an initial elastic region followed by a steeper slope in the flat notched bar case (Figure 6(b)). Once again, the cause of the subtle differences in the latter stages is unclear but may be attributed to the mathematical differences between the logarithmic, Green and Jaumann strain approaches.

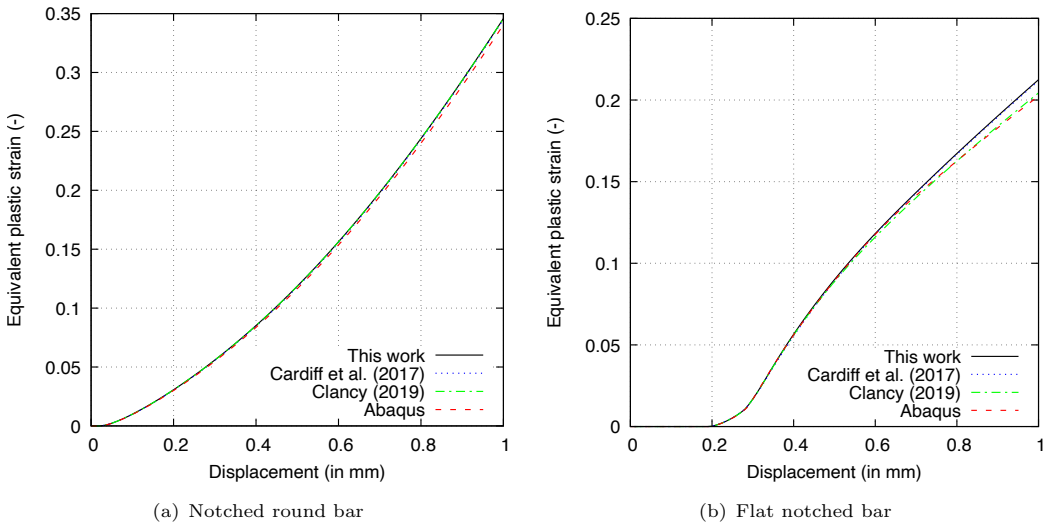


Fig. 6 Equivalent plastic strain at the specimen centres for the notched round bar and flat notched bar cases

4.4 Lemaitre Model

We now move on to verifying the damage procedures, starting with the Lemaitre model. Comparisons are given against results from the literature and those generated using Abaqus.

4.4.1 Material Parameters

The Lemaitre material parameters for the notched round bar case, taken from César de Sá et al. [89], are given in Table 3, while the Lemaitre material parameters for the flat notched bar case are given in Table 4.

| Property | Symbol | Value | Units |
|-----------------------|------------|--|-------|
| Young's modulus | E | 69.9 | GPa |
| Poisson's ratio | v | 0.3 | - |
| Damage denominator | S_0 | 1.1 | MPa |
| Damage exponent | b | 1.0 | - |
| Critical damage | D_c | 0.99 | - |
| Characteristic length | l_c | 0.6325 | mm |
| Hardening law | σ_y | $589(10^{-4} + \bar{\varepsilon}_p)^{0.216}$ | MPa |

Table 3 Lemaitre material parameters for the notched round bar case

| Property | Symbol | Value | Units |
|-----------------------|------------|---------------------------------|-------|
| Young's modulus | E | 68.9 | GPa |
| Poisson's ratio | v | 0.33 | - |
| Damage denominator | S_0 | 0.5 | MPa |
| Damage exponent | b | 1.0 | - |
| Critical damage | D_c | 0.99 | - |
| Characteristic length | l_c | 0.6325 | mm |
| Hardening law | σ_y | $320 + 688 \bar{\varepsilon}_p$ | MPa |

Table 4 Lemaitre material parameters for the flat notched bar case

4.4.2 Reaction Forces

Comparing the current (OpenFOAM) implementation and Abaqus reaction force predictions (Figure 7), the current work and Abaqus predictions can be seen to agree closely. The Abaqus simulations struggled to converge in the rapid crack propagation stage of the flat notched bar case, requiring very small time increments until it eventually crashed before reaching the end time. In contrast, convergence issues were not encountered with the current segregated, finite-volume OpenFOAM simulations. The reason for this difference in convergence behaviour is unclear, but it may stem from the different solution algorithms employed (Newton-Raphson vs. Picard). The Newton-Raphson approach used in Abaqus requires the calculation of the tangent stiffness matrix. For elastoplastic damage models, plastic deformation influences the onset and progression of damage and vice versa. This interaction can result in a significant coupling in the tangent stiffness matrix, manifesting as non-trivial off-diagonal terms [31], potentially leading to convergence difficulties.

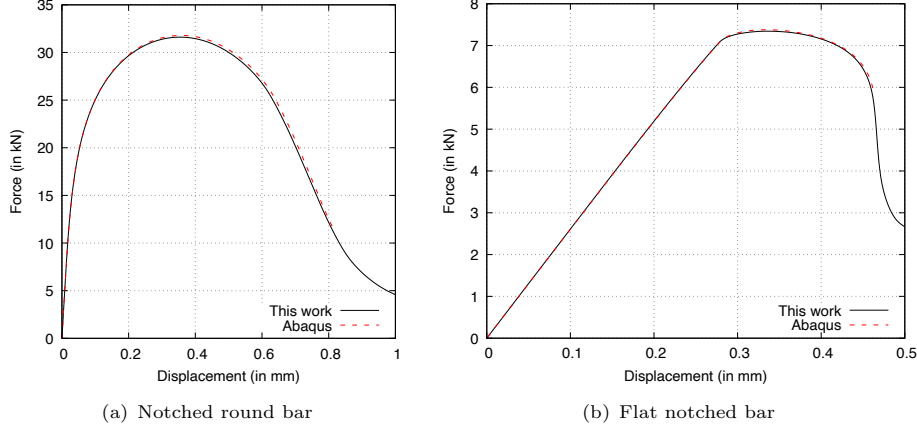


Fig. 7 Reaction force predictions using the Lemaitre damage model

4.4.3 Damage and Plastic Strains

Similar to the forces, the local values for damage and equivalent plastic strain can be seen to closely agree between the current work and Abaqus (Figures 8 and 9). Nonetheless, upon examining the figures closely, the damage and plastic strain in the current work increase slightly quicker than those in Abaqus. This effect can also be observed when viewing the reaction forces (Figure 7) in the previous section. The reason for this is unclear but could be related to the differences in plasticity model formulation, as noted above.

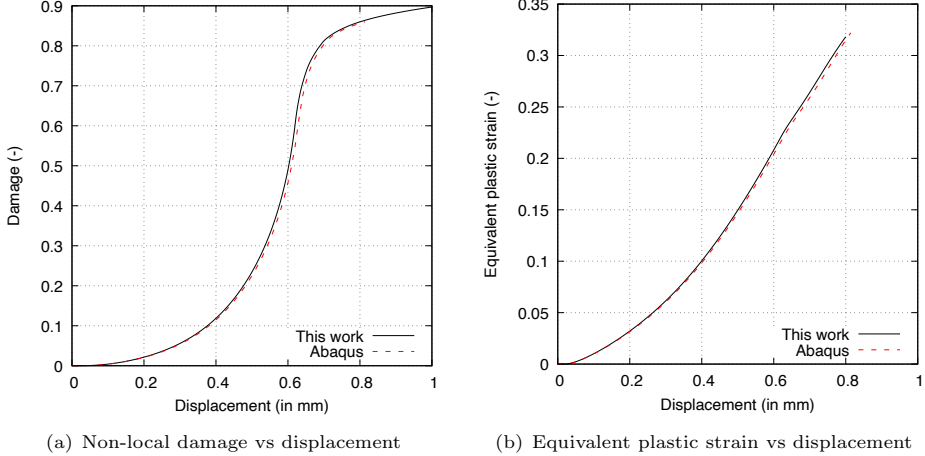


Fig. 8 Damage and plastic strain predictions for the notched round bar case using the Lemaitre model

For the notched round bar case, Figure 10 compares the predicted non-local damage distribution at a loading displacement of 1.2 mm with the predictions provided in César de Sá et al. [89], where the results are displayed on the initial mesh. Qualitative agreement can be observed between the distributions and values, allowing for the differences in the colour palettes.

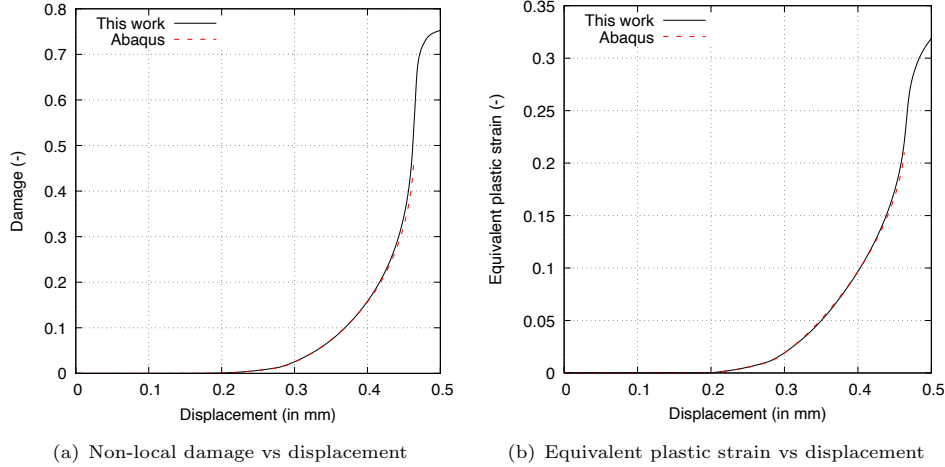


Fig. 9 Damage (non-local) and plastic strain predictions for the flat notched bar case using the Lemaitre model

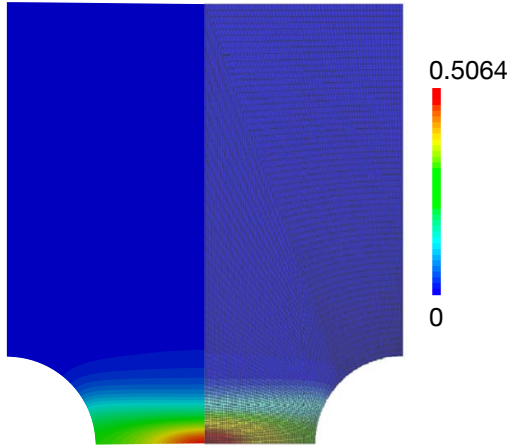


Fig. 10 Comparison of non-local damage distribution in the notched round bar case using the Lemaitre model at a total displacement of 1.2 mm. Predicted from the current work are on the left, while results from César de Sá et al. [89] are on the right. The results are displayed on the initial mesh.

4.4.4 Effect of the S_0 Parameter

The flat notched bar simulations are repeated here for different values of the material damage parameter S_0 . As the value of S_0 increases, rapid crack propagation occurs later in the deformation process. In Figure 11, the current work and Abaqus simulations are seen to be in agreement up to the point of early termination of the Abaqus models.

4.4.5 Effect of the Rhie Chow Stabilisation Term

This section explores the effect of the Rhie-Chow stabilisation term (Section 2.3.1) by examining its impact on the predicted force-displacement curves for the notched round bar and flat notched bar cases.

To get insight into its effect, the Rhie-Chow global scale factor \mathcal{R} is varied from 0.01 to 0.2 (Figure 12). As the Rhie-Chow global scale factor \mathcal{R} is decreased, a greater level of localisation

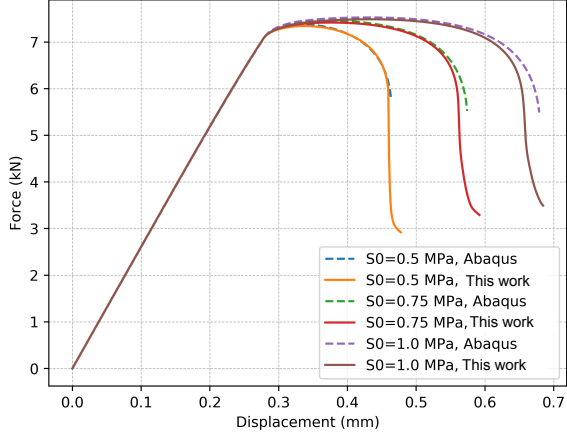


Fig. 11 Force vs. displacement for different values of the Lemaitre parameter S_0 on the flat notched bar case. The forces and displacements are shown for the half model.

is predicted to occur. In contrast, as the scale factor increases, a greater smoothing is seen in the force-displacement trace. As the purpose of the Rhie-Chow term is to smooth out oscillations in the solution field, it is perhaps unsurprising that it tends to quell physical localisations due to damage. The predictions for the notched round bar (Figure 12(a)) are seen to be less sensitive than in the flat notched bar case (Figure 12(b)). This difference can be explained by the increased damage localisation in the latter stages of the flat-notched bar case.

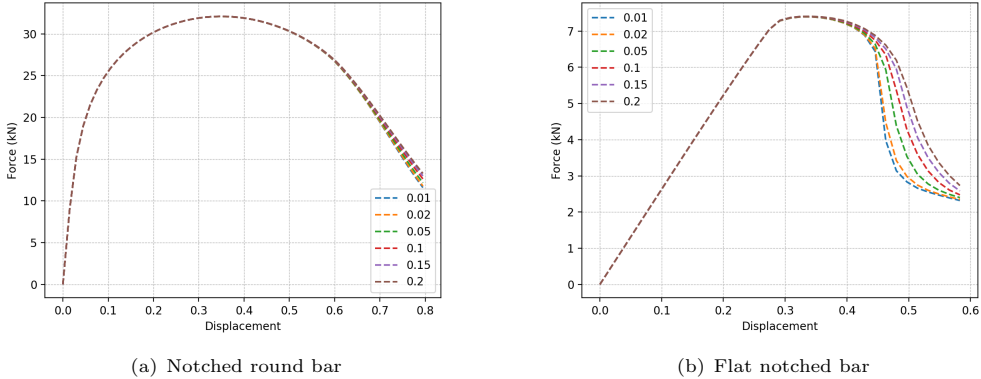


Fig. 12 Force vs. displacement predictions using the Lemaitre model where the Rhie-Chow global scale factor \mathcal{R} is varied from 0.01 to 0.2.

These results suggest that a small value of the Rhie-Chow scale factor \mathcal{R} should be used to avoid excessive smoothing in regions of localised damage. Nonetheless, as noted in Section 2.3.1, the Rhie-Chow term plays an important role in quelling numerical oscillations, particularly in the elastic regions where no dissipative mechanisms exist. In addition, smaller values of the Rhie-Chow term scale factor have been found to slow the convergence of the outer Picard iterations. Consequently, as described in Section 2.3.1, a damage-dependent Rhie-Chow scaling field is proposed here: $\mathcal{R}(1-D)^2$. In this case, a larger global scale factor $\mathcal{R} = 0.1$ can be used throughout the domain, which is then automatically reduced in regions where damage develops ($D > 1$). Many forms of scaling field could be chosen, where the form examined here has been chosen to quickly (greater than linear) reduce the Rhie-Chow stabilisation as the damage variable reduces from unity.

The predicted force-displacement curves using the proposed spatially-varying approach are shown in Figure 13, where the predictions obtained using uniform global Rhie-Chow scale factors of 0.1 and 0.01 are given for comparison. It can be observed that the proposed strategy reduces the effect of the Rhie-Chow scale factor on the localisation behaviour. Therefore, this scheme gains the benefits of a higher Rhie-Chow scale factor (improved convergence properties, reduction of numerical oscillations) up until crack propagation begins. At this point, the Rhie-Chow effects are reduced; therefore, its over-smoothing effect on fracture behaviour is mitigated.

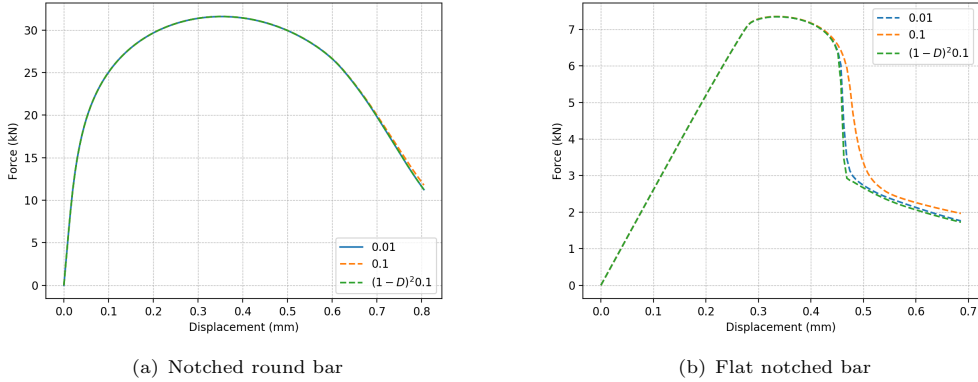


Fig. 13 The effect of the proposed spatially-varying Rhie-Chow scaling field on the predicted force-displacement curves, compared with uniform global scale factors of 0.01 and 0.1

The effect of the Rhie-Chow stabilisation term has been shown here for the Lemaitre damage model; however, the same behaviour is seen using the GTN and phase field models. Similarly, this effect can even be important in purely elastoplastic cases (no damage), particularly when localised plastic regions, e.g., shear bands, are present.

4.4.6 Effect of the Effective Non-Local Damage Approach

This section examines the effect of the proposed *effective* non-local damage approach introduced in Section 3.4.1. The classic non-local damage approach was adopted in the sections above. Here, the effective and classic non-local damage approaches are compared, where a more physically realistic critical damage parameter $D_c = 0.55$ is employed.

Figure 14 shows the predicted reaction forces for the notched round bar and flat notched bar cases, where the effective non-local damage approach is compared with the classic approach. A more physically realistic rapid crack propagation is evident in the force-displacement curve. Such a rapid loss of load-carrying capacity at a certain point for tensile specimens has been observed experimentally [62, 94]. Figure 15 shows a similar rapid increase in the damage evolution. It is worth noting that the maximum damage is set at 0.99, which, combined with the Rhie-Chow diffusive effects, still leads to some nonphysical residual force-displacement behaviour in the simulations. The benefit of the developed scheme can be further seen in Section 5.4, with the model correctly predicting the development of *chevron cracks* in the wire drawing process.

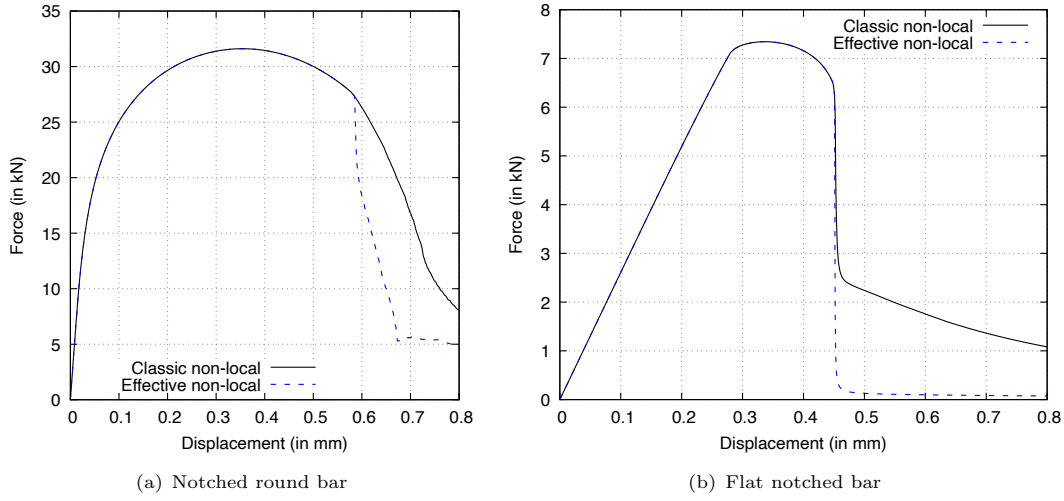


Fig. 14 Reaction force predictions using the Lemaitre damage model and the effective non-local damage approach

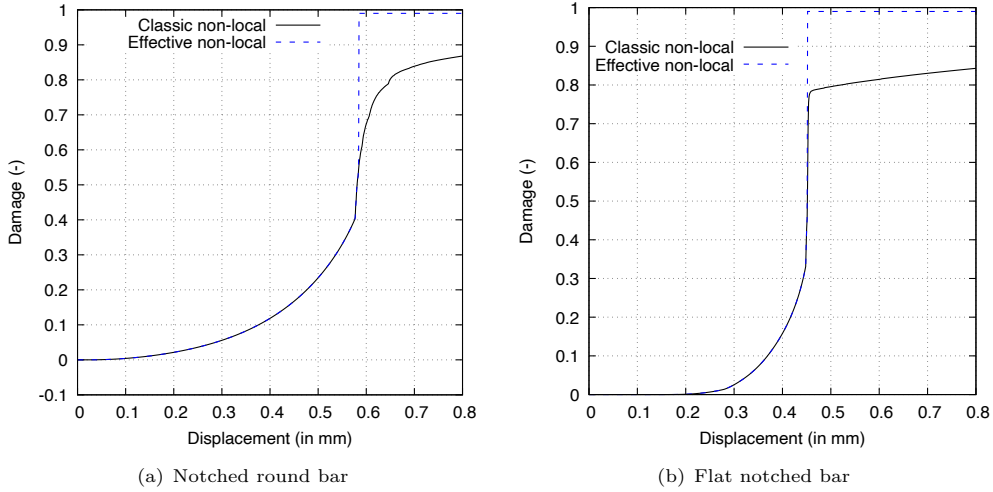


Fig. 15 Non-local damage predictions for the notched round bar and flat notched bar cases using the Lemaitre model and the effective non-local damage approach

4.5 GTN Model

4.5.1 Material Parameters

For the GTN model, the notched round bar is only examined here. The GTN material properties for the notched round bar case are given in Table 5.

4.5.2 Reaction Forces

The predicted force-displacement curves for the GTN model are compared with predictions from Abaqus in Figure 16. The forces align well, where, as with the Lemaitre model, a slightly quicker localisation can be observed in the OpenFOAM implementation. A feature of this test case when using the current GTN model and parameters is the sharp crack propagation, i.e. the sudden drop off in force in Figure 16. Consistent with the Lemaitre cases, the Abaqus simulation has

| Property | Symbol | Value | Units |
|--------------------------------------|-----------------|--|-------|
| Young's modulus | E | 69 | GPa |
| Poisson's ratio | v | 0.3 | - |
| q_1 | q_1 | 1.5 | - |
| q_2 | q_2 | 1 | - |
| q_3 | q_3 | 2.25 | - |
| Initial porosity | f_0 | 0.002 | - |
| Nucleation strain mean | ε_n | 0.15 | - |
| Nucleation strain standard deviation | S_n | 0.08 | - |
| Void volume fraction parameter | f_n | 0.2 | - |
| Hardening law | σ_y | $589(10^{-4} + \bar{\varepsilon}_p)^{0.216}$ | MPa |

Table 5 GTN material parameters for the notched round bar case

convergence issues and eventually crashes, while convergence issues were not encountered in the current (OpenFOAM) simulations.

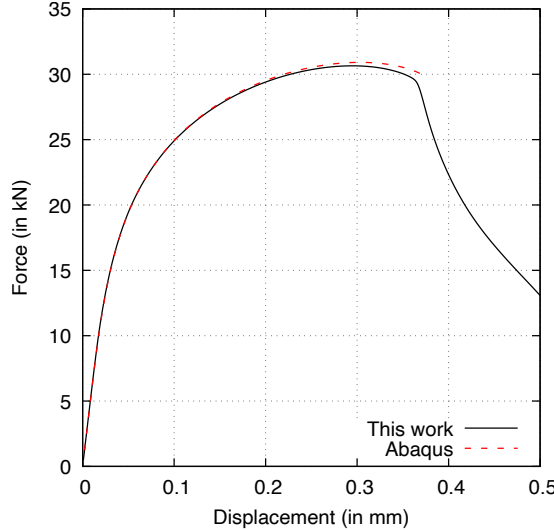


Fig. 16 Predicted force vs displacement for the notched round bar case using the GTN model, compared with predictions from Abaqus.

4.5.3 Porosity and Plastic Strains

The predicted porosity and equivalent plastic strain at the neck's centre are compared with Abaqus's predictions in Figure 17. Porosity and plastic strain increase smoothly up to the point at which the crack propagates, after which their values significantly increase. The differences between the current OpenFOAM formulation and the Abaqus formulation are more pronounced here, after the onset of necking. The GTN model in Abaqus is once again based on a Jaumann-rate plasticity formulation, which may be one reason for the observed differences.

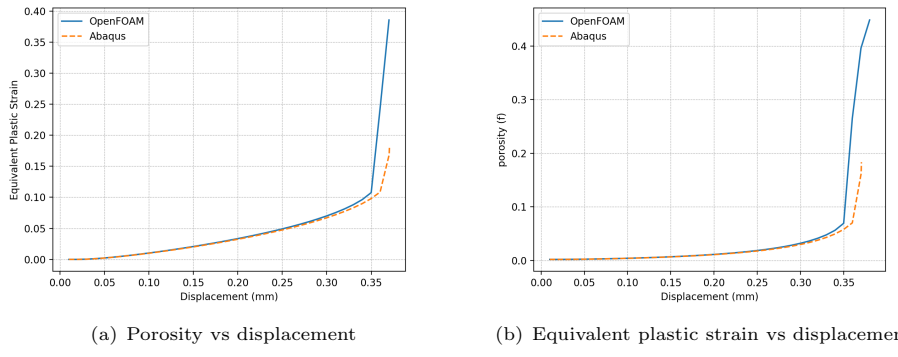


Fig. 17 Predicted porosity and equivalent plastic strain at the centre of the notched round bar case using the GTN model, compared with predictions from Abaqus.

4.6 Phase Field Model

4.6.1 Material Parameters

For the phase field model, the flat notched bar is only examined here, and the predictions are compared with the results from Borden et al. [24] and Eldahshan et al. [92]. The phase field model material properties are given in Table 6.

| Property | Symbol | Value | Units |
|--------------------------|------------|---------------------------------|------------------|
| Young's modulus | E | 68.8 | GPa |
| Poisson's ratio | v | 0.33 | - |
| Critical Fracture Energy | G_c | 60×10^3 | J/m ² |
| Plastic Threshold | W_o | 10 | MPa |
| Characteristic Length | l_c | 0.3226 | mm |
| Hardening law | σ_y | $320 + 688 \bar{\varepsilon}_p$ | MPa |

Table 6 Phase field material parameters for the notched flat notched bar case

4.6.2 Reaction Forces

For consistency with results in the literature, the results are presented here as normalised stress vs normalised displacement, resulting in a scaled version of the force vs displacement curve. The normalised stress is the reaction force divided by the initial area of the narrowest cross-section, and the normalised displacement is the total displacement divided by the specimen's initial length. The predicted normalised stress vs normalised displacement for the phase field model of the flat notched bar is shown in Figure 18. The normalised stress trace plateaus after the initial elastic region, followed by a rapid drop corresponding to crack propagation. The results agree closely with those from Borden et al. [24] and Eldahshan et al. [92]. It is worth noting that the normalised stress reported by Borden et al. [24] before the rapid crack propagation is slightly lower than that obtained here and by Eldahshan et al. [92].

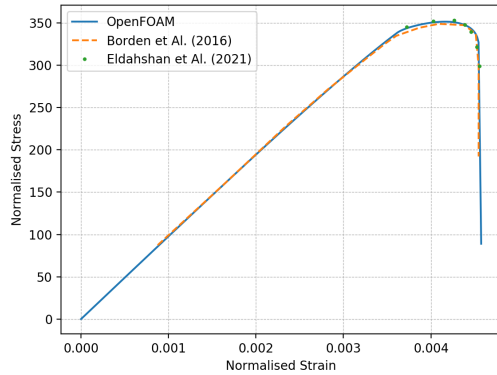
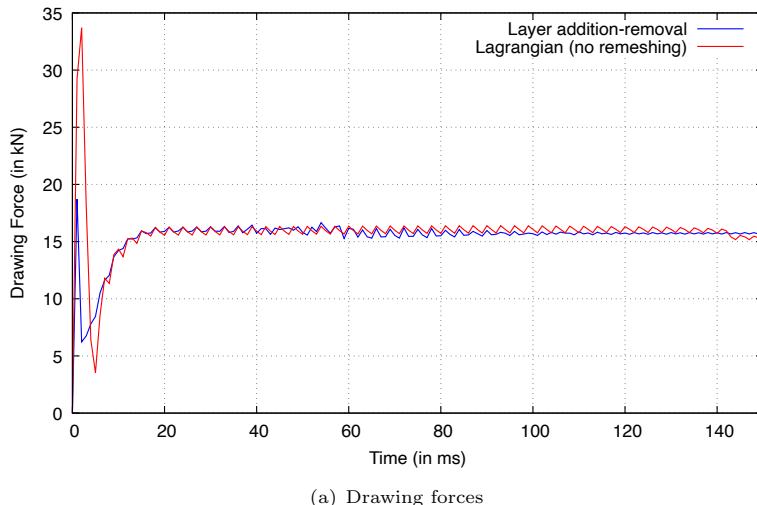


Fig. 18 Predicted normalised stress vs normalised displacement for the flat notched bar case using the phase field model, compared with predictions from Borden et al. [24] and Eldahshan et al. [92].

4.7 Benchmarking the Layer Addition-Removal Remeshing Procedure

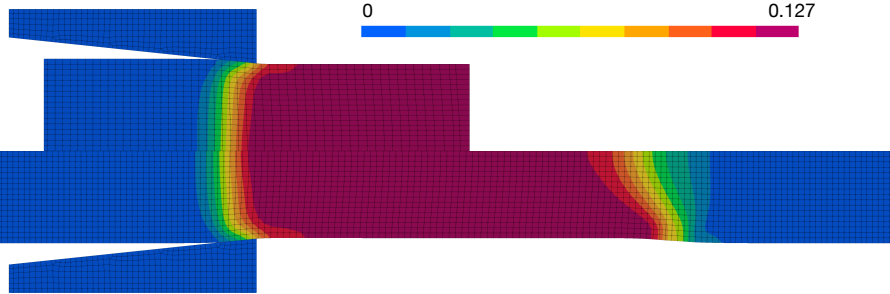
As a final benchmark, the proposed layer addition-removal remeshing procedure is compared with the traditional Lagrangian approach (no remeshing) for a wire drawing case where no damage accumulation is assumed. Here, the wire drawing setup is the same as described in Section 5.3, except no damage model is employed. In the layer addition-removal case, the wire length is kept constant at $L_w = 30$ mm, while in the traditional Lagrangian approach $L_w = 60$ mm. In both cases, a drawing displacement of 45 mm is applied over 150 ms.

Figure 4.7 compares the predicted drawing force (force in the axial direction on the wire downstream boundary) as a function of time for the layer addition-removal and traditional (no remeshing) approaches. After the startup phase (< 20 ms), the drawing forces are seen to closely agree for both approaches. The oscillations in force come from the mesh resolution effects on the contact procedure and are seen to reduce as the mesh is refined. After 100 ms, the oscillations are seen to reduce in the layer addition-removal approach, which is attributed to the wire axial cell widths approximately matching the axial distance travelled each time step. Near the end time (> 140 ms), the predicted forces from the Lagrangian (no remeshing) approach are seen to drop, due to the boundary effects from the approaching wire upstream boundary.

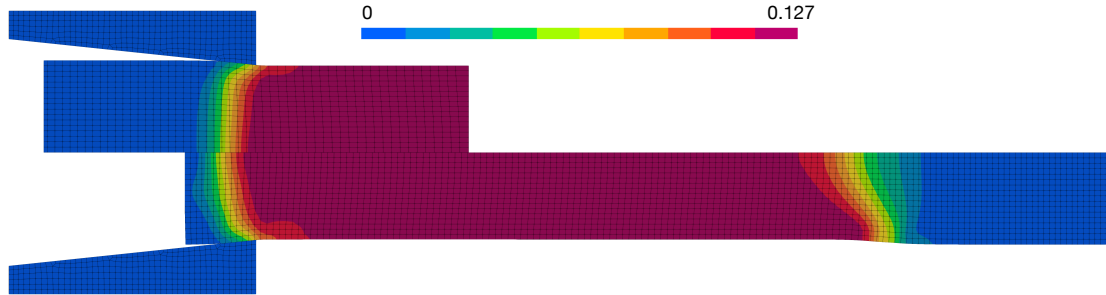


(a) Drawing forces

Figures 19(a) and (b) compares the predicted epsilon plastic strain distribution at the $t = 100$ ms and $t = 150$ ms respectively for both approaches, where the layer addition-removal results are shown on the top and the Lagrangian (no remeshing) results are reflected on the bottom. The plastic strain fields are seen to be qualitatively similar in both approaches at $t = 100$ ms. At $t = 150$ ms, minor changes can be seen in the Lagrangian (no remeshing) approach due to the proximity of the wire upstream boundary.



(b) Equivalent plastic strain distribution at 100 ms for the layer addition-removal (upper) and Lagrangian (lower) approaches



(c) Equivalent plastic strain distribution at 150 ms for the layer addition-removal (upper) and Lagrangian (lower) approaches

Fig. 19 Comparison of the predictions from the layer addition-removal remeshing procedure and the traditional Lagrangian (no remeshing) procedure

The clock time for the layer addition-removal approach is 279 s, while it was 783 s for the Lagrangian (no remeshing) approach, highlighting that doubling number of wire cells more than doubled the clock time ($\times 2.8$ in this case).

This benchmark case demonstrates that the proposed layer addition-removal approach achieves its goal of reducing the computational time, while still delivering the same predictions.

5 Wire Drawing Simulations

5.1 The Wire Drawing Process

This section applies the developed damage procedures to the wire drawing process (Figure 20). The key parameters are the die semi-angle α (in $^\circ$), which is the angle made by the die with the

wire axis, and the reduction ratio r (%), given by

$$r = 100 \times \left(\frac{d_i^2 - d_o^2}{d_i^2} \right) \quad (86)$$

where d_i is the wire's initial diameter, and d_o is the die outlet diameter. The final wire diameter tends to be marginally larger than the die outlet diameter due to elastic *spring back*.

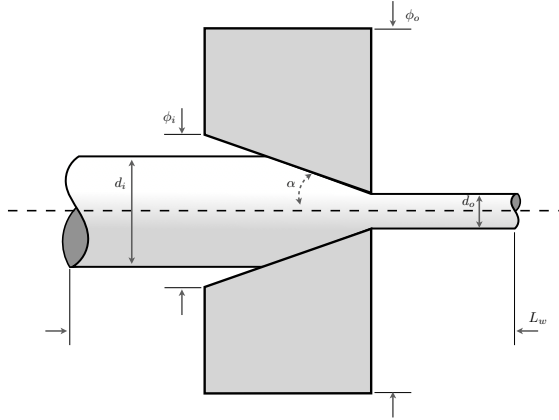


Fig. 20 Schematic of the axisymmetric wire drawing process with a conical die. See Table 10 for the definition of the symbols.

5.2 Comparison of Damage Models for Wire Drawing

In wire drawing, fracture typically originates in the centre of the specimen due to the combination of triaxiality and plastic strain [95–98]. To compare the ability of the damage models to predict this type of damage, a *typical* wire drawing pass is considered, with a reduction ratio r of 10% and a semi-angle α of 6° [66]. This case is not expected to display *catastrophic* fracture; however, damage accumulation is envisaged. The simulations are performed as 2-D axisymmetric with a structured quadrilateral mesh. An average cell width of 0.4 mm is employed, which has been found to minimise mesh errors. Table 10 summarises the geometry and mesh parameters.

| Quantity | Symbol | Value | Units |
|-----------------------|----------|-------|-------|
| Die inlet diameter | ϕ_i | 16 | mm |
| Die outer diameter | ϕ_o | 20 | mm |
| Die outlet diameter | d_o | 12.33 | mm |
| Die semi-angle | α | 6 | ° |
| Wire length | L_w | 30 | mm |
| Wire initial diameter | d_i | 13 | mm |

Table 7 Die and wire geometry for comparing damage modelling approaches. Refer to Figure 20 for interpretation of the parameters.

The wire elastoplastic material parameters, typical of a high-carbon steel, are given in Table 11 [11]. A modified Voce Law [99] (Equation 88) is chosen to describe the plastic hardening law, as Cao [99] found that this law accurately described the hardening behaviour of high carbon steel

in tensile, torsion and compression tests.

$$\sigma_y = \sigma_0 + (\sigma_\infty - \sigma_0 + k\bar{\varepsilon}_p)(1 - e^{-\beta\bar{\varepsilon}_p}) \quad (87)$$

The die elastic parameters (Table 12) correspond to tungsten carbide, as is typically used for

| Term | Value | Units |
|-----------------|-------|-------|
| Young's modulus | 200 | GPa |
| Poisson's ratio | 0.3 | - |
| σ_0 | 689 | MPa |
| σ_∞ | 1340 | MPa |
| k | 250 | MPa |
| β | 32.82 | - |

Table 8 Wire elastoplastic material parameters, where the hardening behaviour is given by Equation 88

drawing die nibs.

| Term | Value | Units |
|-----------------|-------|-------|
| Young's modulus | 600 | GPa |
| Poisson's ratio | 0.22 | - |

Table 9 Die elastic material parameters

A back tension of 20 MPa is applied to the wire upstream boundary, while a total drawing displacement of 45 mm is applied to the downstream wire boundary over 150 ms, allowing quasi-steady-state conditions to be reached. Frictional contact (Coulomb coefficient of 0.1) is assumed between the wire and die contact surfaces. All other die surfaces are assumed to have a zero displacement condition, mimicking the steel casings typically used. The pressure equation approach described in Section 2.3.2 is used for all wire drawing cases presented here, where the Rhee-Chow pressure scale factor was set as $R_p = 100$. The Eulerian-type mesh layer addition and removal procedure (Section 2.5) is employed at the wire upstream and downstream boundaries. In the modelling approach adopted here, the entire length of the wire starts at the initial diameter, resulting in an overlap with the die. In the first time step, the contact procedure ‘pushes’ the wire back, enforcing the contact constraints. This procedure has been found to reach quasi-steady-state drawing conditions efficiently; however, it can lead to convergence issues when incorporating damage, particularly in cases with large reduction ratios and high die angles. This issue is ameliorated here by allowing the damage to evolve only after a user-specified drawing displacement, chosen here as 2 mm.

5.3 Comparison of Damage Models for Wire Drawing

In wire drawing, fracture typically originates in the centre of the specimen due to the combination of triaxiality and plastic strain [95–98]. To compare the ability of the damage models to predict this type of damage, a *typical* wire drawing pass is considered, with a reduction ratio r of 10% and a semi-angle α of 6° [66]. This case is not expected to display *catastrophic* fracture; however, damage accumulation is envisaged. The simulations are performed as 2-D axisymmetric with a

structured quadrilateral mesh. An average cell width of 0.4 mm is employed, which has been found to minimise mesh errors. Table 10 summarises the geometry and mesh parameters.

| Quantity | Symbol | Value | Units |
|-----------------------|----------|-------|-------|
| Die inlet diameter | ϕ_i | 16 | mm |
| Die outer diameter | ϕ_o | 20 | mm |
| Die outlet diameter | d_o | 12.33 | mm |
| Die semi-angle | α | 6 | ° |
| Wire length | L_w | 30 | mm |
| Wire initial diameter | d_i | 13 | mm |

Table 10 Die and wire geometry for comparing damage modelling approaches. Refer to Figure 20 for interpretation of the parameters.

The wire elastoplastic material parameters, typical of a high-carbon steel, are given in Table 11 [11]. A modified Voce Law [99] (Equation 88) is chosen to describe the plastic hardening law, as Cao [99] found that this law accurately described the hardening behaviour of high carbon steel in tensile, torsion and compression tests.

$$\sigma_y = \sigma_0 + (\sigma_\infty - \sigma_0 + k\bar{\varepsilon}_p)(1 - e^{-\beta\bar{\varepsilon}_p}) \quad (88)$$

The die elastic parameters (Table 12) correspond to tungsten carbide, as is typically used for

| Term | Value | Units |
|-----------------|-------|-------|
| Young's modulus | 200 | GPa |
| Poisson's ratio | 0.3 | - |
| σ_0 | 689 | MPa |
| σ_∞ | 1340 | MPa |
| k | 250 | MPa |
| β | 32.82 | - |

Table 11 Wire elastoplastic material parameters, where the hardening behaviour is given by Equation 88

drawing die nibs.

| Term | Value | Units |
|-----------------|-------|-------|
| Young's modulus | 600 | GPa |
| Poisson's ratio | 0.22 | - |

Table 12 Die elastic material parameters

A back tension of 20 MPa is applied to the wire upstream boundary, while a total drawing displacement of 30 mm is applied to the downstream wire boundary over 150 ms, allowing quasi-steady-state conditions to be reached. Frictional contact (Coulomb coefficient of 0.1) is assumed between the wire and die contact surfaces. All other die surfaces are assumed to have a zero displacement condition, mimicking the steel casings typically used. The pressure equation approach described in Section 2.3.2 is used for all wire drawing cases presented here, where the Rhie-Chow pressure scale factor was set as $\mathcal{R}_p = 100$. The Eulerian-type mesh layer addition and removal procedure (Section 2.5) is employed at the wire upstream and downstream boundaries. In the modelling approach adopted here, the entire length of the wire starts at the initial diameter, resulting

in an overlap with the die. In the first time step, the contact procedure ‘pushes’ the wire back, enforcing the contact constraints. This procedure has been found to reach quasi-steady-state drawing conditions efficiently; however, it can lead to convergence issues when incorporating damage, particularly in cases with large reduction ratios and high die angles. This issue is ameliorated here by allowing the damage to evolve only after a user-specified drawing displacement, chosen here as 2 mm.

5.3.1 Lemaitre Model

Table 13 gives the Lemaitre model wire parameters. Simulations are conducted here, both with and without crack-closure effects. For the Lemaitre model *with* crack-closure effects, the crack-closure parameter is taken to be 0.2 [61, 72, 73].

| Property | Symbol | Value | Units |
|-----------------------------|--------|-------|-------|
| Lemaitre damage denominator | S_0 | 13.5 | MPa |
| Lemaitre damage exponent | b | 1.0 | - |
| Lemaitre critical damage | D_c | 0.99 | - |
| Crack closure parameter | h | 0.2 | - |

Table 13 Lemaitre model parameters for wire drawing

Figure 21 provides the predicted Lemaitre damage distributions. It can be observed that without crack-closure effects (upper image in Figure 21), the Lemaitre model gives a somewhat unrealistic damage distribution, with damage being at a maximum away from the centre of the wire. This is because it does not distinguish between positive and negative triaxialities. In contrast, the damage is correctly predicted at a maximum in the centre of the wire for the Lemaitre model *with* crack-closure effects (lower image in Figure 21). This is where the triaxiality and, relatedly, the positive stress tensor are at a maximum. Both models predict limited damage evolution towards the outer surface of the wire due to the triaxiality cut-off ($-1/3$) for damage evolution.

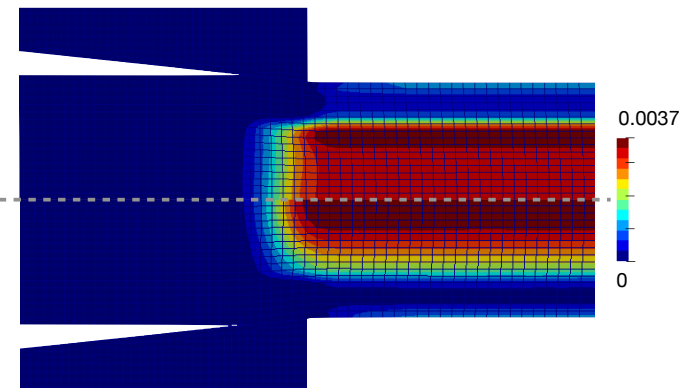


Fig. 21 Predicted damage distribution from the the Lemaitre damage model with (lower) and without (upper) crack-closure effects

5.3.2 GTN Model

The GTN model wire parameters are given in Table 14, corresponding to those of a typical high-strength steel.

| Property | Symbol | Value | Units |
|--------------------|-----------------|-------|-------|
| q_1 | q_1 | 1.5 | - |
| q_2 | q_2 | 1 | - |
| q_3 | q_3 | 2.25 | - |
| Initial porosity | f_0 | 0.002 | - |
| Mean | ε_n | 0.03 | - |
| Standard deviation | S_n | 0.02 | - |
| Volume fraction | f_N | 0.04 | - |

Table 14 GTN model parameters for wire drawing

For the GTN model, porosity growth is negligible for typical wire drawing passes due to the high hydrostatic pressures, making void nucleation the dominant mechanism driving the evolution of the porosity [99]. The GTN model accurately predicts the porosity to be maximum at the centre of the wire (Figure 22). This is because porosity evolution due to nucleation is only set to occur when the hydrostatic pressure is negative (Equation 67). However, there are apparent issues with the assumption of the Gaussian distribution for void nucleation. To illustrate this, the evolution of the equivalent plastic strain and porosity are shown in Figure 23 for a cell near the axis of the wire. It can be observed that the Gaussian assumption leads to the porosity saturating. This is unlikely to reflect the true material behaviour [99], suggesting an alternative assumption may be more appropriate.

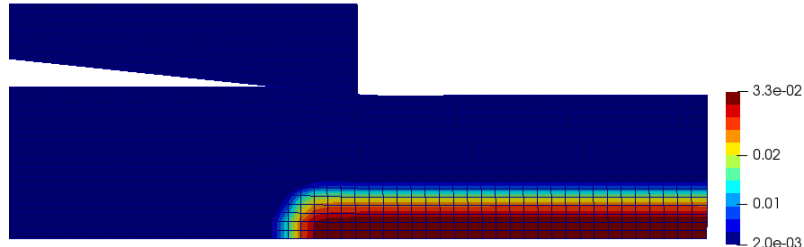


Fig. 22 Predicted porosity distribution in wire drawing for the GTN model

5.3.3 Phase Field Model

The phase field model wire parameters are given in Table 15, also chosen to correspond to those of a typical high-strength steel.

| Property | Symbol | Value | Units |
|--------------------------|--------|--------|-------------------|
| Critical fracture energy | G_c | 1 | MJ/m ² |
| Plastic work threshold | W_o | 0 | J |
| Characteristic length | l | 0.3266 | mm |

Table 15 Phase field fracture model parameters for wire drawing

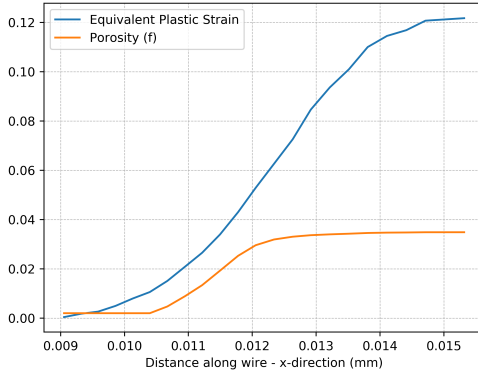


Fig. 23 Predicted porosity and equivalent plastic strain evolution along the wire axis in the axial (x) direction for the GTN model.

The phase field fracture model predicts material degradation to be at its greatest towards the outer surface of the wire (Figure 24). The region with the greatest plastic straining corresponds to the region where material degradation is predicted to be highest. This is contrary to what is expected. The current phase field model does not distinguish between tensile and compressive stress states for the plastic contribution towards crack growth, leading to this unrealistic behaviour.

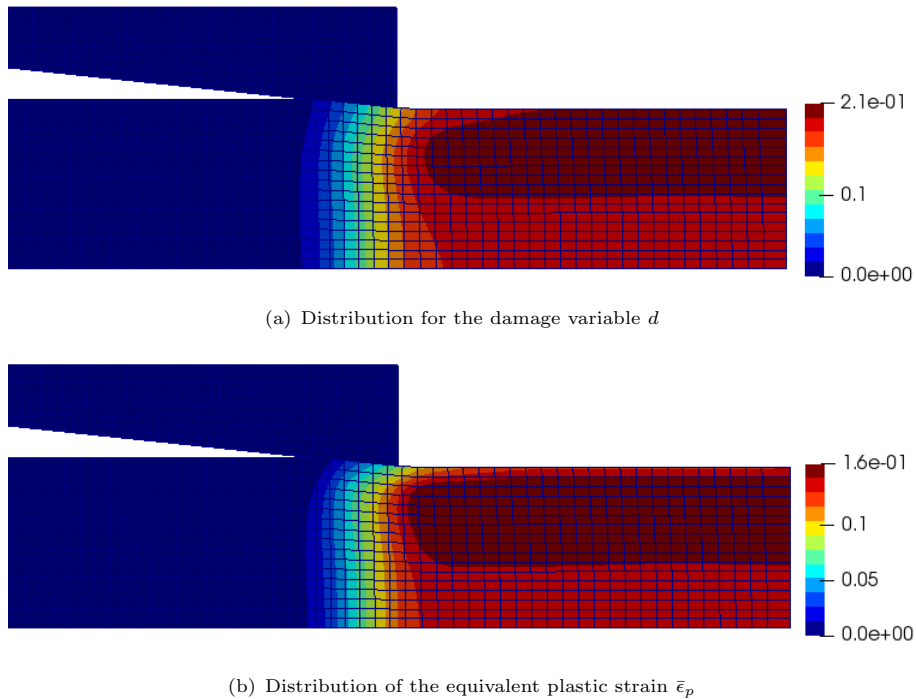


Fig. 24 Predicted damage and equivalent plastic strain fields in wire drawing for the phase field model.

5.3.4 Summary

Along with the limitations in the GTN and phase field models described in the previous section, other factors make them unsuitable for further investigation in predicting fracture in wire drawing

processes. The phase field fracture model requires a relatively fine mesh [24], making it computationally expensive. The GTN model requires the calibration of multiple parameters, which is not feasible given the data available for the cases that will be looked at here. To rigorously calibrate these parameters, the characterisation of each stage of ductile damage requires the continuous monitoring of void nucleation, growth and coalescence during deformation. This is possible (for example, using X-ray tomography measurements such as in Thuillier et al. [100] and Fansi et al. [101]), but is far more demanding than required of the Lemaitre-type models. Consequently, Lemaitre-based damage models with crack-closure effects are chosen here for further evaluation.

5.4 Prediction of Chevron Cracks

To test the Lemaitre models further, their ability to predict *chevron cracks* is examined in this section. Chevron cracks, also known as central burst defects, are common defects that occur at the wire centre in drawing (Figure 25).

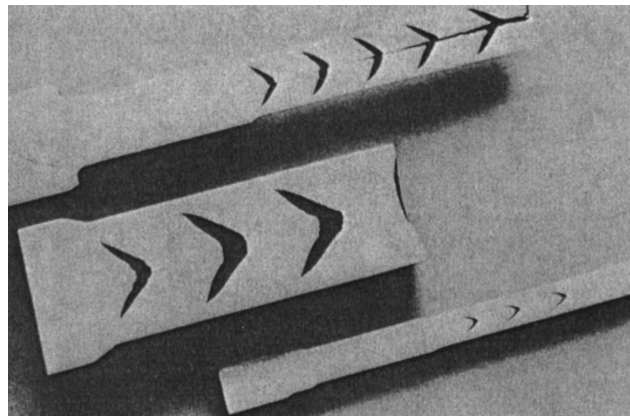


Fig. 25 Chevron cracks in steel rods, similar to those that can occur in drawn wires [102]

A reduction of $r = 20\%$ and a die semi-angle of $\alpha = 10^\circ$ are chosen, where all geometric parameters are given in Table 16.

| | | | |
|-----------------------|----------|--------|----------|
| Die inlet diameter | ϕ_i | 16 | mm |
| Die outer diameter | ϕ_o | 20 | mm |
| Die outlet diameter | d_o | 11.627 | mm |
| Die semi-angle | α | 10 | $^\circ$ |
| Wire length | L_w | 30 | mm |
| Wire initial diameter | d_i | 13 | mm |

Table 16 Die and wire geometry used for the chevron crack predictions.

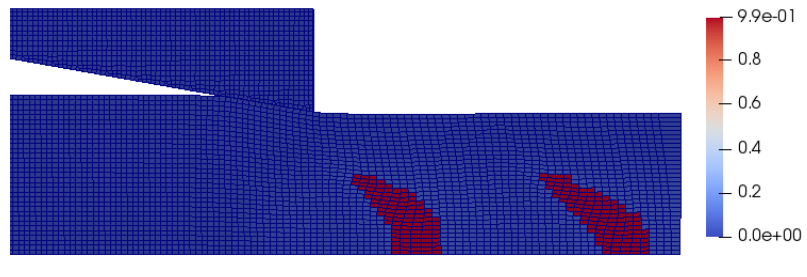
Table 17 gives the assumed wire elastoplastic Lemaitre properties. These properties, along with the drawing reduction and angle, have been chosen to be in a drawing regime expected to produce chevron cracks. Table 12 gives the die elastic properties.

The effective non-local damage field (Figure 26) predicts the formation of expected chevron cracks. The characteristic semi-lunar-shaped cracks are found to occur at a fixed frequency and

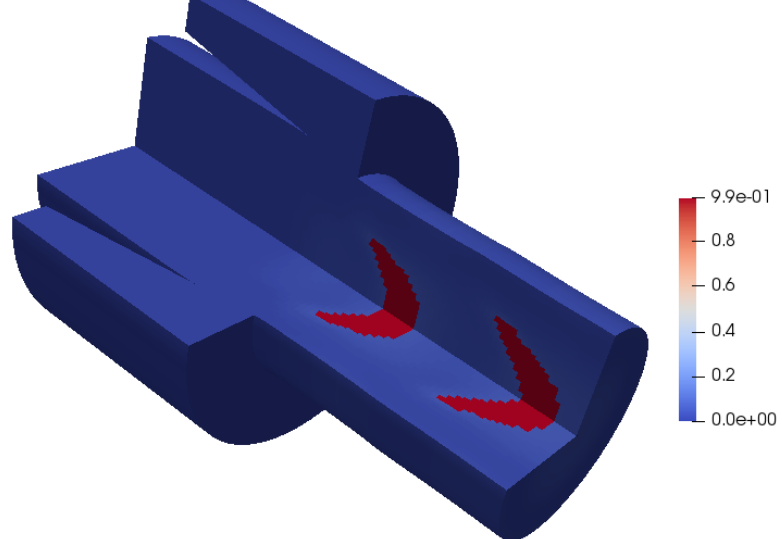
| Property | Symbol | Value | Units |
|-----------------------------|-----------------|-------|-------|
| Young's modulus | E | 200 | GPa |
| Poisson's ratio | ν | 0.33 | - |
| Lemaitre damage denominator | S_0 | 15 | MPa |
| Lemaitre damage exponent | b | 1.0 | - |
| Critical damage | D_c | 0.052 | - |
| Characteristic length | l_c | 0.325 | mm |
| Initial yield stress | σ_0 | 600 | MPa |
| Asymptotic yield stress | σ_∞ | 1280 | MPa |
| Hardening parameter | k | 250 | MPa |
| Hardening parameter | β | 43.44 | - |

Table 17 Wire material parameters for the chevron crack simulation. The hardening behaviour is given by Equation 88.

continue to form as long as the drawing continues. From the modelling perspective, it has been found that without the proposed effective non-local damage approach described in Section 3.4.1, the non-local damage field grows excessively, resulting in the over-prediction of damage. Consequently, rapid crack propagation ensues, and the formation of chevron cracks is not predicted. Hence, including such an effective damage-limiting procedure is crucial in predicting these types of defects.



(a) Axisymmetric mesh



(b) Rotational extrusion (270°) of the axisymmetric mesh

Fig. 26 Prediction of chevron cracks in wire drawing using the Lemaitre damage model. The distribution of the damage variable d is shown.

5.5 Fracture Prediction in a Drawing Series

5.5.1 Drawing Series Overview

In this final section, the experimental wire drawing series from Roh et al. [66] is used to investigate the ability of the Lemaitre-based damage models to predict fracture. Data is available for die half-angles α from 2 to 16° , and reduction ratios r from 20 to 36%. The initial wire diameter was 13 mm. Table 18 summarises the experimental drawing test data available for the examined high-carbon steel wire, where tests which displayed catastrophic wire fracture are indicated with the symbol X .

| | Reduction r (%) | Drawing Die Half-Angle α ($^\circ$) | Fracture |
|----|-------------------|--|----------|
| 20 | 2 | | - |
| | 4 | | - |
| | 6 | | - |
| | 8 | | - |
| | 10 | | - |
| | 12 | | X |
| | 14 | | X |
| | 16 | | X |
| 36 | 4 | | - |
| | 6 | | - |
| | 8 | | - |
| | 10 | | - |
| | 12 | | X |
| | 14 | | X |
| | 16 | | X |

Table 18 Experimental high-carbon steel wire drawing series data from Roh et al. [66], where tests which displayed catastrophic wire fracture are indicated with the symbol X

A 30 mm long wire was used for drawing simulations, aside from the cases where $r = 36\%$, $\alpha = 4^\circ$ and $r = 20\%$, $\alpha = 2^\circ$. In these cases, a longer 50 mm wire was used to ensure minimum upstream and downstream boundary effects. Table 19 summarises the die and wire geometry. An average cell width of 0.25 mm was found to be sufficient to minimise mesh errors. The coefficient of friction was taken as $\mu = 0.08$, as determined in Roh et al. [66]. Neither the die's specific geometry nor the die's material properties are specified in Roh et al. [66], so a conical die is assumed here with die material parameters taken from Clancy [11], corresponding to tungsten carbide. A total drawing displacement of 30 mm is applied to the wire downstream boundary in increments of 0.1 mm with a time step size of 0.5 ms (the total simulation time was 150 ms). A back tension of 20 MPa was applied to the wire upstream boundary. As before, the damage can only evolve after a drawing displacement of 2 mm to avoid localisation in the initial time steps.

| | | | |
|-----------------------|----------|------------------------------|----------|
| Die inlet diameter | ϕ_i | 16 | mm |
| Die outer diameter | ϕ_o | 20 | mm |
| Die outlet diameter | d_o | [11.627, 10.4] | mm |
| Die semi-angle | α | [2, 4, 6, 8, 10, 12, 14, 16] | $^\circ$ |
| Wire length | L_w | [30, 50] | mm |
| Wire initial diameter | d_i | 13 | mm |

Table 19 Die and wire geometry used for the drawing series analyses.

In the models presented here, the non-local gradient equation is not incorporated as localisation behaviour is limited due to the low calibrated value of D_c , and hence, it would not significantly change the results.

5.5.2 Material Model Calibration

To calibrate the elastoplastic and Lemaitre parameters, tensile test data provided in Roh et al. [66] is used (Figure 27). The calibration procedure follows that of Masse [8], where the plastic hardening law is first calibrated against the experimental force-displacement data up to the point where necking is observed ($\approx 6.5\%$ engineering strain). Subsequently, the damage parameters are calibrated while the elastoplastic parameters are fixed. The calibration procedure is simplified by separating out the calibration of the plastic hardening law and the damage parameters, and the risk of over-fitting is reduced. The Young's modulus (200 GPa), Poisson's ratio (0.3) and initial yield stress (689 MPa) are taken directly from Roh et al. [66].

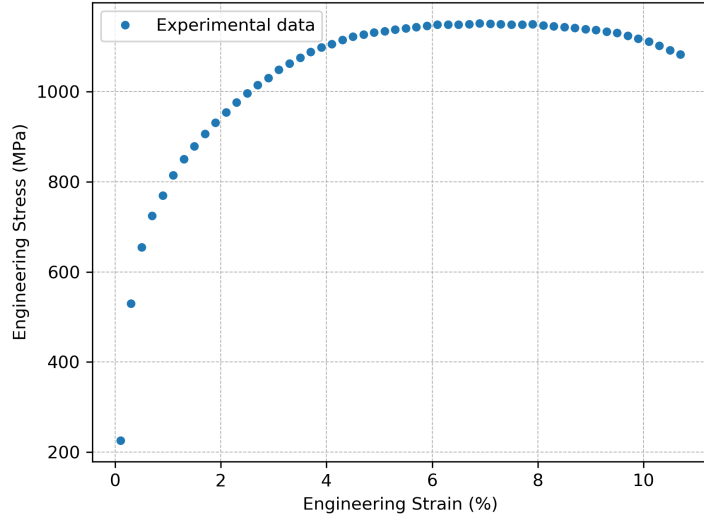


Fig. 27 Tensile test experimental data from Roh et al. [66]

A combined global-local approach is taken to calibrate the elastoplastic and damage parameters. Initially, 50 sets of values for σ_∞ , k and β (Equation 88) are taken from the range of values given in Table 20 using Latin hypercube sampling [103]. Each of these sets of values is used to simulate a tensile test. The force-displacement curves from each simulation are then compared to the experimental data up to 6.5% engineering strain (onset of necking). The parameter sets with the minimum difference from this *global* sampling are then further optimised using the *local* Nelder-Mead method [104] to refine the material parameters. Table 20 gives the final optimised values. Here, two forms of the Lemaitre model are compared: (i) the classic form, where the S parameter is a constant, and (ii) the form proposed in Equation 50, which introduces a triaxiality dependence to the S parameter.

| Term | Range | | Optimal Value | Units |
|-----------------|-------|-------|---------------|-------|
| | Lower | Upper | | |
| σ_∞ | 1.1 | 1.5 | 1.34 | GPa |
| k | 50 | 500 | 104 | MPa |
| β | 25 | 80 | 32.82 | - |

Table 20 Elastoplastic parameter search ranges and optimal calibrated values

Once the elastoplastic parameters have been fit, the Lemaitre damage parameter S_0 is determined. To do this, 50 values are sampled in the range in Table 21. For the classic and proposed Lemaitre laws, tensile test simulations are conducted for each value of S_0 , with the elastoplastic parameters held constant at the previously found optimal values. As before, the parameter sets with the minimum difference from this *global* sampling are then further optimised using the *local* Nelder-Mead method [104] to refine the material parameters (Table 21). Finally, the critical damage parameter D_c is set as the maximum value for the simulated damage obtained at the failure strain (10.7% engineering strain) [105].

| Term | Range | | Optimal Value | | Units |
|-------|-------|-------|---------------|----------|-------|
| | Lower | Upper | Classic | Proposed | |
| S_0 | 5 | 25 | 13.81 | 14.29 | MPa |
| D_c | - | - | 0.078 | 0.087 | - |

Table 21 Lemaitre damage parameter search ranges and optimal calibrated values, where the proposed law corresponds to Equation 50.

The resultant force-displacement curves obtained using the calibrated parameters are given in Figure 28, and the optimal calibrated parameters in Tables 20 and 21.

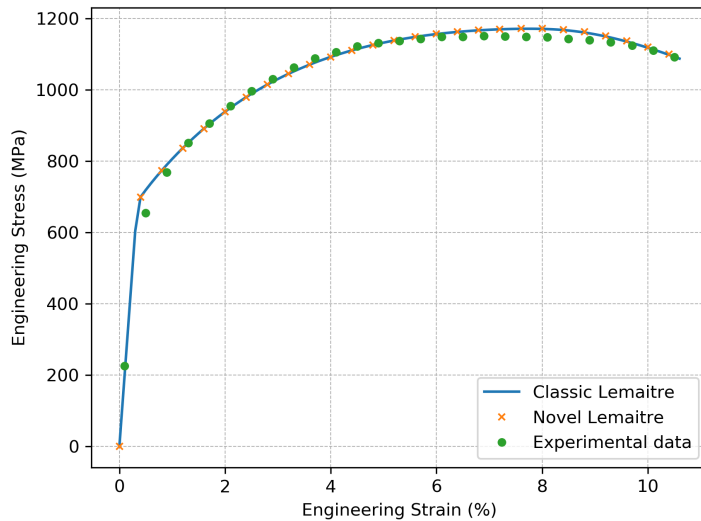


Fig. 28 Comparison of the experimental tensile test curve and the calibrated elastoplastic Lemaitre material laws. The ‘Novel Lemaitre’ model corresponds to Equation 50.

5.5.3 Predicted Evolution of Damage

For all of the cases simulated here, the damage is at a maximum towards the centre of the specimen. As an example, the predicted damage distribution for the case where $r = 36\%$, $\alpha = 6^\circ$ using the classic Lemaitre damage evolution equation is shown in Figure 29. The greatest damage occurs at the centre of the wire because this is where the triaxiality and, relatedly, the positive stress tensor are greatest. The evolution of the triaxiality and axial (xx) component of the plastic strain increment in the active deformation zone is shown in Figure 30. It can be observed that the damage evolution primarily occurs with the increase in triaxiality towards the latter stages of the plastic straining.

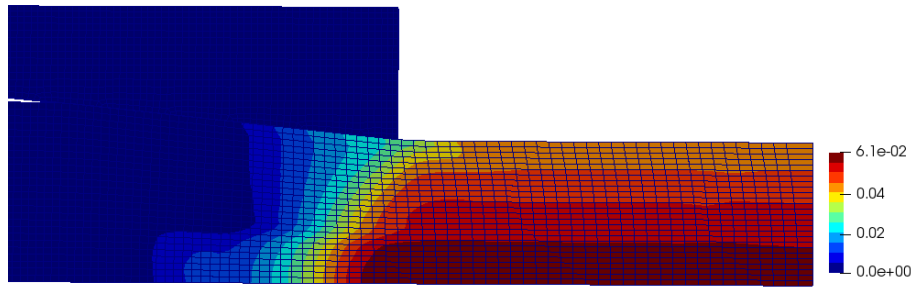


Fig. 29 Distribution of damage for $r = 36\%$, $\alpha = 6^\circ$

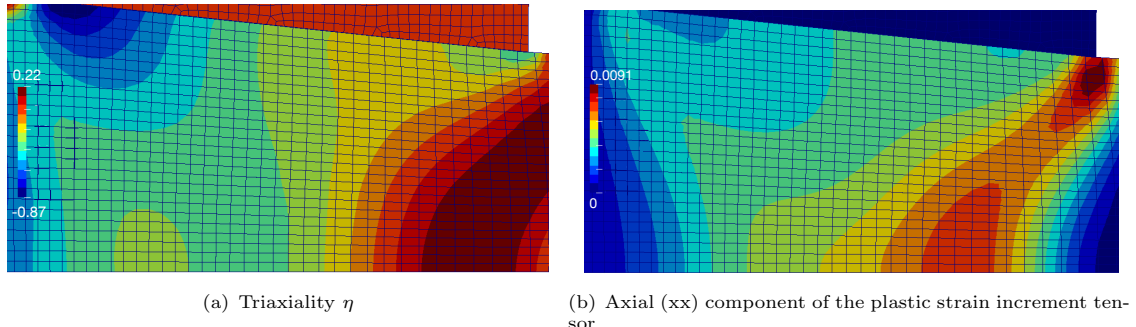


Fig. 30 Predicted distribution of triaxiality and axial component of the plastic strain increment tensor in the active deformation zone for the $r = 36\%$, $\alpha = 6^\circ$ wire drawing case

5.5.4 Fracture Prediction

To determine whether a fracture is predicted to occur, the accumulated damage at the wire axis is compared with the critical damage D_c (Figure 31). Fracture can be expected to occur when the quantity D/D_c becomes greater than or equal to 1. Figure 31 shows that both the classic and the proposed formulations of the Lemaitre model are reasonably consistent with the experimental results. The classic model accurately predicts fracture for the 20% reduction cases but overpredicts fracture in the 36% reduction cases. The novel Lemaitre-based model slightly underpredicts fracture in both the 20% and 36% reduction cases, with a value for D that is 90.4% and 90.8%

of D_c , respectively. Nonetheless, both models produce good predictive capabilities, with the novel approach being slightly closer to the experimental data.

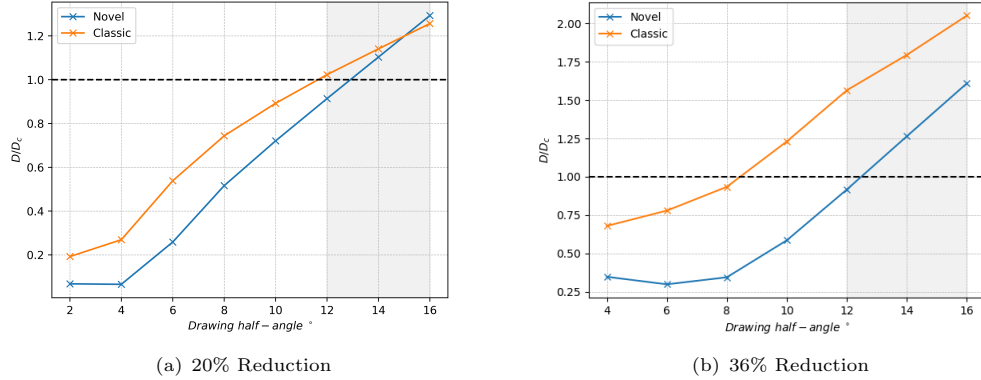


Fig. 31 Comparison of predicted and experimental fractures. The shaded region indicates where fractures occurred in experiments, corresponding to the X symbols in Table 18.

6 Conclusions

This article presents for the first time the implementation of three popular ductile damage models within a segregated, cell-centred finite volume framework. The proposed procedures are verified against popular benchmark cases from the literature, where the proposed approach has shown a robust ability to solve the highly nonlinear coupled equations. Subsequently, the ability of the examined damage models to predict damage accumulation in the wire drawing process is assessed. The main conclusions of the work are:

- An implicit, segregated solution algorithm with Picard iterations has been shown to be robust for damage modelling.
- Novel Eulerian-style layer addition and removal boundary conditions are demonstrated to be capable of simulating the continuous wire drawing process.
- Lemaitre-type models are more appropriate for predicting damage in wire drawing processes than current formulations of GTN and phase field models.
- A proposed incorporation of triaxiality dependency in the Lemaitre S parameter improves the model's predictive capabilities for wire drawing.
- The proposed effective non-local damage approach demonstrates more physically realistic damage evolution.
- Care must be taken when scaling the Rhie-Chow stabilisation term in regions of damage and plasticity to minimise mesh and time-step errors.
- A combined global-local optimisation is suitable for calibrating elastoplastic and damage parameters from experimental test data.

Regarding the prediction of damage in a wire drawing series, although the predictions generally aligned with the experimental data, limitations in the modelling approach exist: (i) Prediction of catastrophic fracture is relatively sensitive to the critical damage D_c parameter determined from

tensile test data; (ii) The assumption of Coulomb friction may be limiting in wire drawing, where hydrodynamic lubrication is known to occur; (iii) In the authors' opinion, the strong association between the positive stress tensor τ^+ and the triaxiality η at low triaxiality values (< 0.33), which occurs in wire drawing, has been neglected. Further incorporation of the positive stress tensor into the damage evolution law may potentially better describe material fracture behaviour.

Acknowledgments. This work has emanated from research conducted with the financial support of/supported in part by a grant from Science Foundation Ireland (SFI) under Grant number RC2302_2. Philip Cardiff gratefully acknowledges financial support from the Irish Research Council through the Laureate program, grant number IRCLA/2017/45, and the European Research Council (ERC) under the European Union's Horizon 2020 research and innovation programme (Grant agreement No. 101088740). Vikram Pakrashi would also like to acknowledge FlowDyn RDD/966 and SiSDATA EAPA_0040/2022. Additionally, the authors want to acknowledge project affiliates, Bekaert, through the Bekaert University Technology Centre (UTC) at University College Dublin (www.ucd.ie/bekaert), I-Form, funded by SFI Grant Number 16/RC/3872, co-funded under European Regional Development Fund and by I-Form industry partners, NexSys, funded by SFI Grant Number 21/SPP/3756, and the DJEI/DES/SFI/HEA Irish Centre for High-End Computing (ICHEC) for the provision of computational facilities and support (www.ichec.ie). Finally, part of this work has been carried out using the UCD ResearchIT Sonic cluster funded by UCD IT Services and the UCD Research Office.

Appendix A Single Cell Verifications

This appendix presents single-cell uni-axial tension tests for the Lemaitre, GTN and phase field models implemented in the solids4foam toolbox for OpenFOAM. These verifications provide confidence in the current implementations. The geometry consists of a $1 \times 1 \times 1$ mm cube, where a displacement is applied to the positive y face in the positive y direction; shear tractions on the loading surface are set to zero. Three symmetry planes are employed, and the remaining two surfaces are traction-free.

The results are compared with values from literature, analytical theory and finite element software Abaqus. The Abaqus software has an inbuilt GTN model but does not have a non-local Lemaitre model. Consequently, for this work, a non-local Lemaitre damage model was implemented in Abaqus through a user subroutine (UMAT). The approach laid out in Azinpour et al. [106] is employed to implement the non-local Lemaitre damage model's diffusion equation. This approach exploits Abaqus' ability to solve the steady-state heat conduction diffusion equation in coupled temperature-displacement problems:

$$k\nabla^2 T + Q = 0 \quad (\text{A1})$$

where k is the thermal conductivity, T is the temperature, and Q is a volumetric source term. This heat equation is made compatible with the non-local gradient equation, as shown in Table A1.

| Field | Field variable | Diffusion coefficient | Flux term | Source term |
|------------------|----------------|-----------------------|--------------|---------------|
| Temperature | T | k | $\nabla^2 T$ | Q |
| Non-local damage | \bar{D} | l_c^2 | $\nabla^2 D$ | $D - \bar{D}$ |

Table A1 Analogous set-up of the heat equation and non-local gradient equation

A.1 Lemaitre Model

A displacement of 0.2 mm is applied with mechanical properties described in Table A2. These mechanical properties are taken from Autay et al. [107].

| Property | Symbol | Value | Units |
|-----------------------------|------------|----------------------------------|-------|
| Young's modulus | E | 200 | GPa |
| Poisson's ratio | v | 0.3 | - |
| Lemaitre damage denominator | S_0 | 0.5 | MPa |
| Lemaitre damage exponent | b | 1.0 | - |
| Hardening law | σ_y | $200 + 10^3 \bar{\varepsilon}^p$ | MPa |

Table A2 Material properties for Lemaitre one cell test

The predicted damage and equivalent stress vs equivalent plastic strain from the OpenFOAM simulations are compared with values from Abaqus and analytical theory [108] in Figure A1. It can be observed that the damage increases exponentially with respect to the equivalent plastic strain. This is because, with the material constant $b = 1$, the damage increases with the square of the effective von Mises equivalent stress.

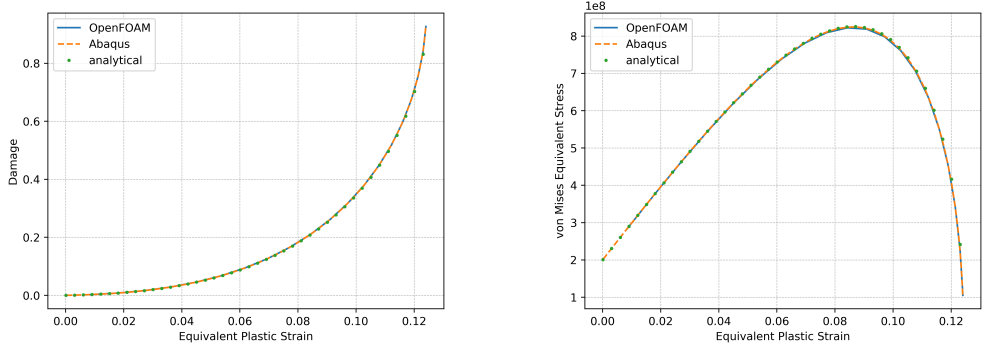


Fig. A1 Comparison of the predicted forces for the Lemaître model from OpenFOAM, Abaqus and analytical theory

The analytically derived relationship for the damage D as a function of the equivalent plastic strain $\bar{\varepsilon}^p$ is given by

$$(1 - D)^2 = 1 - \frac{\sigma_{y0}^2}{3ES_0} \frac{\sigma_{y0}}{h} \left[\left(1 + \frac{h}{\sigma_{y0}} \bar{\varepsilon}_p \right)^3 - 1 \right] \left[\frac{2}{3}(1 + v) + 3(1 - 2v)\eta \right] \quad (\text{A2})$$

where σ_{y0} and h are constants in the hardening law $\sigma_{y0} + h(\bar{\varepsilon}^p)$, and the triaxiality $\eta = 0.33$ for a uniaxial tensile test. The analytical relationship for the equivalent stress σ_v is also provided:

$$\sigma_v = (1 - D) [\sigma_{y0} + h(\bar{\varepsilon}_p)] \quad (\text{A3})$$

The component of plastic strain in the loading direction (ε_p^{yy}) can also be plotted as a function of the equivalent plastic strain $\bar{\varepsilon}_p$ and compared with the results obtained by Doghri [108] (Figure A2).

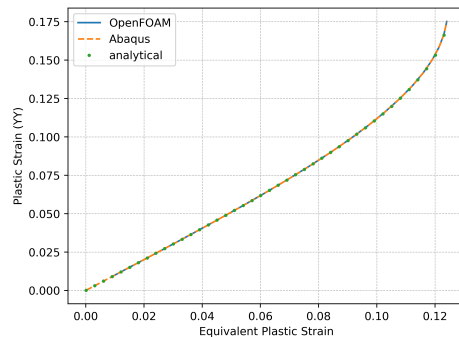


Fig. A2 Axial component of plastic strain (YY) vs. equivalent plastic strain

A.2 GTN Model

This section compares the results for the GTN model implemented in OpenFOAM with those obtained from the inbuilt GTN model in Abaqus. Table A3 displays the material properties used. The GTN model in Abaqus does not allow for the inclusion of porous failure criteria (Equation 64) in Abaqus/Standard, so this feature of the GTN model was neglected.

| Property | Symbol | Value | Units |
|--------------------|-----------------------|--------------------------------|-------|
| Young's modulus | E | 200 | GPa |
| Poisson's ratio | v | 0.3 | - |
| q_1 | q_1 | 1.5 | - |
| q_2 | q_2 | 1 | - |
| q_3 | q_3 | 2.25 | - |
| Initial porosity | f_0 | 0.002 | - |
| Mean | $\bar{\varepsilon}_n$ | 0.3 | - |
| Standard deviation | S_n | 0.1 | - |
| Volume fraction | f_N | 0.2 | - |
| Hardening law | σ_y | $400 + 300\bar{\varepsilon}_p$ | MPa |

Table A3 Material properties for GTN one cell test

The results are shown in Figure A3. Notably, the rate of porosity growth declines towards the latter stages of the deformation. This is because the porosity growth due to the nucleation of voids is assumed to follow a Gaussian distribution. As discussed in the article's main body, this assumption is unlikely to accurately describe real material behaviour.

A.3 Phase Field Model

Table A4 lists the material parameters for the phase field model one-cell test.

| Property | Symbol | Value | Units |
|--------------------------|------------|--------------------------------|------------------|
| Young's modulus | E | 68.8 | GPa |
| Poisson's ratio | v | 0.33 | - |
| Critical fracture energy | G_c | 138×10^6 | J/m ² |
| Plastic work threshold | w_0 | 1 | MPa |
| Characteristic length | l | 2 | m |
| Hardening law | σ_y | $320 + 688\bar{\varepsilon}_p$ | MPa |

Table A4 Material properties for the phase field model one cell test

Figure A4 compares the phase field model one-cell test results with those obtained by Borden et al. [24]. In this test case, the cell undergoes a rapid loss of load-carrying capacity. This is because after the plastic work threshold is exceeded, there is a rapid increase in the plastic strain energy contribution to the crack-driving force \mathcal{H} and, therefore, growth of the phase field variable d .

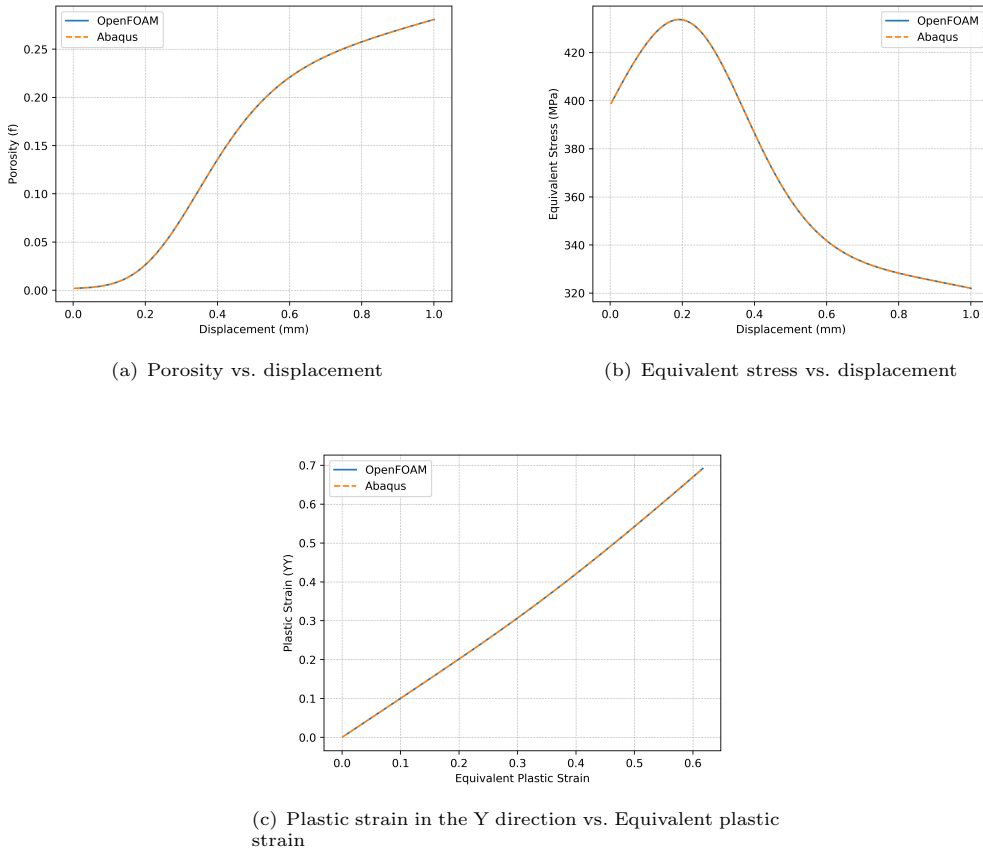


Fig. A3 Comparison between the OpenFOAM and Abaqus predictions for the GTN model one cell test

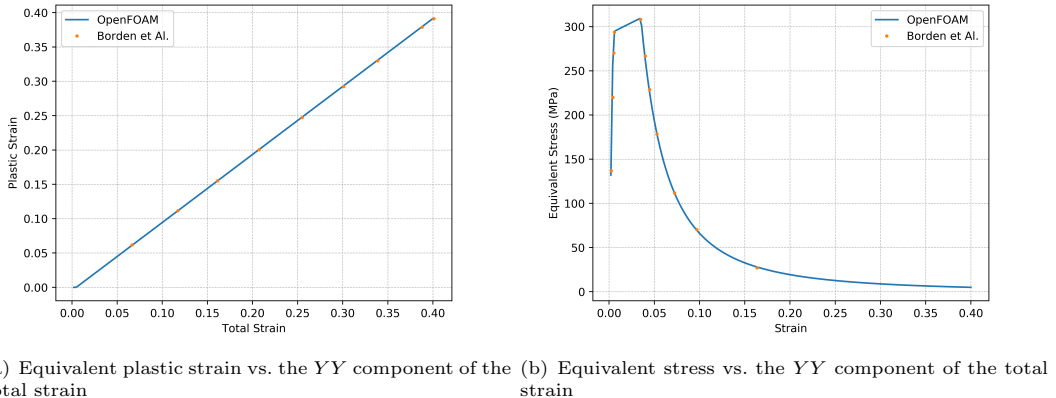


Fig. A4 Comparison between OpenFOAM and Borden et al. [24] predictions for the phase field model one cell test

References

- [1] Riccio, A. (ed.): Damage Growth in Aerospace Composites, 1st ed. 2015 edn. Springer Aerospace Technology. Springer, Cham (2015). <https://doi.org/10.1007/978-3-319-04004-2>
- [2] Johnson, A.F., Toso-Pentecôte, N., Schueler, D.: Numerical modelling of impact and damage tolerance in aerospace composite structures. In: Numerical Modelling of Failure in Advanced Composite Materials, pp. 479–506. Elsevier, ??? (2015). <https://doi.org/10.1016/j.jcomposci.2015.02.011>

doi.org/10.1016/B978-0-08-100332-9.00018-9 . <https://linkinghub.elsevier.com/retrieve/pii/B9780081003329000189> Accessed 2022-12-06

- [3] Alharbi, K., Ghadbeigi, H., Efthymiadis, P., Zanganeh, M., Celotto, S., Dashwood, R., Pinna, C.: Damage in dual phase steel DP1000 investigated using digital image correlation and microstructure simulation. *Modelling and Simulation in Materials Science and Engineering* **23**(8), 085005 (2015) <https://doi.org/10.1088/0965-0393/23/8/085005> . Accessed 2022-12-06
- [4] Sirinakorn, T., Uthaisangsuk, V., Srimanosawpal, S.: Microstructure based Description of Deformation Behavior of Dual Phase Steel Sheets. *Procedia Engineering* **81**, 1366–1371 (2014) <https://doi.org/10.1016/j.proeng.2014.10.158> . Accessed 2022-12-06
- [5] Sarraf, I.S.: Meso-Scale Modelling of Deformation, Damage and Failure in Dual Phase Steels. PhD thesis, University of Windsor (2017)
- [6] Uthaisangsuk, V., Prahl, U., Bleck, W.: Characterisation of formability behaviour of multi-phase steels by micromechanical modelling. *International Journal of Fracture* **157**(1-2), 55–69 (2009) <https://doi.org/10.1007/s10704-009-9329-4> . Accessed 2022-12-06
- [7] Chen, Y.: Modeling of Ductile Fracture Using Local Approach : Reliable Simulation of Crack Extension. PhD thesis, École des Mines de Paris (2020)
- [8] Masse, T.: Study and Optimization of High Carbon Steel Flat Wires. PhD thesis, École des Mines de Paris (2010)
- [9] Cao, T.S.: Models for ductile damage and fracture prediction in cold bulk metal forming processes: a review. *International Journal of Material Forming* **10**(2), 139–171 (2017) <https://doi.org/10.1007/s12289-015-1262-7> . Accessed 2022-12-06
- [10] Tekkaya, A.E., Bouchard, P.-O., Bruschi, S., Tasan, C.C.: Damage in metal forming. *CIRP Annals* **69**(2), 600–623 (2020) <https://doi.org/10.1016/j.cirp.2020.05.005> . Accessed 2022-12-06
- [11] Clancy, M.: Improving the predictive capabilities of wire processing simulations. PhD thesis, University College Dublin (2019)
- [12] Borchers, C., Kirchheim, R.: Cold-drawn pearlitic steel wires. *Progress in Materials Science* **82**, 405–444 (2016) <https://doi.org/10.1016/j.pmatsci.2016.06.001> . Accessed 2023-01-06
- [13] Cardiff, P., Tuković, v., Jaeger, P.D., Clancy, M., Ivanković, A.: A Lagrangian cell-centred finite volume method for metal forming simulation. *International Journal for Numerical Methods in Engineering* **109**(13), 1777–1803 (2017) <https://doi.org/10.1002/nme.5345> . Accessed 2022-10-27
- [14] Besson, J.: Continuum Models of Ductile Fracture: A Review. *International Journal of Damage Mechanics* **19**(1), 3–52 (2010) <https://doi.org/10.1177/1056789509103482> . Accessed 2022-01-13
- [15] Sumpter, J.: An Experimental Investigation of the. In: Hackett, E., Schwalbe, K.-H., Dodds,

- R. (eds.) Constraint Effects in Fracture, pp. 492–49211. ASTM International, 100 Barr Harbor Drive, PO Box C700, West Conshohocken, PA 19428-2959 (1993). <https://doi.org/10.1520/STP18042S> . <http://www.astm.org/doiLink.cgi?STP18042S> Accessed 2022-01-13
- [16] O'Dowd, N.P., Shih, C.F.: Family of crack-tip fields characterized by a triaxiality parameter—I. Structure of fields. *Journal of the Mechanics and Physics of Solids* **39**(8), 989–1015 (1991) [https://doi.org/10.1016/0022-5096\(91\)90049-T](https://doi.org/10.1016/0022-5096(91)90049-T) . Accessed 2022-01-13
- [17] James, M.A., Newman, J.C.: The effect of crack tunneling on crack growth: experiments and CTOA analyses. *Engineering Fracture Mechanics* **70**(3-4), 457–468 (2003) [https://doi.org/10.1016/S0013-7944\(02\)00131-5](https://doi.org/10.1016/S0013-7944(02)00131-5) . Accessed 2022-01-13
- [18] Mahmoud, S., Lease, K.: The effect of specimen thickness on the experimental characterization of critical crack-tip-opening angle in 2024-T351 aluminum alloy. *Engineering Fracture Mechanics* **70**(3-4), 443–456 (2003) [https://doi.org/10.1016/S0013-7944\(02\)00130-3](https://doi.org/10.1016/S0013-7944(02)00130-3) . Accessed 2022-01-13
- [19] Lemaître, J.: A Continuous Damage Mechanics Model for Ductile Fracture. *Journal of Engineering Materials and Technology* **107**(1), 83–89 (1985) <https://doi.org/10.1115/1.3225775> . Accessed 2022-01-13
- [20] Lemaître, J., Desmorat, R.: *Engineering Damage Mechanics: Ductile, Creep, Fatigue and Brittle Failures*. Springer, Berlin ; New York (2005). OCLC: ocm56646827
- [21] Gurson, A.L.: Continuum Theory of Ductile Rupture by Void Nucleation and Growth: Part I—Yield Criteria and Flow Rules for Porous Ductile Media. *Journal of Engineering Materials and Technology* **99**(1), 2–15 (1977) <https://doi.org/10.1115/1.3443401> . Accessed 2022-01-13
- [22] Tvergaard, V., Needleman, A.: Analysis of the cup-cone fracture in a round tensile bar. *Acta Metallurgica* **32**(1), 157–169 (1984) [https://doi.org/10.1016/0001-6160\(84\)90213-X](https://doi.org/10.1016/0001-6160(84)90213-X) . Accessed 2022-01-13
- [23] Ambati, M., Gerasimov, T., De Lorenzis, L.: Phase-field modeling of ductile fracture. *Computational Mechanics* **55**(5), 1017–1040 (2015) <https://doi.org/10.1007/s00466-015-1151-4> . Accessed 2022-01-13
- [24] Borden, M.J., Hughes, T.J.R., Landis, C.M., Anvari, A., Lee, I.J.: A phase-field formulation for fracture in ductile materials: Finite deformation balance law derivation, plastic degradation, and stress triaxiality effects. *Computer Methods in Applied Mechanics and Engineering* **312**, 130–166 (2016) <https://doi.org/10.1016/j.cma.2016.09.005> . Accessed 2022-01-13
- [25] Miehe, C., Aldakheel, F., Raina, A.: Phase field modeling of ductile fracture at finite strains: A variational gradient-extended plasticity-damage theory. *International Journal of Plasticity* **84**, 1–32 (2016) <https://doi.org/10.1016/j.ijplas.2016.04.011> . Accessed 2022-01-13
- [26] Dittmann, M., Aldakheel, F., Schulte, J., Wriggers, P., Hesch, C.: Variational phase-field formulation of non-linear ductile fracture. *Computer Methods in Applied Mechanics and Engineering* **342**, 71–94 (2018) <https://doi.org/10.1016/j.cma.2018.07.029> . Accessed 2022-12-08

- [27] Samaniego, C., Ulloa, J., Rodríguez, P., Houzeaux, G., Vázquez, M., Samaniego, E.: A phase-field model for ductile fracture with shear bands: A parallel implementation. International Journal of Mechanical Sciences **200**, 106424 (2021) <https://doi.org/10.1016/j.ijmecsci.2021.106424> . Accessed 2022-12-08
- [28] Cardiff, P., Demirdžić, I.: Thirty Years of the Finite Volume Method for Solid Mechanics. Archives of Computational Methods in Engineering **28**(5), 3721–3780 (2021) <https://doi.org/10.1007/s11831-020-09523-0> . Accessed 2022-10-27
- [29] Cardiff, P., Karac, A., Jaeger, P.D., Jasak, H., Nagy, J., Ivanković, A., Tuković: An open-source finite volume toolbox for solid mechanics and fluid-solid interaction simulations (2018) <https://doi.org/10.48550/arXiv.1808.10736> . <https://arxiv.org/abs/1808.10736>
- [30] Tuković, Karač, A., Cardiff, P., Jasak, H., Ivanković, A.: Openfoam finite volume solver for fluid-solid interaction. Transactions of FAMENA **42**(3), 1–31 (2018) <https://doi.org/10.21278/TOF.42301>
- [31] Bathe, K.-J.: Finite Element Procedures. Prentice Hall, Englewood Cliffs, N.J (1996)
- [32] Cardiff, P., Tuković, v., Jasak, H., Ivanković, A.: A block-coupled Finite Volume methodology for linear elasticity and unstructured meshes. Computers & Structures **175**, 100–122 (2016) <https://doi.org/10.1016/j.compstruc.2016.07.004> . Accessed 2022-12-08
- [33] Jasak, H., Weller, H.G.: Application of the finite volume method and unstructured meshes to linear elasticity. International Journal for Numerical Methods in Engineering **48**(2), 267–287 (2000) [https://doi.org/10.1002/\(SICI\)1097-0207\(20000520\)48:2<267::AID-NME884>3.0.CO;2-Q](https://doi.org/10.1002/(SICI)1097-0207(20000520)48:2<267::AID-NME884>3.0.CO;2-Q) . Accessed 2022-02-08
- [34] Demirdžić, I., Martinović, D.: Finite volume method for thermo-elasto-plastic stress analysis. Computer Methods in Applied Mechanics and Engineering **109**(3-4), 331–349 (1993) [https://doi.org/10.1016/0045-7825\(93\)90085-C](https://doi.org/10.1016/0045-7825(93)90085-C) . Accessed 2022-10-27
- [35] Cardiff, P., Karač, A., FitzPatrick, D., Flavin, R., Ivanković, A.: Development of a Hip Joint Model for Finite Volume Simulations. Journal of Biomechanical Engineering **136**(1), 011006 (2014) <https://doi.org/10.1115/1.4025776> . Accessed 2022-12-08
- [36] Cardiff, P., Karač, A., Ivanković, A.: A large strain finite volume method for orthotropic bodies with general material orientations. Computer Methods in Applied Mechanics and Engineering **268**, 318–335 (2014) <https://doi.org/10.1016/j.cma.2013.09.008> . Accessed 2022-12-09
- [37] OpenFOAM: OpenFOAM Programmer's Guide (2015)
- [38] Demirdžić, I., Cardiff, P.: Symmetry plane boundary conditions for cell-centered finite-volume continuum mechanics. Numerical Heat Transfer, Part B: Fundamentals (2022) <https://doi.org/10.1080/10407790.2022.2105073>
- [39] Greenshields, C., Weller, H.: Notes on Computational Fluid Dynamics: General Principles. CFD Direct Ltd, Reading, UK (2022)

- [40] Rodrigues, B.O.: De L'attraction des Sphéroïdes. s.n., Paris (1815). <https://gallica.bnf.fr/ark:/12148/bpt6k118869k>
- [41] Cardiff, P., Karač, A., Ivanković, A.: Development of a finite volume contact solver based on the penalty method. Computational Materials Science **64**, 283–284 (2012) <https://doi.org/10.1016/j.commatsci.2012.03.011> . Accessed 2022-10-27
- [42] Batistić, I., Cardiff, P., Tuković: A finite volume penalty based segment-to-segment method for frictional contact problems. Applied Mathematical Modelling **101**, 673–693 (2022) <https://doi.org/10.1016/j.apm.2021.09.009>
- [43] Batistić, I., Cardiff, P., Ivanković, A., Tuković, v.: A finite volume penalty-based implicit procedure for the treatment of the frictionless contact boundaries. International Journal for Numerical Methods in Engineering **124**(18), 4171–4191 (2023)
- [44] Rhie, C.M., Chow, W.L.: Numerical study of the turbulent flow past an airfoil with trailing edge separation. AIAA Journal **21**(11), 1525–1532 (1983) <https://doi.org/10.2514/3.8284> . Accessed 2022-12-01
- [45] Demirdžić, I., Muzaferija, S.: Numerical method for coupled fluid flow, heat transfer and stress analysis using unstructured moving meshes with cells of arbitrary topology. Computer Methods in Applied Mechanics and Engineering **125**(1-4), 235–255 (1995) [https://doi.org/10.1016/0045-7825\(95\)00800-G](https://doi.org/10.1016/0045-7825(95)00800-G) . Accessed 2022-02-03
- [46] Bijelonja, I.: Finite volume method for incremental analysis of small and large thermo-elasto-plastic deformations. PhD thesis, University of Sarajevo (2002). In Bosnian
- [47] Bijelonja, I., Demirdžić, I., Muzaferija, S.: A finite volume method for large strain analysis of incompressible hyperelastic materials. International Journal for Numerical Methods in Engineering **64**, 1594–1609 (2005)
- [48] Bijelonja, I.: FINITE VOLUME METHOD ANALYSIS OF LARGE STRAIN ELASTO-PLASTIC DEFORMATION. In: The 16th DAAAM International Symposium, Opatia, Croatia (2005)
- [49] Bijelonja, I., Demirdžić, I., Muzaferija, S.: A finite volume method for incompressible linear elasticity. Computer Methods in Applied Mechanics and Engineering **195**, 6378–6390 (2006)
- [50] Jacobs, D.A.H.: A Generalization of the Conjugate-Gradient Method to Solve Complex Systems. IMA Journal of Numerical Analysis **6**(4), 447–452 (1986) <https://doi.org/10.1093/imanum/6.4.447> . Accessed 2022-10-28
- [51] Karypis, G., Kumar, V.: A fast and highly quality multilevel scheme for partitioning irregular graphs. SIAM Journal on Scientific Computing **20**(1), 359–392 (1999)
- [52] Pellegrini, F.: Scotch and PT-Scotch Graph Partitioning Software: An Overview. In: Uwe Naumann, O.S. (ed.) Combinatorial Scientific Computing, pp. 373–406. Chapman and Hall/CRC, ??? (2012). <https://doi.org/10.1201/b11644-15> . <https://inria.hal.science/hal-00770422>

- [53] Garrison, W.M., Moody, N.R.: Ductile fracture. *Journal of Physics and Chemistry of Solids* **48**(11), 1035–1074 (1987) [https://doi.org/10.1016/0022-3697\(87\)90118-1](https://doi.org/10.1016/0022-3697(87)90118-1) . Accessed 2023-01-05
- [54] Bai, Y., Wierzbicki, T.: A new model of metal plasticity and fracture with pressure and Lode dependence. *International Journal of Plasticity* **24**(6), 1071–1096 (2008) <https://doi.org/10.1016/j.ijplas.2007.09.004> . Accessed 2022-03-11
- [55] Nahshon, K., Hutchinson, J.W.: Modification of the Gurson Model for shear failure. *European Journal of Mechanics - A/Solids* **27**(1), 1–17 (2008) <https://doi.org/10.1016/j.euromechsol.2007.08.002> . Accessed 2022-03-11
- [56] Eterovic, A.L., Bathe, K.-J.: A hyperelastic-based large strain elasto-plastic constitutive formulation with combined isotropic-kinematic hardening using the logarithmic stress and strain measures. *International Journal for Numerical Methods in Engineering* **30**(6), 1099–1114 (1990) <https://doi.org/10.1002/nme.1620300602> . Accessed 2023-01-05
- [57] Koji, M., Bathe, K.-J.: Inelastic Analysis of Solids and Structures. Springer, Berlin; [London (2010). OCLC: 781682619
- [58] Souza Neto, E.A., Peri, D., Owen, D.R.J.: Computational Methods for Plasticity. John Wiley & Sons, Ltd, Chichester, UK (2008). <https://doi.org/10.1002/9780470694626> . <http://doi.wiley.com/10.1002/9780470694626> Accessed 2022-01-13
- [59] Caminero, M.A., Montáns, F.J., Bathe, K.-J.: Modeling large strain anisotropic elasto-plasticity with logarithmic strain and stress measures. *Computers & Structures* **89**(11-12), 826–843 (2011) <https://doi.org/10.1016/j.compstruc.2011.02.011> . Accessed 2022-11-23
- [60] Simo, J.C., Hughes, T.J.R.: Computational Inelasticity. Interdisciplinary applied mathematics, vol. v. 7. Springer, New York (1998)
- [61] Bouchard, P.-O., Bourgeon, L., Fayolle, S., Mocellin, K.: An enhanced Lemaitre model formulation for materials processing damage computation. *International Journal of Material Forming* **4**(3), 299–315 (2011) <https://doi.org/10.1007/s12289-010-0996-5> . Accessed 2022-12-11
- [62] Malcher, L., Mamiya, E.N.: An improved damage evolution law based on continuum damage mechanics and its dependence on both stress triaxiality and the third invariant. *International Journal of Plasticity* **56**, 232–261 (2014) <https://doi.org/10.1016/j.ijplas.2014.01.002> . Accessed 2022-12-10
- [63] Ferreira, G., Campos, E., Neves, R., Desmorat, R., Malcher, L.: An improved continuous damage model to estimate multiaxial fatigue life under strain control problems. *International Journal of Damage Mechanics* **31**(6), 815–844 (2022) <https://doi.org/10.1177/10567895221091306> . Accessed 2022-12-15
- [64] Castro, F., Bemfica, C.: Calibration and evaluation of the Lemaitre damage model using axial-torsion fatigue tests on five engineering alloys. *Latin American Journal of Solids and Structures* **15**(10) (2018) <https://doi.org/10.1590/1679-78254340> . Accessed 2022-12-15

- [65] Ko, Y.K., Lee, J.S., Huh, H., Kim, H.K., Park, S.H.: Prediction of fracture in hub-hole expanding process using a new ductile fracture criterion. *Journal of Materials Processing Technology* **187-188**, 358–362 (2007) <https://doi.org/10.1016/j.jmatprotec.2006.11.071>. Accessed 2022-12-11
- [66] Roh, Y.-H., Cho, D., Choi, H.-C., Yang, Z., Lee, Y.: Process Condition Diagram Predicting Onset of Microdefects and Fracture in Cold Bar Drawing. *Metals* **11**(3), 479 (2021) <https://doi.org/10.3390/met11030479>. Accessed 2022-12-10
- [67] Bao, Y., Wierzbicki, T.: On the cut-off value of negative triaxiality for fracture. *Engineering Fracture Mechanics* **72**(7), 1049–1069 (2005) <https://doi.org/10.1016/j.engfracmech.2004.07.011>. Accessed 2022-10-11
- [68] Chu, C.C., Needleman, A.: Void Nucleation Effects in Biaxially Stretched Sheets. *Journal of Engineering Materials and Technology* **102**(3), 249–256 (1980) <https://doi.org/10.1115/1.3224807>. Accessed 2022-01-13
- [69] Teixeira, P.M.C.: Ductile Damage Prediction in Sheet Metal Forming and Experimental Validation. PhD thesis, Faculdade de Engenharia da Universidade do Porto (2010)
- [70] Basic, H., Demirdžić, I., Muzaferija, S.: Finite volume method for simulation of extrusion processes. *International Journal for Numerical Methods in Engineering* **62**(4), 475–494 (2005) <https://doi.org/10.1002/nme.1168>. Accessed 2022-12-08
- [71] Pires, F.M.A.: Issues on the Finite Element Modelling of Degradation and Prediction of Failure in Finitely Straining Ductile Materials. PhD thesis, University of Wales Swansea (2005)
- [72] Desmorat, R., Cantournet, S.: Modeling Microdefects Closure Effect with Isotropic/Anisotropic Damage. *International Journal of Damage Mechanics* **17**(1), 65–96 (2008) <https://doi.org/10.1177/1056789507069541>. Accessed 2022-12-11
- [73] Lemaître, J.: A Course on Damage Mechanics, 2., rev. and enlarged ed edn. Springer, Berlin (1996)
- [74] Peerlings, R.H.J., Geers, M.G.D., Borst, R., Brekelmans, W.A.M.: A critical comparison of nonlocal and gradient-enhanced softening continua. *International Journal of Solids and Structures* **38**(44-45), 7723–7746 (2001) [https://doi.org/10.1016/S0020-7683\(01\)00087-7](https://doi.org/10.1016/S0020-7683(01)00087-7). Accessed 2022-12-05
- [75] Peerlings, R.H.J., de Borst, R., Brekelmans, W.A.M., Geers, M.G.D.: Localisation issues in local and nonlocal continuum approaches to fracture. *European Journal of Mechanics - A/Solids* **21**(2), 175–189 (2002) [https://doi.org/10.1016/S0997-7538\(02\)01211-1](https://doi.org/10.1016/S0997-7538(02)01211-1). Accessed 2022-01-13
- [76] Geers, M.G.D., Ubachs, R.L.J.M., Engelen, R.A.B.: Strongly non-local gradient-enhanced finite strain elastoplasticity. *International Journal for Numerical Methods in Engineering* **56**(14), 2039–2068 (2003) <https://doi.org/10.1002/nme.654>. Accessed 2022-01-13

- [77] Bettaieb, M.B., Lemoine, X., Duchêne, L., Habraken, A.M.: On the numerical integration of an advanced Gurson model. *International Journal for Numerical Methods in Engineering* **85**(8), 1049–1072 (2011) <https://doi.org/10.1002/nme.3010> . Accessed 2023-01-06
- [78] Achouri, M., Germain, G., Dal Santo, P., Saidane, D.: Numerical integration of an advanced Gurson model for shear loading: Application to the blanking process. *Computational Materials Science* **72**, 62–67 (2013) <https://doi.org/10.1016/j.commatsci.2013.01.035> . Accessed 2023-01-06
- [79] Reusch, F., Svendsen, B., Klingbeil, D.: A non-local extension of Gurson-based ductile damage modeling. *Computational Materials Science* **26**, 219–229 (2003) [https://doi.org/10.1016/S0927-0256\(02\)00402-0](https://doi.org/10.1016/S0927-0256(02)00402-0) . Accessed 2023-01-06
- [80] Leclerc, J., Nguyen, V.-D., Pardoen, T., Noels, L.: A micromechanics-based non-local damage to crack transition framework for porous elastoplastic solids. *International Journal of Plasticity* **127**, 102631 (2020) <https://doi.org/10.1016/j.ijplas.2019.11.010> . Accessed 2023-01-06
- [81] Borden, M.J., Verhoosel, C.V., Scott, M.A., Hughes, T.J.R., Landis, C.M.: A phase-field description of dynamic brittle fracture. *Computer Methods in Applied Mechanics and Engineering* **217-220**, 77–95 (2012) <https://doi.org/10.1016/j.cma.2012.01.008> . Accessed 2022-01-13
- [82] Miehe, C., Hofacker, M., Welschinger, F.: A phase field model for rate-independent crack propagation: Robust algorithmic implementation based on operator splits. *Computer Methods in Applied Mechanics and Engineering* **199**(45-48), 2765–2778 (2010) <https://doi.org/10.1016/j.cma.2010.04.011> . Accessed 2022-01-13
- [83] Francfort, G.A., Marigo, J.-J.: Revisiting brittle fracture as an energy minimization problem. *Journal of the Mechanics and Physics of Solids* **46**(8), 1319–1342 (1998) [https://doi.org/10.1016/S0022-5096\(98\)00034-9](https://doi.org/10.1016/S0022-5096(98)00034-9) . Accessed 2022-03-16
- [84] Mumford, D., Shah, J.: Optimal approximations by piecewise smooth functions and associated variational problems. *Communications on Pure and Applied Mathematics* **42**(5), 577–685 (1989) <https://doi.org/10.1002/cpa.3160420503> . Accessed 2022-03-16
- [85] Ambrosio, L., Tortorelli, V.M.: Approximation of functional depending on jumps by elliptic functional via t-convergence. *Communications on Pure and Applied Mathematics* **43**(8), 999–1036 (1990) <https://doi.org/10.1002/cpa.3160430805> . Accessed 2022-03-16
- [86] Bourdin, B., Larsen, C.J., Richardson, C.L.: A time-discrete model for dynamic fracture based on crack regularization. *International Journal of Fracture* **168**(2), 133–143 (2011) <https://doi.org/10.1007/s10704-010-9562-x> . Accessed 2023-01-03
- [87] Amor, H., Marigo, J.-J., Maurini, C.: Regularized formulation of the variational brittle fracture with unilateral contact: Numerical experiments. *Journal of the Mechanics and Physics of Solids* **57**(8), 1209–1229 (2009) <https://doi.org/10.1016/j.jmps.2009.04.011> . Accessed 2022-03-22

- [88] Eldahshan, H., Munoz, D.P., Alves, J., Perchat, E., Bouchard, P.-O.: 3D crack initiation and propagation applied to metal forming processes. *International Journal of Material Forming* **15**(5), 60 (2022) <https://doi.org/10.1007/s12289-022-01702-7> . Accessed 2023-01-06
- [89] Sá, J.M.A., Areias, P.M.A., Zheng, C.: Damage modelling in metal forming problems using an implicit non-local gradient model. *Computer Methods in Applied Mechanics and Engineering* **195**(48-49), 6646–6660 (2006) <https://doi.org/10.1016/j.cma.2005.02.037> . Accessed 2022-01-13
- [90] Fincato, R., Tsutsumi, S.: A return mapping algorithm for elastoplastic and ductile damage constitutive equations using the subloading surface method. *International Journal for Numerical Methods in Engineering* **113**(11), 1729–1754 (2018) <https://doi.org/10.1002/nme.5718> . Accessed 2022-11-23
- [91] Vaz, M., Owen, D.R.J.: Aspects of ductile fracture and adaptive mesh refinement in damaged elasto-plastic materials. *International Journal for Numerical Methods in Engineering* **50**(1), 29–54 (2001) [https://doi.org/10.1002/1097-0207\(20010110\)50:1<29::AID-NME18>3.0.CO;2-G](https://doi.org/10.1002/1097-0207(20010110)50:1<29::AID-NME18>3.0.CO;2-G) . Accessed 2022-11-23
- [92] Eldahshan, H., Bouchard, P.-O., Alves, J., Perchat, E., Munoz, D.P.: Phase field modeling of ductile fracture at large plastic strains using adaptive isotropic remeshing. *Computational Mechanics* **67**(3), 763–783 (2021) <https://doi.org/10.1007/s00466-020-01962-7> . Accessed 2022-03-22
- [93] Soyarslan, C., Tekkaya, A.E.: Finite deformation plasticity coupled with isotropic damage: Formulation in principal axes and applications. *Finite Elements in Analysis and Design* **46**(8), 668–683 (2010) <https://doi.org/10.1016/j.finel.2010.03.006> . Accessed 2023-03-14
- [94] Li, H., Fu, M.W., Lu, J., Yang, H.: Ductile fracture: Experiments and computations. *International Journal of Plasticity* **27**(2), 147–180 (2011) <https://doi.org/10.1016/j.ijplas.2010.04.001> . Accessed 2022-12-02
- [95] González, A.A., Celentano, D.J., Cruchaga, M.A.: Assessment of ductile failure models in single-pass wire drawing processes. *International Journal of Damage Mechanics* **27**(9), 1291–1306 (2018) <https://doi.org/10.1177/1056789517704029> . Accessed 2022-12-13
- [96] Norasethasopon, S., Yoshida, K.: Prediction of chevron crack initiation in inclusion copper shaped-wire drawing. *Engineering Failure Analysis* **15**(4), 378–393 (2008) <https://doi.org/10.1016/j.engfailanal.2007.01.003> . Accessed 2023-01-01
- [97] Zimerman, Z., Darlington, H., Kottcamp, E.H.: Selection of Operating Parameters to Prevent Central Bursting Defects During Cold Extrusion. In: Hoffmanner, A.L. (ed.) *Metal Forming: Interrelation Between Theory And Practice*, pp. 47–62. Springer, Boston, MA (1971). https://doi.org/10.1007/978-1-4615-1757-3_2 . http://link.springer.com/10.1007/978-1-4615-1757-3_2 Accessed 2023-01-01
- [98] Choi, J.-S., Lee, H.-C., Im, Y.-T.: A study on chevron crack formation and evolution in a cold extrusion. *Journal of Mechanical Science and Technology* **24**(9), 1885–1890 (2010)

<https://doi.org/10.1007/s12206-010-0605-z> . Accessed 2023-01-01

- [99] Cao, T.-S.: Modelling Ductile Damage for Complex Loading Paths. PhD, École des Mines de Paris (2014)
- [100] Thuillier, S., Maire, E., Brunet, M.: Ductile damage in aluminium alloy thin sheets: Correlation between micro-tomography observations and mechanical modeling. Materials Science and Engineering: A **558**, 217–225 (2012) <https://doi.org/10.1016/j.msea.2012.07.116> . Accessed 2022-12-10
- [101] Fansi, J., Balan, T., Lemoine, X., Maire, E., Landron, C., Bouaziz, O., Ben Bettaieb, M., Marie Habraken, A.: Numerical investigation and experimental validation of physically based advanced GTN model for DP steels. Materials Science and Engineering: A **569**, 1–12 (2013) <https://doi.org/10.1016/j.msea.2013.01.019> . Accessed 2022-12-10
- [102] Krauss, G.: Steels: Processing, Structure, and Performance, Second edition edn. ASM International, Materials Park, Ohio (2015). OCLC: ocn904652440
- [103] Loh, W.-L.: On Latin hypercube sampling. The Annals of Statistics **24**(5) (1996) <https://doi.org/10.1214/aos/1069362310> . Accessed 2022-12-11
- [104] Luersen, M.A., Le Riche, R.: Globalized Nelder–Mead method for engineering optimization. Computers & Structures **82**(23–26), 2251–2260 (2004) <https://doi.org/10.1016/j.compstruc.2004.03.072> . Accessed 2022-12-11
- [105] Malcher, L.: Continuum Modelling and Numerical Simulation of Damage for Ductile Materials. PhD, University of Porto (2012)
- [106] Azinpour, E., Ferreira, J.P.S., Parente, M.P.L., Sa, J.C.: A simple and unified implementation of phase field and gradient damage models. Advanced Modeling and Simulation in Engineering Sciences **5**(1), 15 (2018) <https://doi.org/10.1186/s40323-018-0106-7> . Accessed 2022-11-09
- [107] Autay, R., Koubaa, S., Wali, M., Dammak, F.: Numerical Implementation of Coupled Anisotropic Plasticity-Ductile Damage in Sheet Metal Forming Process. Journal of Mechanics **34**(4), 417–430 (2018) <https://doi.org/10.1017/jmech.2017.28> . Accessed 2022-11-14
- [108] Doghri, I.: Numerical implementation and analysis of a class of metal plasticity models coupled with ductile damage. International Journal for Numerical Methods in Engineering **38**(20), 3403–3431 (1995) <https://doi.org/10.1002/nme.1620382004> . Accessed 2022-01-13